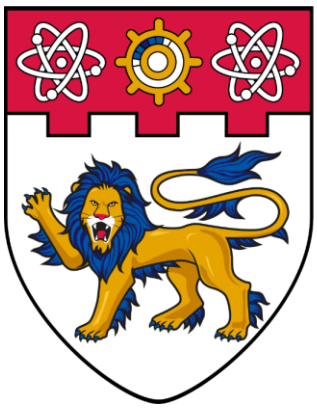

NANYANG TECHNOLOGICAL UNIVERSITY

SINGAPORE

FABRICATION AND CHARACTERIZATION OF GRAPHENE AND CARBON NANOTUBE REINFORCED BIOCERAMIC NANOCOMPOSITES

HU HUANLONG

SCHOOL OF MECHANICAL AND AEROSPACE ENGINEERING

NANYANG TECHNOLOGICAL UNIVERSITY

2019

FABRICATION AND CHARACTERIZATION OF GRAPHENE AND CARBON NANOTUBE REINFORCED BIOCERAMIC NANOCOMPOSITES

Hu Huanlong

School of Mechanical and Aerospace Engineering

A thesis submitted to the Nanyang Technological University

in partial fulfillment of the requirement for the degree of

Doctor of Philosophy

2019

Statement of Originality

I hereby certify that the work embodied in this thesis is the result of original research, is free of plagiarised materials, and has not been submitted for a higher degree to any other University or Institution.

June 2019
.....
Date

hu huanlong
.....
Hu Huanlong

Supervisor Declaration Statement

I have reviewed the content and presentation style of this thesis and declare it is free of plagiarism and of sufficient grammatical clarity to be examined. To the best of my knowledge, the research and writing are those of the candidate except as acknowledged in the Author Attribution Statement. I confirm that the investigations were conducted in accord with the ethics policies and integrity standards of Nanyang Technological University and that the research data are presented honestly and without prejudice.

June 2019

.....

Date

.....

Professor Khor Khiam Aik

Authorship Attribution Statement

This thesis **does not** contain any materials from papers published in peer-reviewed journals or from papers accepted at conferences in which I am listed as an author.

June 2019
.....
Date

hu huanlong
.....
Hu Huanlong

Acknowledgments

First of all, I would like to express my sincere gratitude to my supervisor, Prof. Khor Khiam Aik, and my co-supervisor, Assoc. Prof. Li Hua for their continuum guidance and encouragement during the past years. Thank you Prof. Khor for your insightful comments and advice that the meetings and discussions with you always give me a lot of thinking and inspirations. You not only help me touch deeper knowledge in the present research area, but also taught me life truths that will be beneficial for my life. Thank you Prof. Li for keeping me on the track.

Besides my supervisors, I would like to thank my Thesis Advisory Committee members, Assoc. Prof. Dong Zhili and Assoc. Prof. Su Peichen for their valuable comments and encouragements.

I also appreciate the friendship and technical help from my seniors Dr. Li Ruitao, Dr. Li Zhong, Dr. Xu Jinling, and Dr. Yu Ligen.

The technicians in MAE Materials Labs are also appreciated. Thank you Mr. Leong Kwok Phui, Ms. Yong Mei Yoke, Ms. Sandy Yeong Peng Neo and Mr. Thomas Lew for the technical support.

Last but not least, I would like to thank my parents for their selfless love and support in the past 29 years. Thank you for raising me up and encouraging me to pursue my dreams.

Table of contents

Abstract

Bioceramics play an important role in the replacement and regeneration of human tissues, but their intrinsic brittleness and low wear resistance make the monolithic bioceramics still problematic for load-bearing applications. The two dimensional (2D) graphene and one dimensional (1D) carbon nanotube (CNT), as the secondary strong and tough biocompatible nanofillers, are popular nanocarbons to reinforce bioceramics. However, their utilization as high-performance reinforcements in bioceramics is not fully exploited because of several significant challenges, including agglomerations of nanocarbons and the weak interfaces between nanocarbons and matrixes.

This research aimed to utilize the advantages of graphene and CNT as nanosized reinforcements to enhance the mechanical and tribological properties of bioceramics. This research specifically investigated the following: (1) the effects of reduced graphene oxide (rGO) content and mixing method on the structural and mechanical properties of rGO-reinforced hydroxyapatite (HA) composites; (2) the effect of nanocarbon morphologies on the structural and mechanical properties of nanocarbon-reinforced HA composites; and (3) the evaluation of the tribological behaviors of nanocarbon-reinforced HA composites at micro- and nano- scales.

In terms of nanocarbon content, monolithic HA and HA reinforced with various contents of rGO (0, 1, 2, 5, and 10 wt%) were prepared and characterized. The hardness, Young's modulus and fracture toughness of the composites were increased with up to 2 wt% rGO and reduced with 5 and 10 wt% rGO as reinforcements. With increasing rGO concentration, the densification rate decreased, and the number of rGO agglomerations and porosities increased. The improvement in mechanical properties

was mainly attributed to the microstructure refinement of the composites, and the crack bridging and branching mechanisms of rGO.

Regarding mixing methods, all the ultrasonication mixed and ball milled 1 wt% rGO reinforced HA composites were almost fully densified. The hardness and fracture toughness of SPSed pellets were improved in all the rGO-HA composites, and the highest values were obtained in the composite mixed with ultrasonication in ethanol solvent. Although the high-speed wet ball milling method facilitated the satisfactory dispersion of nanocarbons into HA bioceramics, a large number of defects were introduced simultaneously. In contrast, the ultrasonication mixing method was superior with similar dispersion efficiency but fewer defects generated on rGO.

When one type of nanocarbons was used, the size and shape of the nanocarbons significantly influenced the structural and mechanical behaviors of the reinforced composites. The highest hardness and fracture toughness were obtained from SPSed rGO-HA and the CNT-HA composites, with 30.6% and 43.1% improvements over the pure HA samples, respectively. In rGO-HA composites, the rGO plates with large lateral dimensions could wrap HA grains for finer and layered microstructures for higher hardness. In CNT-HA composites, the interactions between CNTs and HA matrixes were enhanced by the formation of the unique mechanical locking structures in CNTs.

When rGO and CNT hybrid were used as reinforcements, the optimum dispersion of rGOs and CNTs, and the strong interface bonding between the nanocarbons and HA matrixes were established in the composites. Furthermore, the small-sized CNTs were found inserted into rGO plates in the mixed powder and sintered pellets. As a result, the HA composite reinforced with rGO and CNT hybrids showed a significant

improvement in mechanical properties. They exhibited higher hardness and fracture toughness than the ones reinforced with one type of nanocarbon.

In the micro-scale ball-on-disk tribological tests, the wear and friction behaviors were strongly dependent on nanocarbon content and morphology. By increasing the total nanocarbon contents from 1 wt.% to 2 wt.%, the wear resistance of both rGO and rGO + CNT hybrids reinforced composites were substantially increased. Under 2 wt% total nanocarbon content and with the morphology of rGO/CNT hybrid, the wear resistance was improved up to ~17 times that of monolithic HA.

In the nano-scale tribological tests, the wear and fatigue performances depended on nanocarbon morphology, nanocarbon content, normal force, and wear velocity. The maximum wear track deformation and wear volume loss demonstrated nearly perfect quadratic and linear relations, respectively. The 1 wt% rGO based composites exhibited ~3.35 times lower wear rate than that of pure HA sample under 1 μm/s scratching speed and 5 mN normal force conditions. The reinforcing mechanism was due to the lubrication and pinning effects of rGO, which resulted in high resistance to penetration, elastic recovery capability, low-cycle fatigue resistance, and microcrack propagation inhibition properties.

Therefore, by varying nanocarbon content and mixing method, and nanocarbon morphology, the HA bioceramics were strengthened and toughened. In addition, the tribological results at both micro- and nano- scales suggested that rGO and CNT reinforced HA bioceramic composites had higher long-term capabilities to sustain the complex environments and load scales when used as artificial substrates in human beings. The mechanical and tribological results suggested the clinical applications of HA were expected to be extended with rGO and CNT as reinforcements.

Abbreviations

BM	Ball mill
CNT	Carbon nanotube
CMC	Ceramic matrix composite
CTAB	Cetyltrimethyl ammoniumbromide
DI water	Deionized water
EDS	Energy dispersive X-ray spectroscopy
FESEM	Field emission scanning electron microscopy / microscope
GNP	Graphene nanoplatelet
GO	Graphene oxide
HA	Hydroxyapatite
MWCNT	Multi-walled carbon nanotube
PDF	Powder Diffraction File
R-CNT	Raw carbon nanotube
rGO	Reduced graphene oxide
SPS	Spark plasma sintering
TCP	Tricalcium phosphate
TEM	Transmission electron microscopy / microscope
UT	Ultrasonication
XRD	X-ray diffraction / diffractometer
SBF	Simulated body fluid
0D	Zero dimensional
1D	One dimensional
2D	Two dimensional

Figure Captions

Table Captions

Chapter 1 Introduction

1.1 Background

Bioceramics have received increased attention in replacement and regeneration of human tissues during the past few decades due to their excellent bioactivity, biocompatibility, and corrosion resistance [1-4]. Bioceramics are found in a variety of different applications through the body, covering all areas of the skeleton: dental implants, bone defects, fracture treatment, etc. [5]. Among the diverse forms of bioceramics, hydroxyapatite ($Ca_{10}(PO_4)_6(OH)_2$, HA) is advantageous as it is the main mineral component in bones and teeth of vertebrates and has been applied as biomaterials because HA bioceramics are biocompatible, bioactive, osteoconductive, and bioresorbable. In spite of their successful clinical applications, the intrinsic brittleness or low fracture toughness of monolithic bioceramics makes them still problematic for load-bearing applications in tissue engineering [6, 7].

In order to extend the clinical applications of bioceramics, various strategies have been proposed. Among them, the addition of secondary strong and tough biocompatible phases has become popular for significant improvement in the mechanical properties and unreduced biological properties of the bioceramic matrixes. The carbonaceous nanomaterials, especially graphene and carbon nanotube, are attracting considerable research interests in this aspect. The graphene and CNT have outstanding physical and mechanical properties and they are promising reinforcing phases in the development of

nanocomposites for tissue engineering [5]. It has already been demonstrated that the introduction of such nanofillers could dramatically improve the overall and microscopic mechanical properties of the composites, as compared with both pure ceramics and non-nanocarbon composites [6-9]. In addition, graphene and carbon nanotube have been proved to be biocompatible when incorporated into ceramics as well [10-14].

Nevertheless, significant challenges remain due to the stacking of graphene nanoplates (GNPs) and agglomerations of CNTs, and the weak interfaces between the reinforcements and matrixes. The reinforced properties of bioceramics are achieved, not only by choosing the nanofillers with proper inherent properties but also by optimizing the dispersion level and nanoscale interfaces to take advantages of the excellent mechanical properties and enormous surface areas of the nanocarbons. However, the GNPs tend to restack due to their large Van der Waals and strong π–π interactions and CNTs tend to entangle and agglomerate due to their high aspect ratio (length/diameter) and strong Van der Waals interactions [8-10]. Thus, the reinforcing effects of nanocarbons in bioceramics are not fully utilized and the leading challenges in the manufacturing of nanocarbon reinforced bioceramic composites still lie in the dispersion of GNP and CNT, and their interface interactions with the bioceramic matrix. Furthermore, systematic characterizations are of essential importance to reveal the relationships between the structural behaviors, and mechanical or tribological behaviors of the composites.

1.2 Objectives and scope

This is an interdisciplinary project that spans from the basic to applied aspects of nanocarbon reinforced bioceramic composites in materials, mechanical engineering, biology, and chemistry. The key issue is to reveal and combine the advantages of 1D CNT and 2D graphene as reinforcements by studying the effects of CNT and GNP in their dispersion and interactions with bioceramics on the structural, mechanical and tribological behaviors, to extend bioceramic's clinical applications.

The flowchart of the key experiments covered in this thesis is presented in Figure 1.1. The general fabrication routes include two processes (marked with yellow arrows in Figure 1.1): (a) the dispersion of nanocarbons into HA bioceramic powders to obtain mixed composite powders; (b) the densification of the composite powders through spark plasma sintering (SPS) to obtain densified compacts.

The three studies covered (filled with light blue in Figure 1.1) are as follows:

1. *To study the effects of rGO content and mixing method on the structural and mechanical properties of rGO reinforced HA composites (chapter 4).*

   The focus of this study was on the two key factors that influencing the reinforced properties of the composites, including rGO content and mixing method. In the first case, monolithic HA and HA reinforced with various contents of rGO (0, 1, 2, 5, and 10 wt%) were prepared and characterized. In the second case, 1 wt% rGO was used as the reinforcement in HA composites and the mixing methods were classified as two groups: (a) ultrasonicated group

(i. using CTAB as surfactant and DI water as solvent, ii. using ethanol as the solvent without surfactant); (b) ball milled group (at low and high milling speeds).

2. *To study the effect of nanocarbon morphologies on the structural and mechanical properties of nanocarbon reinforced HA composites (chapter 5);*

   In this study, the effect of nanocarbon morphologies was investigated in two cases: (a) using individual nanocarbon (rGO, CNT and GO) as reinforcement to study the size and shape effects of nanocarbons; (b) using rGO and CNT hybrids as reinforcements to study the interactions between rGO and CNT, and the ones between nanocarbons and HA matrixes.

3. *To evaluate the tribological behaviors of nanocarbon reinforced HA composites at both micro- and nano- scales (chapter 6).*

   In this study, the tribological behaviors of rGO and CNT reinforced HA bioceramics were studied, to indicate the long-term reliability of the reinforced composites. The experiments were conducted under two load scales: (a) microscale by ball-on-disk tribological tests; (b) nanoscale by scratching tests.

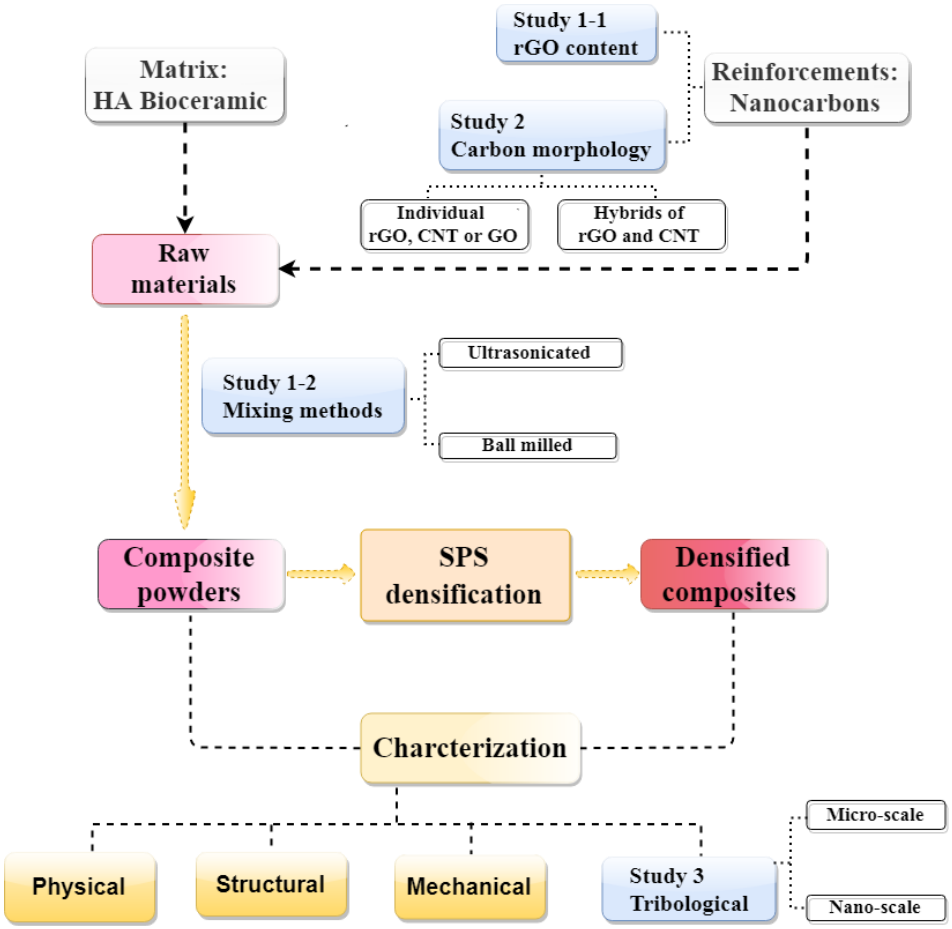

Figure 1.1 Key components covered in this thesis.

Chapter 2 Literature review

2.1 Bone and bioceramics

Bone is the most important hard tissue in the human body that plays an important role in protecting vital organs, providing adhesion for muscles and producing blood cells [2, 11]. In this aging population, the need for bone regeneration is increasing, and the demands and requirements in bioceramics for the replacement and regeneration of human tissues are becoming higher [12, 13]. Although bioceramics are the "gold" materials to repair damaged bone or tooth, their intrinsic brittleness and insufficient wear resistance make the monolithic bioceramics still problematic for load-bearing applications.

2.1.1 Bone

Bone is a dense tissue that constitutes of organic (such as collagen) and inorganic (such as HA and Calcium Carbonate ($CaCO_3$)) constitutes [14]. The organizations of typical compact bone are illustrated in Figure 2.1.

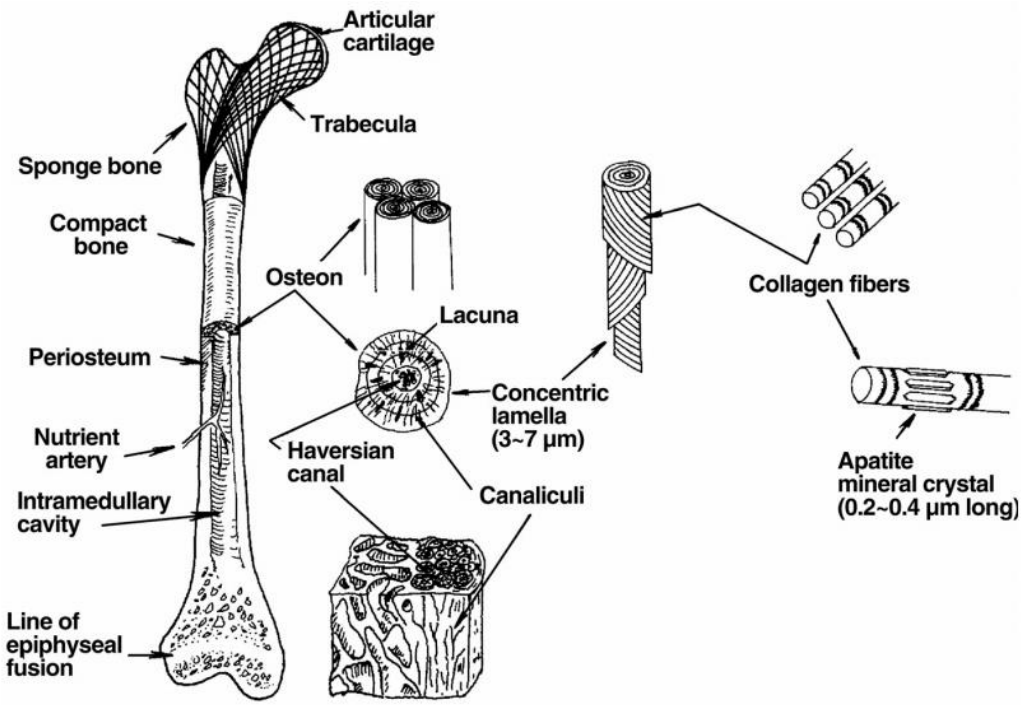

Figure 2.1 Organization of typical bone [15].

Distinguished by the structures of bone, it has long been classified into cortical and cancellous types, at macrostructure level [15] and the properties of these two types of bones differ. Table 2-1 lists the physical and mechanical properties of the representatives of compact bone and sponge bone.

Table 2-1 Physical properties of cortical and cancellous bones [16].

	Cortical	**Cancellous**
Density (g/cm3)	1.6-2.1	0.1-1.0
Young's modulus (GPa)	7-25	0.05-0.5
Strain to failure (%)	1-3	5-7
Compressive strength (MPa)	170-193	7-10
Tensile strength (MPa)	50-150	10-20
Fracture toughness (MPa m1/2)	2-12	0.1

In the current world with an aging population and higher expectations for life quality, there is an increasing demand for the replacement and regeneration of human tissues.

Clinically, the bone substitutes consist of natural bone grafts and synthetic bone grafts. The clinically available natural bone grafts and their limitations are classified as [5]:

1. Autologous bone graft: good osteoconduction, osteoinduction, and osteogenesis properties, but the availability is limited and there is a high risk of donor site morbidity;
2. Allogeneic bone graft: the second choice with good biological properties, but it has a high risk of disease transmission and immune reaction.

Due to the drawbacks of natural bone grafts, there is a need to find appropriate synthetic bone grafts for bone cure [17]. Currently, the most used implants in load-bearing applications are metal implants. However, the biological and tribological performances of metal implants are not satisfied because failures can occur by the following reasons: implant motion, inflammation, and bone resorption and osteolysis due to implant loosening, wear and improper loading [18].

2.1.2 Bioceramic and hydroxyapatite

Calcium-phosphate based bioceramics, making up to 70% of human bone and teeth mineral, are the gold materials in the areas of human tissue replacement and regeneration because they process excellent bioactivity, biocompatibility and corrosion resistance. LL Hench classified bioceramics as the following 3 categories [4] and the physical properties of major bioceramics are listed in Table 2-2:

1) Bioinert (alumina, zirconia): do not provoke or undergo reactions with the surrounding tissues;

2) Absorbable (TCP): filling materials absorbed by the body;

3) Bioactive (HA, bioactive glasses and glass-ceramics): the increased phenomenon of adhesion, through stimulation of bone regrowth.

Table 2-2 Properties of major bioceramics used for tissue engineering.

Material	Young's modulus (GPa)	Compressive strength (MPa)	Modulus of rupture (MPa)	Density (g/cm^3)
HA	100~200	~1000	<100	3.15
TCP	~100	~1000	~100	~2.8
Bioglass	11-63	950	12	2.7

The bioceramics are widely used in different applications through the body, covering all areas of the skeleton: bone defects, dental implants, fracture treatment, etc [19]. The examples of commercial bioceramic implants are shown in Figure 2.2 [2]. The powders and granules are used as bone fillers (typically calcium phosphates or bioactive glass), the hemispherical acetabular cup (made of alumina) is for hip joint implant and the coating (made of HA) is deposited on metals.

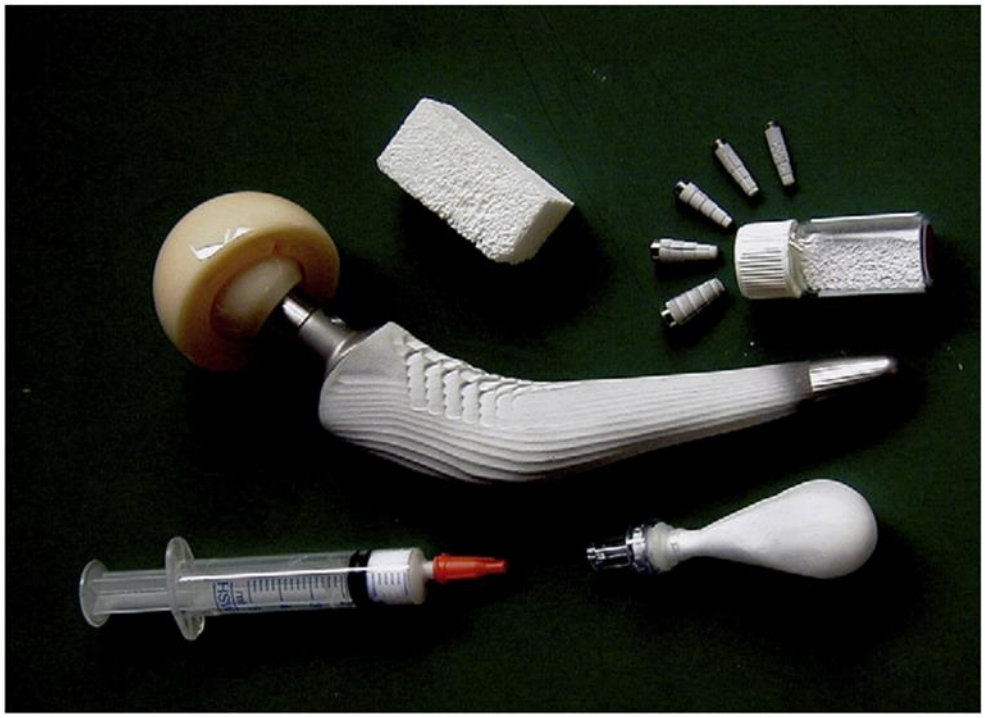

Figure 2.2 Examples of commercial bioceramic implants [2].

Compared with other bioceramics, hydroxyapatite ($Ca_{10}(PO_4)_6(OH)_2$, HA) is advantageous as it is the main mineral component in bones and teeth of vertebrates and has been applied as biomaterials because HA bioceramics are biocompatible, bioactive, osteoconductive, and bioresorbable.

The crystal structure of hydroxyapatite projected on x,y plane is shown in Figure 2.3. The crystal system and space group of HA are hexagonal and P63/m, respectively. The dimensions of unit cell are a = b = 0.943 nm and c = 0.688 nm. In each unit cell, it contains 10 Ca^{2+}, 6 PO_4^{3-} and 2 OH^- [20]. In terms of using HA as implants, the cationic (substituting for calcium) and anionic (substituting for the phosphate or hydroxyl groups) substitutions could alter the biological response and physical properties [21]. Furthermore, the thermal stability of HA is of critical importance because HA may be

decomposed at elevated temperatures that are involved in the sintering and plasma spraying process [22].

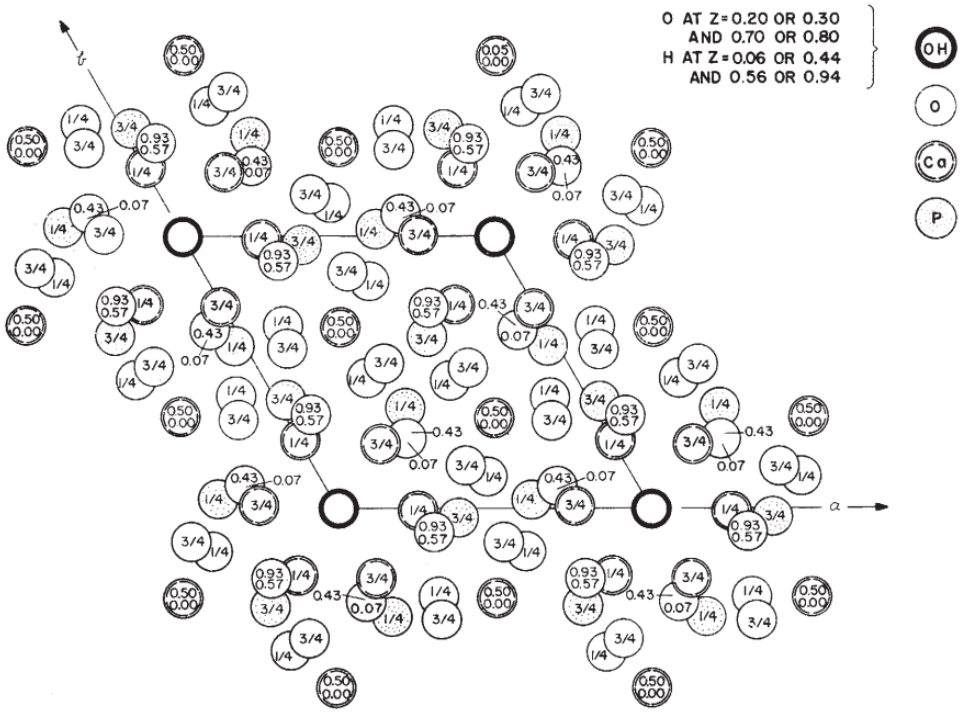

Figure 2.3 Crystal structure of hydroxyapatite projected on *x*,*y* plane [23].

For HA bioceramic, it has been used in the forms of powders and bulk implant in non-load bearing areas [24]. In load-bearing applications, HA is commonly used as coatings to be deposited on metals for better biological properties. However, during the implantation process, there is a risk that the contact shear stresses can overcome the coating-substrate adhesion strength and these coatings can be detached from the metal surface, thus causing the failure of implantation [25, 26]. Furthermore, the application of using HA in the bulk form in load-bearing applications is also still problematic due to the intrinsic brittleness and insufficient wear resistance of HA [6–8]. The poor

mechanical properties of HA can lead to instability and unsatisfactory duration of the implant or scaffold in the presence of body fluids and under local loading [27].

2.2 Nanocarbon reinforced composites

2.2.1 Introduction

In order to extend the clinical applications of bioceramics, the addition of carbonaceous nanomaterials, especially graphene and carbon nanotube, is attracting considerable research interests in this aspect [28, 29]. The unique mechanical properties of graphene and CNT make them promising reinforcing phases in the development of nanocomposites for tissue engineering [30-33].

Graphene and carbon nanotube are dimensionally confined sp^{2-} bonded carbonaceous nanomaterials with unique electrical, mechanical, thermal, and optical properties. Graphene is the thinnest and strongest material with one-atom-thick planar sheet of carbon atoms densely packed in a honeycomb crystal lattice [34, 35]. It is the elementary structure of other carbonaceous nanomaterials [36], which exist in three principle shapes: graphene can be stacked one over another to make 3D graphite, or rolled into tubes to make 1D carbon nanotubes, or wrapped up to form 0D fullerenes, as shown in Figure 2.4.

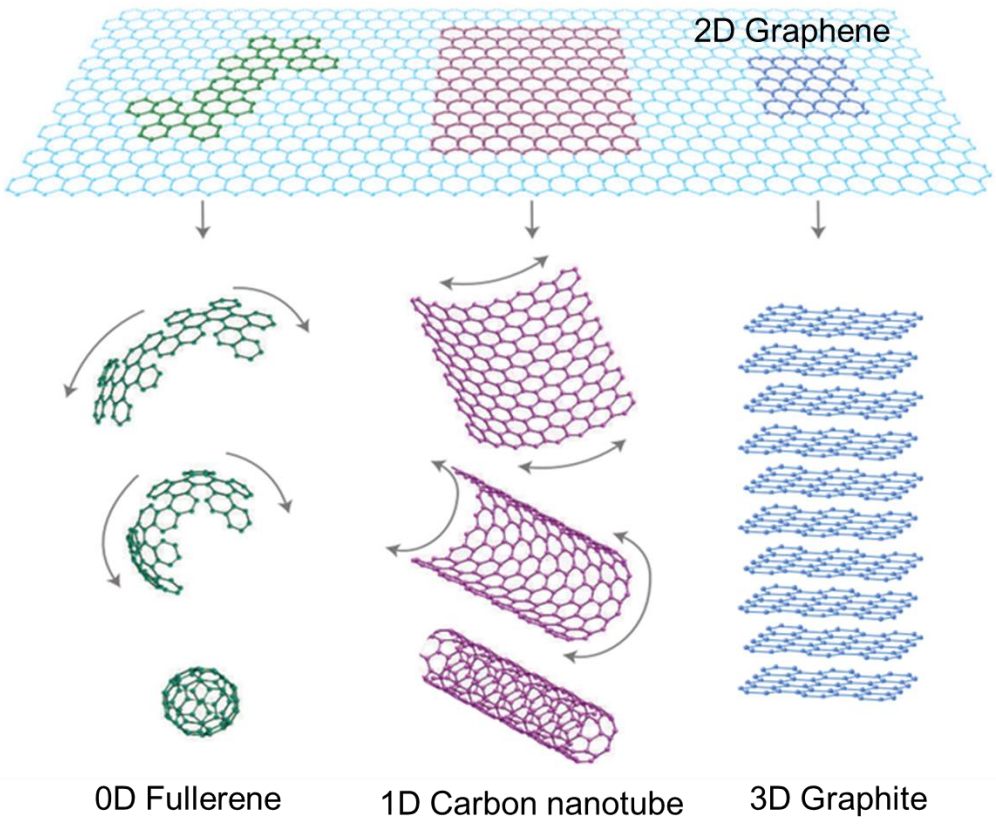

Figure 2.4 Schematic illustration of 0D fullerenes, 1D carbon nanotubes, 2D graphene, and graphite [35].

In recent years, the research on graphene and carbon nanotube is an increasingly popular topic and there are many breakthroughs in fabrications and applications of nanocarbons. The applications of graphene and carbon nanotube are found in various fields including lithium-ion batteries [37], biosensors [38], transparent conductors [39] and supercapacitors [40]. Especially, the study of nanocarbon-based composites has been raised rapidly following the preparation and isolation of graphene and carbon nanotube. Figure 2.5 shows the number of peer-reviewed publications on graphene and carbon nanotube reinforced ceramic composites in the past two decades, and the data source was Elsevier Scopus by searching the words “graphene” + “ceramic” and

"carbon nanotube" + "ceramic", respectively. The research on carbon nanotubes-based CMCs became popular around 2002 and has lasted until now. In terms of graphene-based CMCs, the annual number of publications is growing rapidly since the year 2010 and in the past two years, the numbers are more than two hundred. In 2009, Mohammad A. Rafiee et al. reinforced epoxy with graphene nanoplates and carbon nanotubes. Compared with both SWCNT and MWCNT, graphene shows superior efficiency in terms of mechanical properties enhancement, with Young's modulus, tensile strength, and fracture toughness increased by 3 %, 14 %, and 20 %, respectively [41]. Two years later, the first publication of graphene reinforced ceramic composites was published by Luke S.Walker [42].

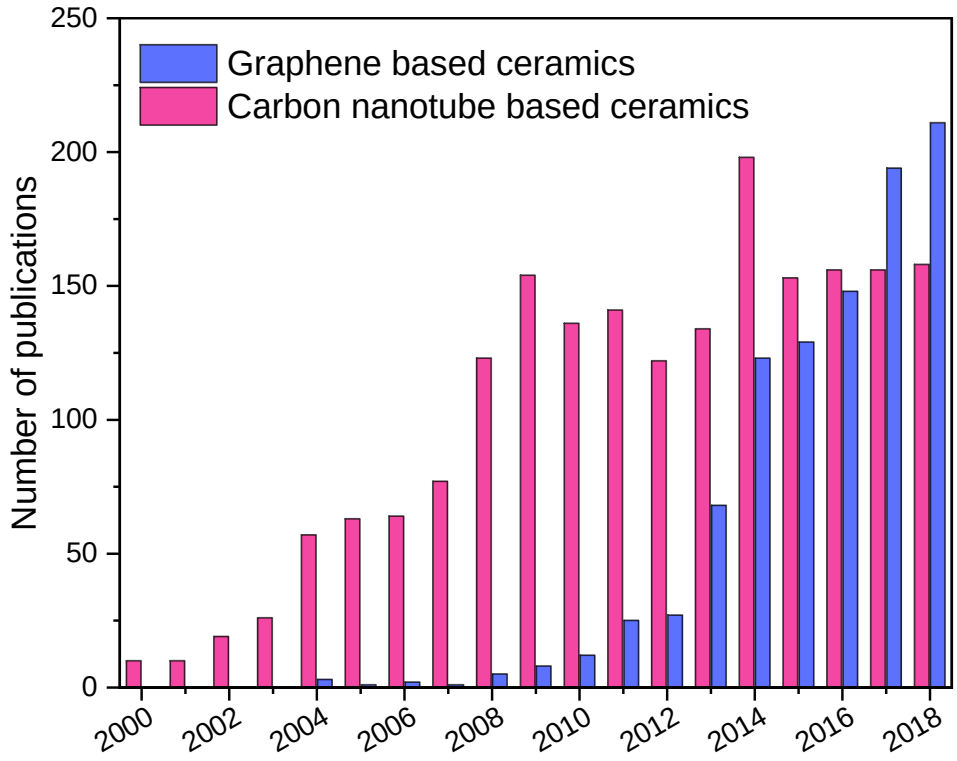

Figure 2.5 Scholarly output analysis of graphene and carbon nanotube based ceramic composites. Data source: Elsevier Scopus.

2.2.2 Properties of graphene and carbon nanotube

Graphene and carbon nanotube have advanced mechanical and biological properties that could be incorporated into bioceramic scaffolds in tissue engineering [43]. In terms of using nanocarbons as reinforcements in bioceramics, the intrinsic physical and mechanical properties and biological properties of nanocarbons are of vital importance.

2.2.2.1 Physical and mechanical properties

The physical and mechanical properties of carbon fillers related to composites application are listed in Table 2-3. Compared with the traditional reinforcements, such as carbon fiber and carbon particles (carbon black) that always present in the forms of micro- and macro- scales, it is an advantage of the nanocarbons to have the excellent and unprecedented physical and mechanical properties, and thousands of times higher the surface area. Furthermore, these properties are dependent upon complex factors, such as nanocarbon size, number of walls/layers, concentration, type of defects, and synthesis strategy [44].

Table 2-3 Physical and mechanical properties of carbon fillers.

Material	Young's modulus (GPa)	Fracture strength (GPa)	Elongation at break (%)	Density (kg/m3)	Surface area (m2/g)	Aspect ratio	Reference
Graphene	~1000	~130	0.8	2200	2630	6000-600,000	[34, 45]
GO	23-42	0.13	0.6	1800	700-1500	1500-45,000	[46, 47]
CNT	950	11-63	12	1330	70-400	1000-10,000	[48, 49]
Carbon fiber	7-400	0.4-5	1.7	1770	0.134	100-1000	[50]

2.2.2.2 Biological Properties

Nanocarbons' biological properties are also believed to be determined by various factors, such as the number of layers/walls, dimension, chemical structure, morphology, hydrophilicity, etc.

Recent investigations have indicated that graphene and carbon nanotube are promising fillers in biomaterial composites, as they possess nontoxic for human osteoblasts, excellent antibacterial property, suitable for adhesion and proliferation of osteoblasts and the ability of apatite mineralization [30]. Especially, the interconnected, conductive graphene network in a graphene/bioceramic composite placed in a bone defect might transfer electrical signals from the surrounding natural bones, thus generating a beneficial microenvironment to help bone remodeling around the implant [33].

With regards to bioceramic composites application, the biological performance of graphene and carbon nanotube usually evaluated by *in vitro* tests, namely SBF immersion and cell culture. SBF immersion is an easy and powerful method to assess the bioactivity of bioceramics [51]. The formation of an apatite layer on the surface of ceramic is due to ion exchange between the sample and the surrounding SBF. The rate of apatite layer formation could be used to indicate the degree of a material's bioactivity. Cell culture is another common approach employed in *in vitro* study as it is of key importance to developing new materials for biomedical applications [52]. Biocompatible materials would provide active surface sites for cell attachment, migration, and proliferation.

2.2.3 Graphene and carbon nanotube dispersion in ceramic matrix

The mixing of the nanofillers and matrix material is the most challenging step in preparing nanocarbon based bioceramics [53]. It has a direct influence on the reinforcing phase's dispersion level and its adhesion to the matrix, thus influencing the mechanical properties of the composites. In addition, the mixing process may alter the physical and chemical properties of the fillers and matrixes, which would affect the intrinsic properties of the fillers and matrixes, and the way they interact between the matrix and filler materials.

2.2.3.1 Physical processing

The physical mixing method is the most convenient and commonly used technique to disperse the second phase reinforcements into bioceramics. In this mixing method, the filling material is firstly deagglomerated using various methods, including ultrasonication and ball milling, and then mixed with the ceramic powder in a solvent. In terms of mixing graphene and carbon nanotube into bioceramics by physical processing methods, the amount of agglomerations of nanocarbons in the composites that resulted from the high aspect ratios of nanocarbons, and the change in mechanical and structural properties of nanocarbons are inevitable. Therefore, it is interesting to study the effects of mixing methods on the mixing efficiency of nanocarbons into bioceramics and the change in the properties of nanocarbons induced by the processing routes.

2.2.3.2 Colloidal processing

The colloidal processing is on the basis of colloidal chemistry [54] that nanocarbon–ceramic mixtures are prepared by combining the colloidal suspensions of nanocarbon and ceramic powders.

Graphene and CNT are hydrophobic that cannot be dispersed in polar solvents [55]. With the aid of proper surfactants, the effective specific surface charge is created in the surface of nanocarbons and a stable solution can only be obtained. The commonly used surfactants are CTAB, SDBS and SDS [42, 56]. In contrast, graphene oxide (GO) has a similar structure to graphene but oxygen-containing functional groups are presented in the planes or edges of GO. As a result, the hydrophilic oxygen groups make GO can be easily dispersed into water to form stable colloidal suspensions [57, 58] and its interaction and compatibility with polar solvents or with a particular bioceramic matrix are promoted. However, the intrinsic mechanical properties of GO are always lower than graphene because of the presence of these functional groups.

2.2.4 Reinforcing efficiency and mechanisms of nanocarbon reinforced ceramics

The conventional carbonaceous fillers, such as graphite and carbon fiber, are usually in macro or micro scale, while graphene and carbon nanotube are nanostructured materials that have large surface areas and surface energy. Therefore, the 2D graphene and 1D CNT have much larger surfaces to interact with the matrix material and the intrinsic mechanical properties of the nanocarbons are dramatically improved. With better toughening effects, novel toughening mechanisms are introduced due to their unique

structures, as shown in Figure 2.6. From another aspect, their high aspect ratios make it difficult to homogeneously disperse graphene or CNT into the matrix material. Thus, the extent to which ceramics are reinforced is determined by the following complex factors.

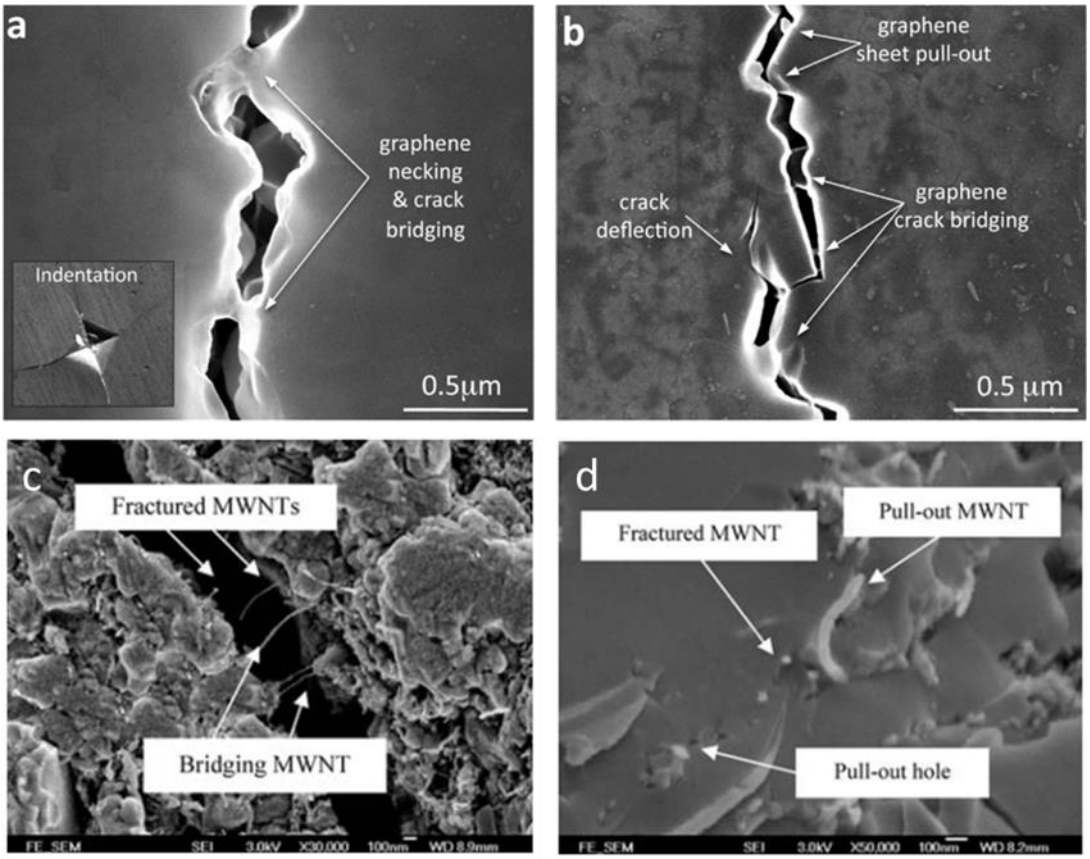

Figure 2.6 Toughening mechanisms of GNP (a,b) [42] and CNT (c,d) based composites

2.2.4.1 Reinforcing efficiency of nanocarbons

The reinforcing efficiency of the nanoscale fillers is mainly determined by the following 3 factors:

(1) The intrinsic properties of the filler material

With regards to composites application, the intrinsic properties of the reinforcements include their mechanical strength and morphology (dimension, aspect ratio, alignment, etc.). From the mechanical strength aspect, graphene and CNT are the thinnest and strongest materials ever found, as discussed earlier. From the morphology aspect, GNP and CNT have greatly increased the specific interfacial area to interact with the matrix in composites.

(2) The efficiency of load transfer at the interface of matrix and filler

The mechanical properties of the composites are influenced by the efficiency of load transfer from the ceramic matrix to nanocarbon fillers and the interfacial interactions between the ceramic matrix and nanocarbon fillers are of vital importance [59, 60]. When load transfers are acting efficiently, the reinforcement carries a higher proportion of the externally applied load. Thus, the matrixes endure less load and the stress concentrations within the matrixes are reduced. The typical intermolecular interactions, relevant to nanocarbon based composites, that have a major influence in load transfer are listed in Table 2-4 [61].

Table 2-4 Intermolecular interactions relevant to nanocarbon based composites [61].

Interaction	Strength (kj mol $^{-1}$)	Bond length (nm)	Restorability
Covalent	355-730	0.15-0.26	N
Hydrophobic	40r	<0.5	Y
π-stacking	8-12	0.5	Y
Coulombic	5.8-232	0.3-1.0	Y
Hydrogen	4-20	0.24-0.35	Y
Van der Waals	2-4	0.3-0.5	Y

(3) The dispersion level of the nanoscale filers in the host matrix.

Among these three factors, uniform dispersion and distribution of the nanofillers is the fundamental requirement and most challenging step to enable their utilization as high-performance reinforcements. Distributed network morphology and suppressed aggregation will increase the areas of nanocarbon surfaces to interact with the matrix, thus improve the reinforce efficiency.

Up to now, it is still a challenge to simultaneously optimize the above three factors. For example, graphene with increased layers, more defects and functional groups will suffer a decrease in its intrinsic mechanical properties, while these changes will result in higher load transfer efficiency and more homogenous dispersion. As the final reinforcing effects of nanocarbons are determined by the combination of these three factors, systematic studies of these changes may help to enable optimized reinforced properties.

2.2.4.2 Possible reinforcing mechanisms

(1) GNP and CNT pullout

In conventional composites, reinforcement pullout is the main toughening mechanism due to the weak interfacial connection of reinforcement with the matrix. During the pulling-out process, the frictional force between reinforcement and matrix consumes the crack energy and the crack propagation is reduced, thus resulted in higher toughness. In nanocarbon reinforced composites, graphene and carbon nanotube are nanostructured reinforcements that have larger interaction surfaces with matrix to

undergo frictional forces during the pullout process, thus leading to more work done and energy consumption during the process. In addition, graphene and carbon nanotube can be arranged in various directions in composites, which enables the higher reliability of this toughening mechanism in all directional cracks.

(2) Crack deflection

The crack deflection in nanocarbon CMCs can effectively hinder crack growth in the already existed cracks. As GNPs/CNTs' intrinsic properties are extremely high, cracks in their composites materials do not penetrate the GNP/CNT during crack propagation. In fact, the cracks grow along the GNP/CNT and thereby follows a curved path along nanocarbon and ceramic surfaces.

(3) Crack bridging or necking

Figure 2.7 shows the crack bridging or necking toughening mechanism [62]. In this mechanism, CNT or GNP bridges two crack surfaces and the relative displacement between two crack surfaces are inhibited by alleviating the stress required for further crack propagation.

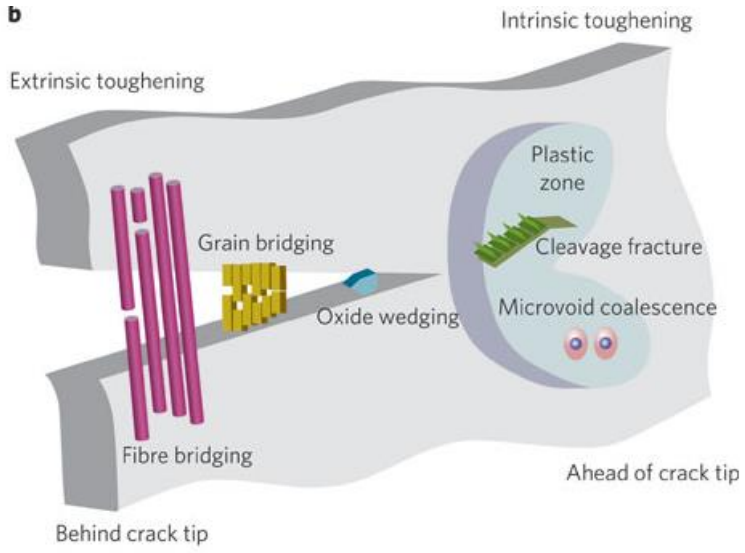

Figure 2.7 Schematic illustration of crack bridging by tube and plate reinforcements [62].

(4) Grain growth inhibition:

The GNPs or CNTs that uniformly dispersed in the matrix will anchor around the matrix particles. During sintering, grain boundary migrations are precluded by the pinning effects of GNPs and CNTs. The reduced grain boundary migrations result in less grain growth, especially grain coarsening and abnormal grain growth to have fine structures of the sintered products [63, 64].

2.2.5 Fabrication of nanocarbon reinforced bioceramic composites

2.2.5.1 Introduction

The mechanical and tribological properties of nanocarbon based bioceramic composites are strongly affected by the densification process in the course of nanocarbons based CMCs fabrication [65]. Achieving nearly full density and obtaining fine microstructure are the fundamental requirements because the density and microstructure affect the

monolithic and CMCs in most of the cases. In terms of using nanocarbons as reinforcements and bioceramic as matrix material, reducing the sintering temperature and dwell time are two critical factors in this process. First, the defects and degradation of nanocarbons could be minimized to retain the favorable properties of nanocarbons [66, 67]. Second, the fine and uniform microstructure of the composites could be achieved to maximize the performance [30, 68].

From the previous investigations, several authors have reported the degradation of the nanocarbons during conventional pressureless sintering because high temperature and long dwell time are required in this technique [69]. In comparison with the conventional sintering, some novel sintering techniques, such as hot pressing (HP) or hot isostatic pressing (HIP) [70, 71], microwave sintering [72] and spark plasma sintering (SPS) [73] are becoming increasingly popular to densify the samples.

Among these techniques, SPS is the most widely used and advantageous technique as it reduces the sintering temperature for hundreds of degrees and dwell time from several hours to minutes due to the aid of simultaneous pressure, electricity and vacuum ambiance [74, 75].

2.2.5.2 Spark plasma sintering

Figure 2.8 shows the schematic illustration of the SPS working principle. During sintering, powders are inserted into the graphite punches and dies, which are fast heated with high heating rate (the typical value is 100~600 °C/min) and then held at the desired temperature during dwell time, and uniaxial pressure (below 100 MPa due to the

strength of graphite die [76]) is applied across the specimen simultaneity. Heat is generated by the Joule effect of the pulse current flowing through the powder and the container. The parameters affecting sintering include dwell temperature, heating and cooling rates, hold pressure, and load application and removal rates [77].

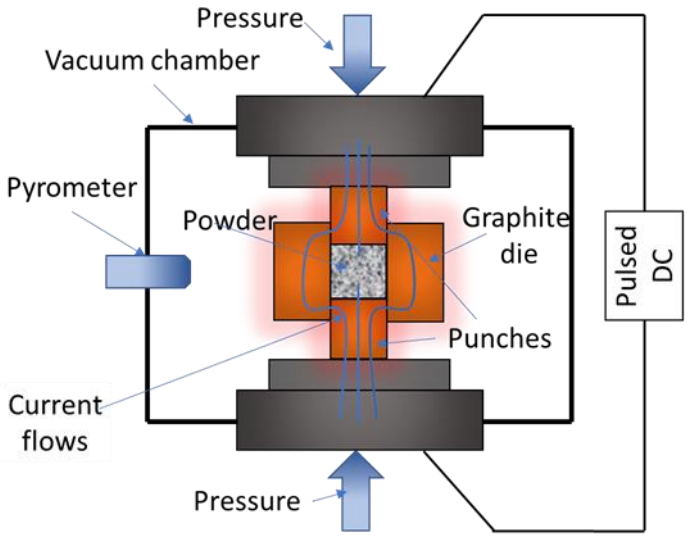

Figure 2.8 A schematic of the SPS process.

Andy Nieto successfully consolidated bulk graphene by spark plasma sintering under the condition of 1850 °C hold temperature and 80 MPa pressure [78]. This proves the feasibility of graphene to withstand extremely high temperature and pressure during SPS, which are inevitable for CMC densification by SPS [79]. Other researchers have also proved the existence of graphene in the SPSed CMCs.

2.2.5.3 Nanocarbon reinforced bioceramic composites

As discussed previously, HA is a significant category of bioceramics and has been widely used in clinical applications, but the applications in load-bearing areas are limited. Several researchers have studied graphene based HA composites by various

methods and demonstrated it is an efficient strategy to enhance the properties of bioceramics. The matrix, nanofillers type, nanofillers content, processing method and investigated properties of publications on this topic are listed as Table 2-5.

Table 2-5 Publications of graphene-based HA composites.

HA type	Graphene type	Filler content	Processing method	Investigated properties	Ref.
-	-	0, 3 vol% 5 vol%	SPS 900,1000,1100°C: 20min	Directional properties (normal and parallel to applied pressure)	[80]
Nanotube-HA Self-synthesized [81]	GO	0, 0.5 wt% 1.0 wt% 1.5 wt%	HIP 250 MPa pressed to discs 1150 °C, 160 MPa, 1h, Ar gas	Compared with pure HA Mechanical: E 186%, K_{IC} 140% Biological: increased osteoblast adhesion and proliferation	[7]
Rod-like HA length:55 nm diameter: 13nm	Graphene Oxide (GO) colloid solution (2mg/ml) [82]	40 wt% 60 wt% 80 wt%	One-pot synthesis Solution A: 94mg $Ca(NO_3)4H_2O$ add into 30 ml GO solution; then 60 min sonication; Add 40 mg CTAB; then 60 min sonication Solution B: 103.2 mg trisodium citrate and 31.56 mg $(NH_4)_2HPO_4$ mixed in 15ml ultrapure water Add solution B into Solution A sonication for 30 min; then sealed under 180 °C/ 24h	Mechanical: nanoindentation, displacement 200 nm Hardness: 242.06 ± 7.28 MPa Young's modulus: 6.20 ± 1.67 GPa twice of pure HA Biological: 40 wt% HA composites show higher cell adhesion and proliferation, better biocompatibility, and good bone bonding ability	[83]
Hierarchical flake-like HA grown on GO/Mg matrix substrate, with Ca/P ratio equals to 1.65	Graphene Oxide (GO) prepared using a modified Hummers method[84]	-	Biomimetic mineralization; Dip coat GO on Mg alloy; Culture the composite matrix in modified simulated boy fluid (m-SBF)	Mechanical: electrochemical measurement and soaking test were done, with the improved corrosion resistance of Mg alloys	[25]

HA type	Graphene type	Filler content	Processing method	Investigated properties	Ref.
				Biological: Growth time, pH, Ca^{2+} were studied	
Self-synthesized nanosized HA powder, using a modified chemical precipitation method[85, 86]	Graphene nanoplates (GNPs) average 30-50 layers, diameter 12nm, purity 99.2%, from Graphene Supermarket	1 wt%	Electrodeposit HA/Gr composite on Ti	Mechanical: compared with pure HA, reduced surface cracks; double hardness, 14.8 ± 2.0 GPa; 150% elastic modulus, 190.9 ± 18.0 GPa Biological: high bioactivity, confirmed by the formation of apatite layer after 7 days soaking in SBF, by XRD and FESEM	[87]
Nano-sized Ag/HAP powder prepared utilizing modified chemical precipitation method[85, 86] rod-like grain structure	Graphene nanoplates (GNPs) average 30-50 layers, diameter 12nm purity 99.2%, from Graphene Supermarket	1 wt%	Electrophoretic deposition (EPD) silver/hydroxyapatite/graphene (Ag/HAP/Gr) composite coatings on titanium substrate	Coatings with a more uniform surface and less micro cracks; Mechanical: Better thermal stability (TGA); H and E_r 10% higher Biological: Graphene facilitates optimal Ca/P ratio(1.52) for better bone integration; *In vitro*: noncytotoxic, antibacterial against *S.aureus* and *E. coli*	[88]
HA powders prepared from eggshell[89], 66nm in size, formed agglomerates 5-20μm	Graphene nanoplates (GNPs) 13.7 nm, 40 layers	2 wt%	SPS (HD P5, FCT GmbH) 700 and 900 °C, 5 and 10 min; diameter 3 cm, thickness 5 mm	Relative density ~ 96% at 700°C Mechanical: Hardness 4 GPa, bending strength 119 MPa, with HA elongated grains 300 nm long.	[90]
Nanoparticles Nanjing Emperor Nano Material Co., Ltd., China.	Graphene Oxide (GO) Angstron Material LLC, USA.	0, 2 wt% 5 wt%	Electrophoretic deposition (EPD) cathodic electrophoretic deposition process on Ti	Reduced surface cracks; Increased coating adhesion strength: 1.55 ± 0.39 MPa to 2.75 ± 0.38 MPa (2 wt%) and 3.3 ± 0.25 MPa (5 wt%);	[91]

HA type	Graphene type	Filler content	Processing method	Investigated properties	Ref.
			substrate	Higher corrosion resistance in SBF (Potentiodynamic polarization and electrochemical impedance spectroscopy) 95% cell viability (2 wt%), 80-90%(5 wt%)	
Nanoparticles Nanjing Emperor Nano Material Co., Ltd., China.	Graphene Oxide (GO) Angstron Material LLC, USA. (product ID: N002-PD; Lot #: D2110810-1)	0, 0.5 wt% 1.0 wt% 1.5 wt%	Electrophoretic deposition (EPD) graphene oxide-hyaluronic acid-hydroxyapatite (GO-HY-HA) coating on Ti substrate	Zeta potential: −69.1 ± 1.7 mV (0.0 wt% GO) to −76.8 ± 2.6 mV (1.5 wt% GO). Good stability and negatively charged. Raman: D-band 1355^{-1}, G-band 1593^{-1}, peak intensities increase with GO contents increasing. Deposition yield increased with GO contents increasing.	[92]
Spindle-like HA nanoparticles were randomly and strongly decorated on the surface or aggregated at the edges of GO-based substrate. Diameter: 27 ± 7 nm Length: 150 ± 25 nm	graphene oxide (GO) and chitosan (CS) functionalized graphene oxide(CS-GO)	-	Solution-based *in situ* synthesis GO and CS-GO as templates to decorate HA nanoparticles on the GO based matrix.	Mechanical: Increased elastic modulus and hardness Biological: *in vitro* cytotoxicity-CCK-8 assay on L-929 cell line and MG-63 cells. CS-GO-HA higher cell viability and alkaline phosphatase activity than GO-HA.	[93]
HA particles nucleated randomly on both sides of rGO	Graphite (500 meshes) from Acros Organic Company, were reduced to rGO. 10 ml 1 mg mL^{-1} GO aqueous suspensions mixed with 10 mM 2	-	Biomimetic mineralization Reduce and surface functionalize GO by one-step oxidative polymerization of dopamine (PDA)	UV−vis absorption spectra, optical absorbance: GO reduced to rGO by PDA; FTIR/ XPS spectroscopy: functionalization and reduction of GO	[94]

HA type	Graphene type	Filler content	Processing method	Investigated properties	Ref.
	mg mL^{-1} dopamine hydrochloride buffer solution; sonic dismembered for 1 h and magnetically stirred for 11 h.		Incubate substrate in SBF (1.5X), HA particles grown.	etc. Dopamine: reduce GO to RGO; improve RGO and calcium ions' interaction; promote HA nanoparticles nucleation. Biocompatibility: MTT assay	
Rod-like HA, length ~20–45 nm, diameter ~10 nm synthesized using wet chemical approach, stoichiometric reaction$(NH_4)_2HPO_4$, $Ca(NO_3)_2$, and $NH_3 \cdot H_2O$	Graphene Nanoplates (GNPs) Fabricated from high purity flakey graphite, height 0.8–1.1 nm, lateral dimensions ~4 μm	-	Vacuum cold spraying HA/ HA-GN coating on Ti at room temperature	Mechanical: MST test, adhesive strength improved Biological: *in vitro* cell culture, osteoblast cells moved to and anchored by GN, enhanced attachment and proliferation of cells on GN-based coating.	[95]
Rod-like HA, diameter 9 nm, length 20–45 nm, wet chemical synthesized	Reduced graphite oxide(rGO) 2–6 layers of graphene thermal reduction processing at 200 °C for 30 min in vacuum (0.1 Pa)	0, 0.1 wt% 1.0 wt%	Synthesized: liquid precipitation Consolidation: SPS (950 °C, 30 MPa, 3 min, ~5 Pa)	HA samples with enhanced densification and reduced grain growth Mechanical: K_{IC} 3.94 MPa $m^{1/2}$, 203% increase compared with pure HA (Vickers indentation approach); Biological: enhanced proliferation of the osteoblast cells(human osteoblast cells, HFOB 1.19 SV40 transfected osteoblasts)	[96]
-	RGO by procedures: GO prepared from graphite powder with Hummers method[82], GO dispersed in ethylenediamine (EDA) and dried.	-	Chemical precipitation GNPs (40 mg) dispersed in 40 ml DI water, 5 min sonication, add $Ca(OH)_2$, 1 h stirring, add H_3PO_4 until PH=9, then dried.	FTIR: confirm oxygen functionalities on GO, deoxygenation of GNPs, HA on GNPs; FESEM: sandwich-like GNPs/HA structure;	[97]

HA type	Graphene type	Filler content	Processing method	Investigated properties	Ref.
				EDS: Ca to P ratio 1.67; TEM: strong interaction between GNPs/HA Raman: G- and D- bands shifted downwards, ID/IG increased.	
Self-assembled HA nanoparticles with rod-like morphology	Oxidized carbon nanotubes (oCNTs) CNTs in 9.5 M HNO_3 for24 h and 18 h, CNTs from Nanocyl Co., Belgium, Nanocyl^{TM} NC7000 MWCNTs, 90% carbon purity Graphene oxide (GO) self synthesized: i. graphite oxide prepared using modified Hummers' method with graphite powder (Sigma–Aldrich Co. St. Louis, MO, Ref. number 332491); ii. Graphite oxide powder dispersed in concentrated ammonia, 1 h ultrasonication.	-	Wet in-situ precipitation nHA synthesized on oCNTs and GO: 2 g $CaCO_3$ dissolved 100 ml of H_3PO_4 (0.3 M in DI Water); add to 100 ml concentrated NH_4OH; keep stirring and PH > 10; dry the precipitate	Functionalization degree and CNTs/GO morphology controlled the shape and crystallinity of grown HA nanoparticles. Biological: *in vitro* tests showed fast apatite biomineralization, depending on crystalline size and dispersion degree;	[98]
-	Carbon nanotubes (CNTs) functionalized using concentrated 3 sulfuric acid:1 nitric acid at 70°C[99]; Graphene nanoplates (GNPs) by reduction of graphite oxide (GO) by Hummers and Offeman	-	*In situ* deposition GNPs (50mg) or f-CNTs (200mg) dispersed in 50 ml DI water, 5 min sonication; add $Ca(OH)_2$(0.01 mol $L^{-1)}$ and 1 h in ambient; add H_3PO_4 to PH 9; centrifuged, washed (DI water)	FTIR/XRD: HA grafted on f-CNTs and GNPs; SEM: HA grafted on both sides of both materials; Biological: the CNTs-HA and GN-HA supports proliferation and differentiation of human fetal	[100]

HA type	Graphene type	Filler content	Processing method	Investigated properties	Ref.
	method[82].		and vacuum dried.	osteoblastic cell hFOB 1.19	
-	Graphene oxide (GO) nanosheets prepared using modified Hummers method	-	Biomimetic mineralization First, peptide nanofibers (PNFs) were self-assembled; Second, Graphene oxide (GO) nanosheet was modified with PNFs to prepare GO-PNF hybrid; Third, GO-PNF serve as template for biomimetic mineralization.	GO-PNF facilitates the nucleation and growth of hydroxyapatite (HA); Short-term along PNFs' axis, long-term HA microsphere on GO. Good biocompatibility and enhanced proliferation with L-929 and MC3T3-E1 cells.	[101]
-	Graphene oxide (GO) nanosheets prepared using modified Hummers method	-	Biomimetic mineralization Layer-by-layer (LBL) assemble graphene oxide (GO) nanosheets and fibrinogen nanofibers (Fg NFs) on a silicon substrate; then incubate the scaffold in 1.5x simulated body fluid	Hierarchical 3D (GO–NF)10–HA scaffold was fabricated by LBL assemble and mineralization; Fg NFs promote nucleation and growth of HA crystals along the axis; L-929 cells proliferated on the fabricated scaffold	[102]
HA colloidal suspensions were prepared from Li's method[103]	GO aqueous suspension from Graphene Laboratories Inc., Calverton, NY, USA; 6.2 mg mL−1; lateral dimensions 0.5–5 μm.	0, 20 wt% 30 wt% 40 wt% 50 wt% 80 wt%	Colloidal chemistry synthetization Colloidal solution mixing: 6.45 mL GO suspension, 0.15 mL of aqueous ammonia (28–30 wt%) and HA colloidal were mixed to 10 mL; Hydrothermal treatment: 2 min ultrasonication, 180 °C 6 h; Dialysis: 5 d.	Free-standing and homogeneous graphene/ hydroxyapatite (HA) hydrogels were prepared; Mechanical: yield stress and elastic modulus decrease at low or high HA content; Biological: rGO and G/HA-40 constituents show high cell viability with mouse MSCs	[104]

HA type	Graphene type	Filler content	Processing method	Investigated properties	Ref.
-	GO sheets aqueous dispersion functionalized with gelatin	-	Electrochemical deposition HA/f-GO(gelatin) deposited on TiO2 nanotube arrays (TNs)	Mechanical: porous and thicker coating with gelatin and graphene oxide incorporation, with better bond strength and corrosion resistance; Biological: enhanced cell viability (osteoblasts cells, OB; MCT3T3-E1.	[105]
HA nanorods from Nanjing Emperor Nano Material (Nanjing, China), length: ~100 nm, diameter: ~30 nm	Graphene Nanosheets from ACS Material (MA, USA), thickness: ~0.8 nm, diameter: 0.5–2μm GNS suspension 0.1 mg/ml, sodium dodecyl-benzene sulfonate (SDBS) dispersant	0, 0.5 wt% 1.0 wt%	Spark plasma sintering (SPS) 1150 °C, 40 MPa, 150 °C/min, 3 min	Mechanical: 1.0 wt% GNS/HA show ~180% fracture toughness; various toughening mechanisms investigated; Biological: *in vitro*, enhanced osteoblast adhesion and apatite mineralization (Mouse osteoblast cells, MC3T3-E1)	[106]
-	Graphene oxide (GO) nanosheets prepared using modified Hummers method	-	Biomimetic mineralization		[107]

Notes: vol% - volume percentage, wt% - weight percentage,

2.3 Summary

To some extent, the field of hard tissue engineering is one of the most important areas because it is related to the health of human beings. Bioceramics, such as hydroxyapatite, are attractive candidates for the body's hard tissues replacement. However, bulk HA is poor in mechanical strength. To extend bioceramics' clinical applications, the design and dispersion of nanocarbons into the HA matrix and the consolidation process is of prime importance, because the final properties of the composites strongly depend on it. In general, work on graphene and carbon nanotube reinforced bioceramic composites is in its early stage. To maximize the reinforcing effects of nanocarbons in bioceramics, there are still considerable works regarding processing, microstructure and interfacial properties that need to be done.

Chapter 3 Methodology

3.1 Raw materials

The HA nanorods used in this thesis were produced by a wet chemical precipitation method. The detailed fabrication method was described elsewhere [108]. Reduced graphene oxide (rGO) nanoplates, multiwalled carbon nanotubes (CNTs) and graphene oxide (GO) were the three types of nanofillers used in the experiments. Cetyltrimethylammonium bromide (CTAB) was used as the surfactant for rGO and CNT to be dispersed in water and was purchased from Sigma-Aldrich (H5882).

Table 3-1 Specifications of the raw materials.

Material	Formula	Physical Shape	Size (nm)	Density (g/cm^3)	Melting point (^oC)
HA	$Ca_{10}(PO_4)_6(OH)_2$	Particle	<200	3.156	1650
rGO	C	Nanoplate	-	1.9	3652-3697
CNT	C	Nanotube	110-170	1.85	3652-3697
GO	C	Nanoplate	-	-	3652-3697

3.2 Mixing procedure

To prepare nanopowder composites, the raw powders, with HA matrix material and various nanocarbons, were mixed to obtain the composite powders. Accordingly, common procedures include:

1) Dispersion of nanocarbons separately in solution;
2) Dispersion of HA in water;
3) Final mixing of all the previously prepared suspensions;
4) Drying the suspensions to obtain nanocarbon based HA composite nanopowders for later SPS densification process.

3.3 Densification process

The mixed powders were densified by an SPS system (Dr. Sinter 1050, Sumitomo Coal Mining, Japan). According to the previous experiments from our group, the optimal operating conditions for HA densification were: 1050 ^{o}C dwell temperature and 3 min dwell time. Briefly, 0.6 gram of the mixed powder was wrapped in a graphite foil and loaded in cylindrical graphite die with an inner diameter of 10 mm. Two pieces of graphite foils were put between the punches and powders to prevent the reaction between the powders and die set and for improved current flow. An initial temperature of 600 ^{o}C was reached in 1 min and maintained at 600 ^{o}C for 3 mins. Subsequently, followed by a ramp to 650 ^{o}C in 1 min and to 1050 ^{o}C in 4 mins at a heating rate of 100 ^{o}C/min. A pressure of ~8 MPa was applied at the beginning of the SPS cycle and leave the pistol free to move unless the pressure was above 30 MPa throughout the heating period. After the temperature reaches 1020 ^{o}C, the pressure was slowly increased to 50 MPa to inhibit abnormal temperature rise and maintained at this pressure during the dwell time. The pressure was released to ~10 MPa in the cooling period. Furthermore, the sintering was performed in a vacuum environment with a residual pressure of ~4-6 Pa and sintering temperature was regulated by an infrared pyrometer focused on a small hole in the outer wall of the die. After sintering, sandpapers were used to remove the graphite foil and polish the surfaces of the samples, ranging from #180 to #4000, sequentially.

3.4 Characterization techniques

SEM is a powerful tool used to investigate the microstructural features at high magnification. In this study, a Field Emission Scanning Electron Microscope (FESEM, JEOL JSM 7600F, Japan) was used to study the morphologies of the raw powders and

mixed powders prior to SPS densification, and the surfaces of sintered samples. Prior to FESEM observation, samples were carefully fractured to the required size and cleaned with ethanol to remove any potential contaminations from the sample surface. The fractured samples were then mounted using conductive tape and gold coated for 90s to eliminate the problems associated with the charging of the sample, and to provide a better conductive path between the sample and sample holder. The Energy dispersive X-ray spectroscopy (EDS) analysis was conducted with the EDS detector equipped with FESEM to determine the wt. % of atoms and their distributions. It's noted that 2 kV accelerating voltage was used in taking FESEM images to avoid charging effect and 15 kV accelerating voltage was used in EDS analysis to obtain accurate results.

Transmission Electron Microscopy (TEM, JEOL JEM 2010 UHR, Japan) was used to obtain detailed morphological characteristics of HA and rGO.

X-ray diffraction (XRD) analysis was used to identify the phase compositions and crystallite sizes of the samples, using PANalytical EMPYREAN, The Netherlands, at 40 kV operating voltage and 40 mA operating current. For all the samples, the scanning 2θ range was 20-70° and the scanning speed was 2 °/min. The calculation of crystallite size was based on the Scherrer equation, with the instrumental peak broadening effect calibrated with a standard silicon pellet:

$$\varsigma = (k \cdot \lambda)/(\beta \cdot cos\theta) \quad (3.1)$$

Where ς is the crystallite size, k the Scherrer constant equal to 0.89, λ the wavelength of the Cu Kα X-ray equal to 0.154060 nm, and β is the full width at half maximum of the diffraction peak.

Raman scattering is a fast and nondestructive technique that provides a direct insight on the electron-phonon interactions, which implies a high sensitivity to electronic and

crystallographic structures [109], especially it can distinguish ordered and disordered crystal structures of carbon. It can be used to determine the stacking order in several layers of graphene. G-peak, which arises from the first order scattering of the E_{2g} phonon from sp2 carbon atoms (in the range of 1500–1600 cm^{-1}); D-band represents edges, other defects, disordered sp^{3-} bonded carbon atoms and impurities (in the range of 1200–1500 cm^{-1}).

Densities of the sintered samples were measured using Archimedes' method with an electronic balance of 5-decimal precision (Mettler Toledo XS105DU, Switzerland). DI water was used as the auxiliary liquid. The theoretical densities of 3.156, 1.8 and 1.8 g/cm^3 were used for HA, rGO and CNT, respectively. The mixture density (ρ) was evaluated by the rule of mixtures, as follows [110]:

$$\rho = \frac{100\%}{\frac{w_m}{\rho_m}+\frac{w_r}{\rho_r}} \qquad (3.2)$$

where w_m and w_r are the weight percentages of matrix HA and nanocarbon reinforcements, respectively. ρ_m and ρ_r are the specific weight of HA and nanocarbon, respectively. Based on equation (4.1), the mixture density, or the theoretical density of mixed composites were calculated. Five measurements were conducted for each parameter and the average values were used for relative density comparison. The densification rate was computed by dividing the measured density by the calculated theoretical density.

Nanoindentation test is a useful and popular method for measuring the mechanical properties of biomaterials. The Young's modulus and hardness of the sintered samples were measured using Agilent Nano Indenter G200, operated under continuous stiffness measurement (CSM) mode, with Poisson's ratio 0.3 for HA and rGO reinforced composites.

Fracture toughness of bioceramics is one of the most critical properties with regards to the clinical application [89, 111, 112]. In this study, the fracture toughness of ceramics was measured by Vickers indentation fracture toughness (*VI*). Vickers indentation is the most commonly used technique in determining the fracture toughness of ceramics due to the ease of specimen preparation and the simplicity of the test [113]. In this method, the extent of cracking associated with a Vickers indentation was measured to calculate fracture toughness by Anstis' equation [114]:

$$K_{IC} = 0.16 \left(\frac{E}{H}\right)^{\frac{1}{2}} \left(\frac{P}{c_0^{\frac{2}{3}}}\right) \qquad (3.3)$$

where E and H are the modulus and hardness of the composites measured by nanoindentation, P is the applied load and c_0 is the radical crack length.

Chapter 4 Effects of reduced graphene oxide content and mixing method on reduced graphene oxide reinforced hydroxyapatite composites

4.1 Characterization of raw powders

The morphologies of raw powders (HA, rGO, CNT, and GO), characterized by FESEM and TEM at low and higher magnifications, are presented in Figure 4.1. The HA particles were in nanorod shape with aspect ratios around 3-5. In the present study, the rGO had larger lateral diameter than GO, which was micrometer scale in rGO and sub-micrometer scale in GO powders. The diameter × length of CNT was 110-170 nm × 5-9 um, as provided by the supplier and confirmed experimentally. In raw nanocarbons materials, the TEM results indicated the wrinkled rGO layers and the defects in CNT. Furthermore, it is easy to observe that the as-received nanocarbons were not well separated that rGO and GO were stacked together, and CNTs were entangled to form agglomerates, respectively.

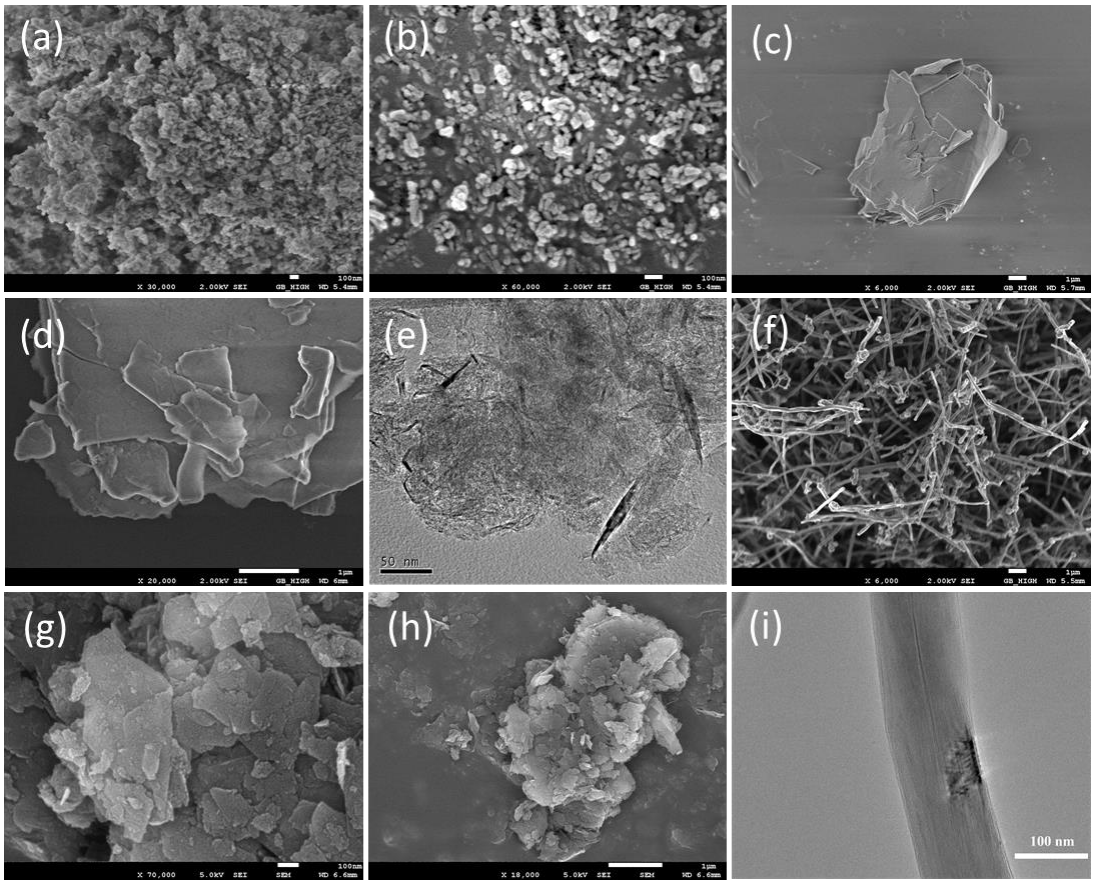

Figure 4.1 Morphologies of raw powders: (a-b) HA; (c-e) rGO; (f, i) CNT; (g-h) GO.

The compositions of rGO and CNT were confirmed by EDS mapping analysis. In Figure 4.2, (b) and (d) show the carbon atom distributions that perfectly matched the corresponded electron images of rGO, and CNT, as shown in (a) and (c).

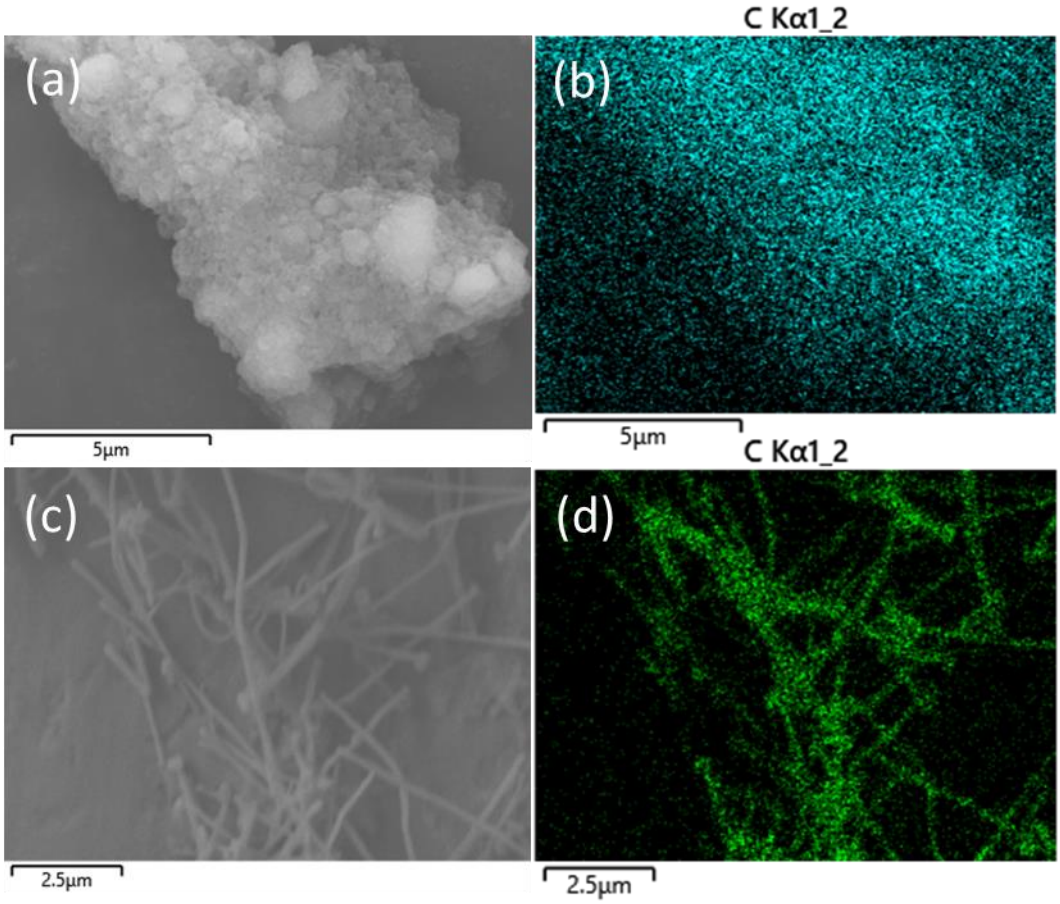

Figure 4.2 EDS analysis of raw powders: (a-b) rGO; (c-d) CNT.

The structural analysis of HA powder before processing is shown in Figure 4.3 (a). According to the reference HA patterns (PDF #96-900-2216), the characteristic HA peaks of (002), (121), (300), etc. were indexed, and the sharp shape of the peaks confirmed the high degree of crystallinity in HA.

The Raman spectra of raw HA and nanocarbon powders are shown in Figure. 4.3 (b). The strongest peak closing to 961 cm^{-1} was assigned to the v_1 vibration of PO_4^{3-} (symmetric P-O stretching mode), while the peaks around 430 cm^{-1}, 1045 cm^{-1}, and 590 cm^{-1} are $v_2PO_4^{3-}$, $v_3PO_4^{3-}$ and $v_4PO_4^{3-}$ HA bands [115-118]. It is noted that the peak positions of $v_2PO_4^{3-}$, $v_3PO_4^{3-}$ and $v_4PO_4^{3-}$ bands were indexed by the strongest peaks in each group. All the HA bands detected in this study are assigned to internal vibrational modes of the phosphate groups. In rGO, CNT and GO powders, the D peak at around

1234 cm^{-1} is a double-resonance Raman mode and can be understood as a measurement of structural disorder coming from amorphous carbon and defects. The G peak at around 1577 cm^{-1} originates from the tangential in-plane stretching vibrations of the carbon-carbon bonds within the graphene sheets. The G' or 2D peak at around 2621 cm^{-1} was the D peak overtone [119-121]. The characteristic Raman spectra peaks of the above raw materials are summarized in Table 4-1.

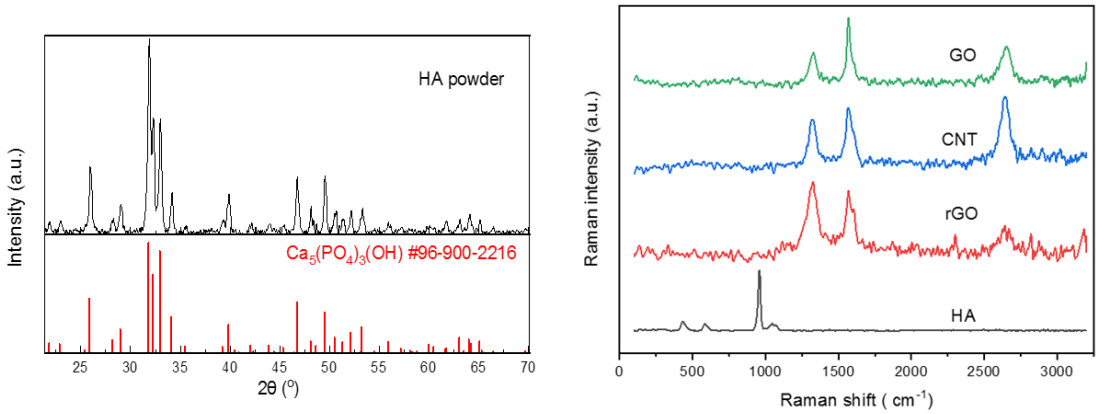

Figure 4.3 (a) XRD analysis of HA powder and (b) Raman analysis of raw powders.

Table 4-1 Characteristic Raman spectra peaks of raw powders

	$v_1PO_4^{3-}$	$v_2PO_4^{3-}$	$v_3PO_4^{3-}$	$v_4PO_4^{3-}$	D	G	2D	I_D/I_G
HA	959	430	1043	585	-	-	-	-
rGO	-	-	-	-	1328	1577	2630	1.176
CNT	-	-	-	-	1322	1565	2640	0.696
GO	-	-	-	-	1323	1577	2655	0.614

4.2 Effect of reduced graphene oxide content

In nanocarbon reinforced composites, the content of reinforcement is of vital importance in the final properties of the composites [122]. In this section, HA reinforced with various contents of rGO (1, 2, 5, and 10 wt%) were mixed by same mixing methodology (using CTAB as surfactant and DI water as solvent with the

assistance of ultrasonication) and followed by SPS under same processing conditions (1050 °C dwell temperature, 3 min dwell time, and 50 MPa sintering pressure). The microstructures of mixed powders and sintered compacts were characterized by FESEM, XRD, Raman spectroscopy, nanoindentation, and Vickers' indentation fracture toughness measurements.

4.2.1 Mixing of rGO and HA powders

Good dispersion of rGO reinforcements in the HA matrix facilitates uniform distribution of rGO in the matrix, which helps to enhance the properties of reinforced composites. Figure 4.4 shows the FESEM images and the corresponding EDS mapping analysis of the mixed rGO-HA composite powders after the drying process. HA nanorod particles remained the original shapes and were partially attached to rGO surfaces. The EDS mapping images clearly show the morphology of plate-like rGOs in the composites.

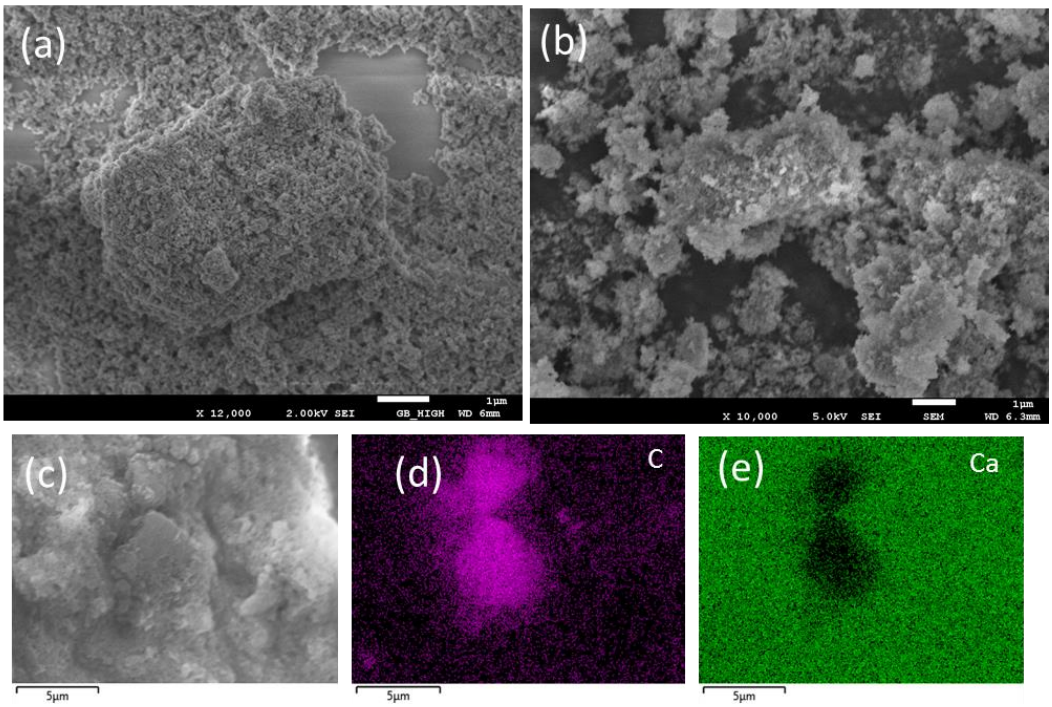

Figure 4.4 FESEM images (a-b) and EDS mappings of mixed rGO-HA powders (c-e).

4.2.2 SPS behaviors of mixed rGO-HA composites

HA and its nanocarbon-reinforced nanocomposites were consolidated using SPS with the application of pressure and heat. During sintering, densification and grain growth occur simultaneously, which determines the final properties of the sintered samples. A typical SPS processing schedule under the condition of 1050 °C dwell temperature, 3 min dwell time, and 50 MPa pressure is shown in Figure 4.5. The blue and green lines correspond to the temperature and pressure profiles, respectively. The purple line relates to the relative displacement of piston travel, and its displacement rate is shown in the yellow line. The whole process takes around 14 minutes.

The relative displacement of piston travel indicates the shrinkage of the composites. During sintering, the composites were expanded until ~780 °C due to the thermal expansion with increased temperature in the fast heating process. With further increasing the sintering temperature, the composites began to compact. The peak of the yellow line at 8 min is because of the pressure increased from ~10 to 50 MPa; while the peak at 11 min is due to the sudden reduction of pressure. The inset of the figure shows the recorded current and voltage during the whole SPS process. The voltage below 8 V and current as high as 1000 A were applied in the SPS as pulse appearance.

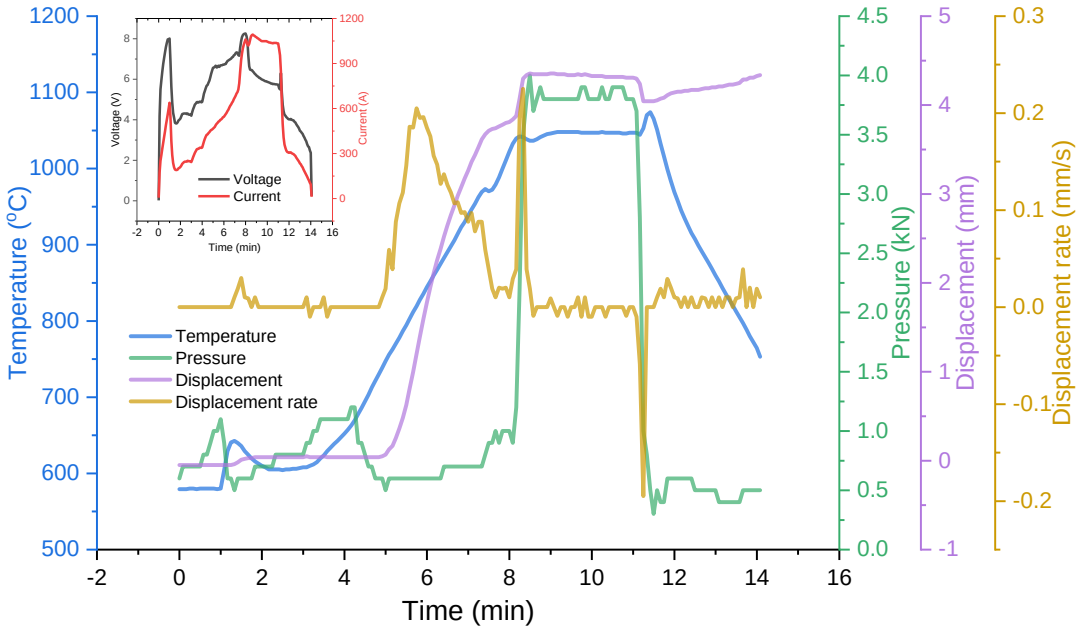

Figure 4.5 Typical SPS cycle for rGO/HA pellet sintered under 1050 °C, 3 min and 50 MPa condition, showing the profiles of temperature (blue line), pressure (green line), the relative displacement of piston travel (purple line), and the displacement rate (yellow line). The inserted figure shows the corresponding current and voltage of the power supply.

4.2.3 Characterization of sintered composites

The sintered HA and rGO-HA composites were characterized in terms of the densification rate, XRD, Raman spectra, hardness, Young's modulus, fracture toughness analyses, and microstructure analysis.

The theoretical and measured densities, and densification rates of densified HA and rGO-HA composites are shown in Figure 4.6. The theoretical densities of HA reinforced with different contents of rGO were calculated with equation (3.2), and the densification rate was calculated by dividing the measured density over calculated theoretical density for each composition. Figure 4.6 shows there was a trend of reducing the densification rate by increasing the rGO contents. In this study, the reduction in

densification rate was possibly due to the following reasons: (a) At higher rGO contents, there were more rGO agglomerated; (b) At higher rGO contents, the amount of surfactants was increased accordingly. In the high-temperature SPS process, more porosities were prone to form that resulted from the decomposition of CTAB. Despite the impediment of densification induced by rGO introduction, the relative densities of rGO-HA composites still exceeded 97.0 % with less than 2 wt% rGO addition, and this relatively high densification rate possibly guaranteed proper mechanical properties.

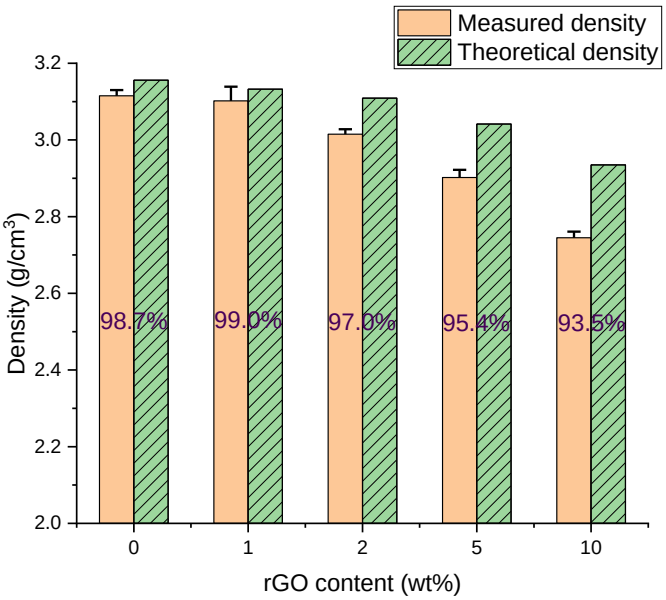

Figure 4.6 The theoretical and measured densities of HA reinforced with different content of rGO.

To assess the influence of rGO content on its dispersion quality in HA matrixes, the LABE FESEM images are provided (shown in Figure 4.7, with the black dots indicating rGO agglomerations). By visual inspection, the rGO agglomerations increased significantly with increasing rGO content. As a result, defected areas that unfavorable for the reinforcing effects were increased accordingly.

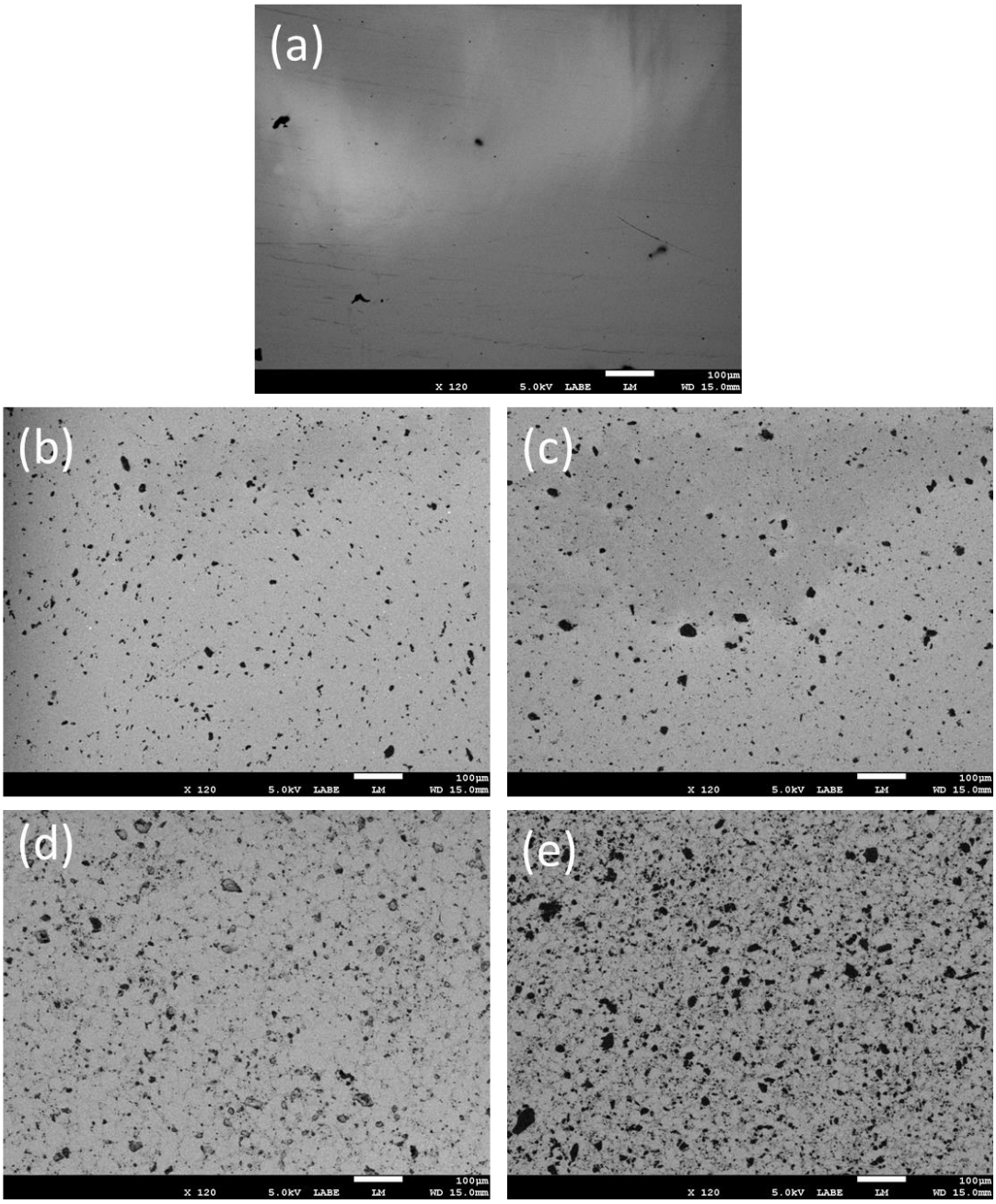

Figure 4.7 LABE FESEM observations for SPSed HA and rGO-HA composites with different contents of rGO: (a) HA; (b) 1 wt %; (c) 2 wt%; (d) 5 wt%; (e) 10 wt%.

To study the structural change caused by rGO introduction, the XRD patterns and the calculated crystallize sizes from various planes of raw HA powder, SPSed pure HA and rGO-HA composites are presented in Figure 4.8, with the α-TCP peaks marked with stars. It is clearly seen that the major peaks in the diffraction patterns are from the typical peaks of HA for all the compositions, besides a small amount of HA

decomposed into tricalcium phosphate (TCP). The characteristic peaks of rGO, a broad peak around $2\theta = 26.5°$ [123, 124], were not detected below 5 wt% rGO content due to XRD analysis nature. Similarly, this phenomenon was found in other matrixes that were reinforced with low rGO content as well [125]. However, in 10 wt% rGO based composites, this broad peak was observed and the survival of rGO after SPS process was confirmed by XRD [126].

The average crystallize sizes in all the three above planes reduced subsequently with increasing the rGO content from 2 to 10 wt%, implying the presence of rGO hinders crystallize growth of HA. This was directly related to the densification rate discussed previously. Another interesting thing is the relative length ratios for HA crystallize in a- and c- axes directions. With up to 5 wt% rGO addition, the ratios between the length and width of HA crystallizes decrease, indicating the reduction in the aspect ratios of HA crystallizes and more uniform of HA crystallizes. It is noted that the mismatch in 10 wt% rGO-HA composites possibly resulted from the low densification rate that HA crystallizes remained the aspect ratios as that of the powders before SPS. Furthermore, compared with other compositions, the crystallize growth of 10 wt% rGO-HA was much lower. It is indicated that the introduction of rGO helps hinder the growth of elongated grains and causes the formation of a finer and more homogenous microstructure.

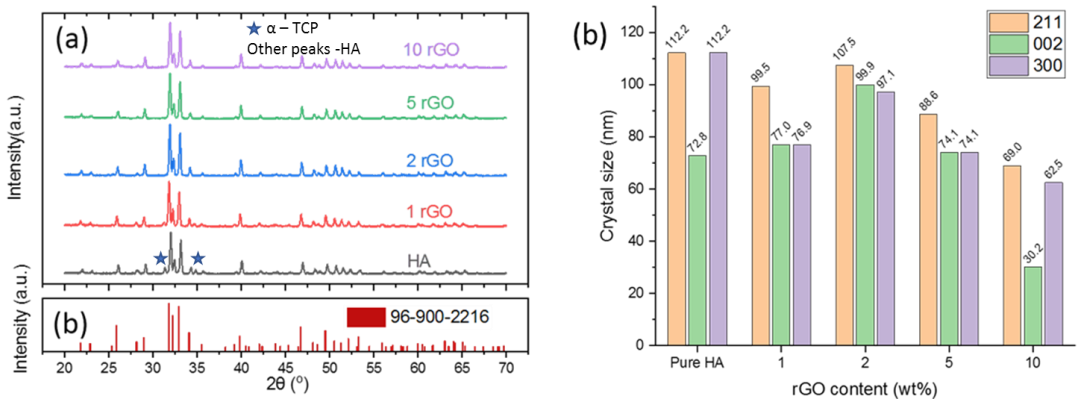

Figure 4.8 (a) XRD patterns and calculated HA crystallize size by various planes of sintered rGO reinforced HA composites.

The Rietveld refinement of HA and rGO-HA composites are shown in Figure 4.9, and the R values and the structural parameters obtained are summarized in Table 4-2. In Figure 4.9, the red lines denote experimental results, and the blue lines denote calculated results. In all patterns, the visual inspection and R values obtained provide evidence of a reasonable estimation of the structural parameters. In rGO-HA composites with rGO concentrations increasing from 0 to 10 wt.%, no systematic change in the lattice constants was observed. The small non-systematic variations in the lattice constants could be attributed to the processing of the samples.

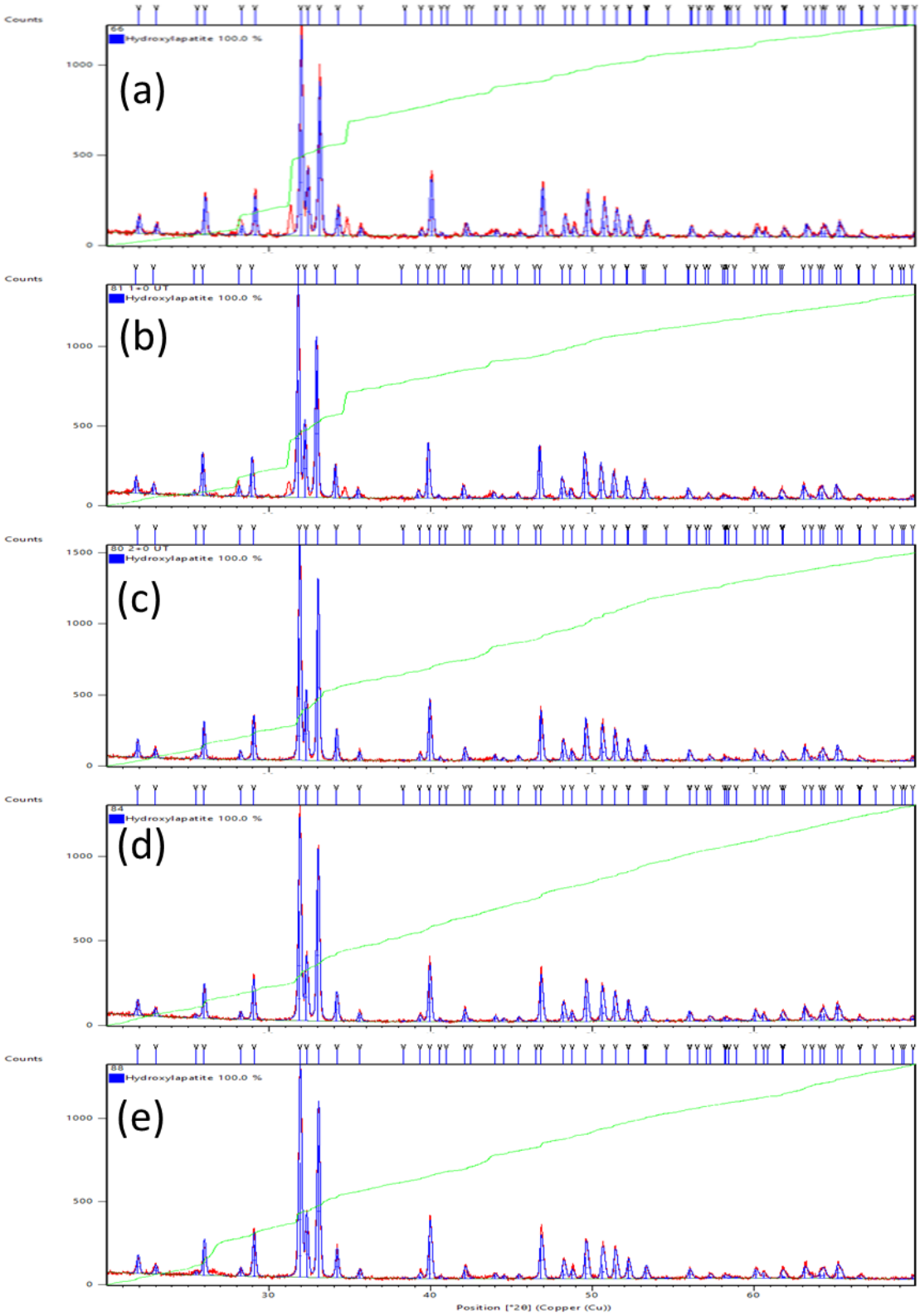

Figure 4.9 Observed (red line) and calculated (blue line) XRD patterns of HA reinforced with various contents of rGO: (a) HA; (b) 1 wt%; (c) 2 wt%; (d) 5 wt%; (e) 10 wt%.

Table 4-2 R-values and lattice parameters for HA and rGO-HA samples from Rietveld analysis

	Powder	Pure HA	1	2	5	10
R-factors (%)						
Rexp	13.085	10.784	10.860	11.248	10.510	11.380
RBragg	2.357	2.340	2.334	3.496	2.940	3.353
Rp	10.174	10.776	9.413	9.079	8.252	8.864
Rwp	13.516	15.364	13.023	11.704	10.790	11.701
GoF	1.033	1.425	1.199	1.041	1.027	1.028
Lattice parameters						
a/ Å	9.403	9.406	9.412	9.414	9.414	9.415
c/ Å	6.869	6.874	6.875	6.880	6.879	6.880
alpha/ °	90	90	90	90	90	90
beta/ °	90	90	90	90	90	90
gamma/ °	120	120	120	120	120	120
Preferred orientation direction/ hkl	1 0 0	1 0 0	1 0 0	1 0 0	1 0 0	1 0 0
Preferred orientation parameter	1.085	0.724	0.750	0.686	0.668	0.671

Raman spectra of SPSed pure HA and rGO-HA composites showed well-defined PO_4^{3-} peaks belonging to HA, and D, G, 2D bands belonging to rGO, shown in Figure 4.10. The presence of the characteristic rGO bands confirmed the survival of rGO in SPSed composites under either content. The above-mentioned characteristic Raman spectra peaks of SPSed HA and rGO-HA composites are summarized in Table 4-3. The most important difference in the Raman spectra of the SPSed compacts and the as-received rGO or HA powders (shown in Figure 4.3 (b)) was the positive shift of G bands in SPSed composites. In Raman spectra, the number of graphene layers can be expressed as $w_G=1581.6 + 11/(1+n^{1.6})$ [127, 128]. As the number of layers decreases, the G band shifts to higher wavenumber. The thinning of rGO possibly resulted from the combined effect of ultrasonication and mechanical stirring in the powder mixing process, and the SPS process. Another point to note is there was no significant change in the SPSed

compacts' I_D/I_G ratios by varying rGO contents, implying that under the same processing condition, the densities of rGO defects were similar.

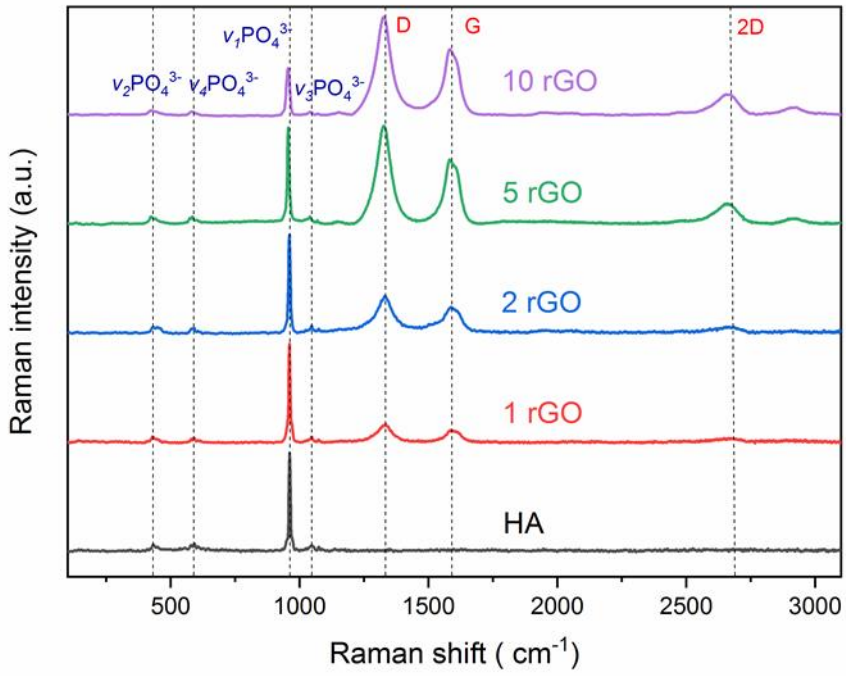

Figure 4.10 Raman spectra of SPSed HA and rGO-HA composites with different rGO contents.

Table 4-3 Characteristic Raman spectra peaks of SPSed HA and rGO-HA composites.

	$v_1PO_4^{3-}$	$v_2PO_4^{3-}$	$v_3PO_4^{3-}$	$v_4PO_4^{3-}$	D	G	2D	I_D/I_G
HA	962	430	1045	590	-	-	-	-
1	960	430	1045	589	1331	1587	2664	1.47
2	961	433	1047	588	1329	1588	2670	1.42
5	960	430	1046	590	1331	1588	2662	1.42
10	960	431	1045	588	1323	1587	2662	1.45

The fracture surfaces of SPSed compacts observed by FESEM are presented in Figure 4.11. From Figure 4.11 (a-b), the fractured HA was composed of large HA chunks.

However, the rGO-HA composites showed layered structures with smaller fractured structures, shown in Figure 4.11 (c-d). This difference may be caused by the grain refinement effect by rGO addition, as evidenced by XRD analysis. Furthermore, in SPSed rGO based composites, rGO plates tended to align in the direction perpendicular to the compressing pressure [129-131]. The microstructure refinement of the composites by adding rGOs was confirmed with FESEM as well. Figure 4.11 (e-f) show the LABE FESEM of well-dispersed rGO in the HA matrix and defected areas caused by rGO agglomerations. It can be seen well-dispersed rGOs were attached to HA grains, while damages were introduced in the places where rGOs were agglomerated.

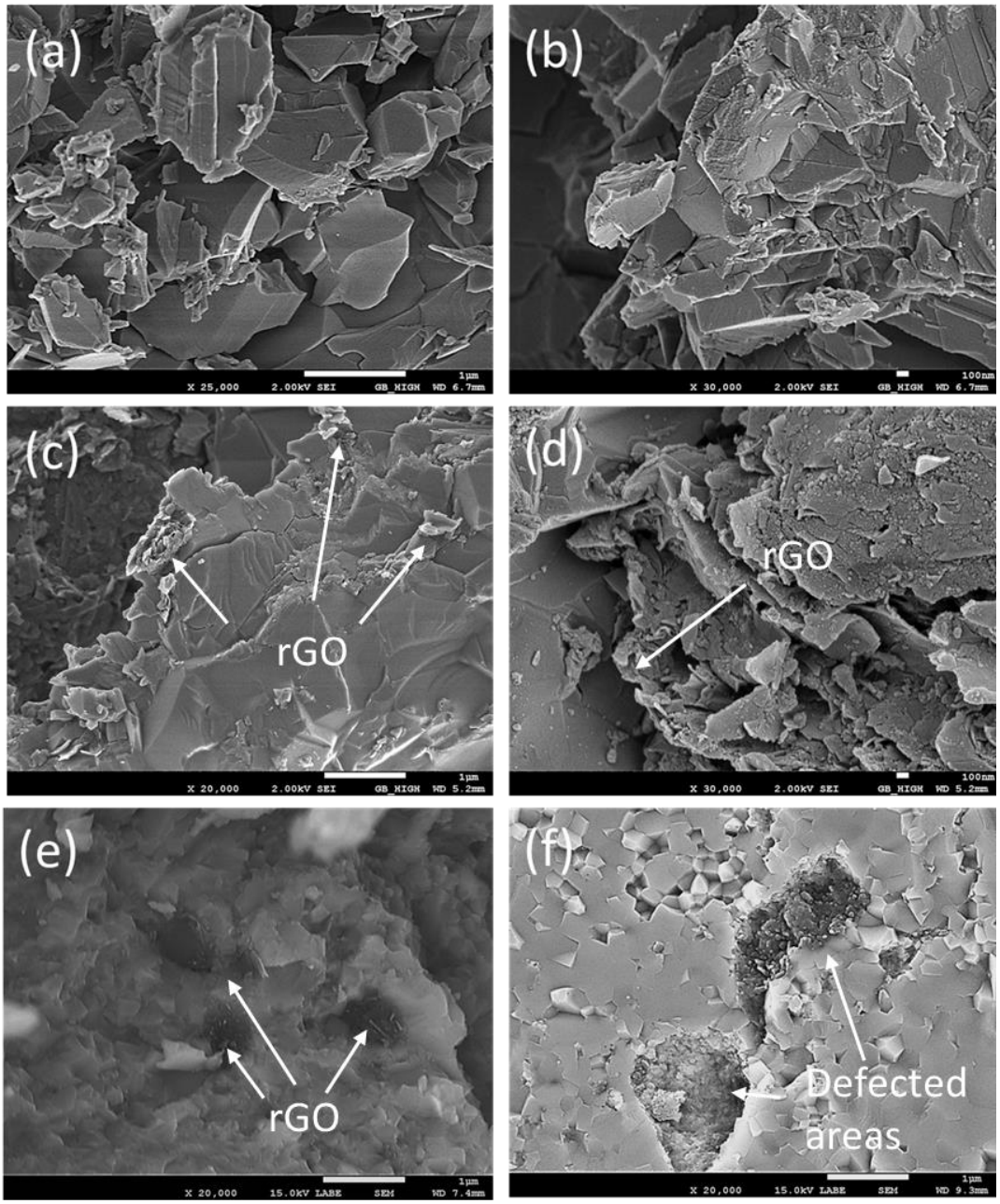

Figure 4.11 Fracture surfaces of (a-b) HA and (c-f) rGO-HA composites.

The mechanical properties of SPSed HA and rGO-HA composites are shown in Figure 4.12. The results indicate that the contents of rGO added to the composites affected the hardness, Young's modulus and fracture toughness with respect to the monolithic HA ceramic. In general, it is possible to observe that the hardness and Young's modulus of the composites shared the same trend to increase with 1 and 2 wt% rGO addition and decrease when the contents reach 5 and 10 wt%.

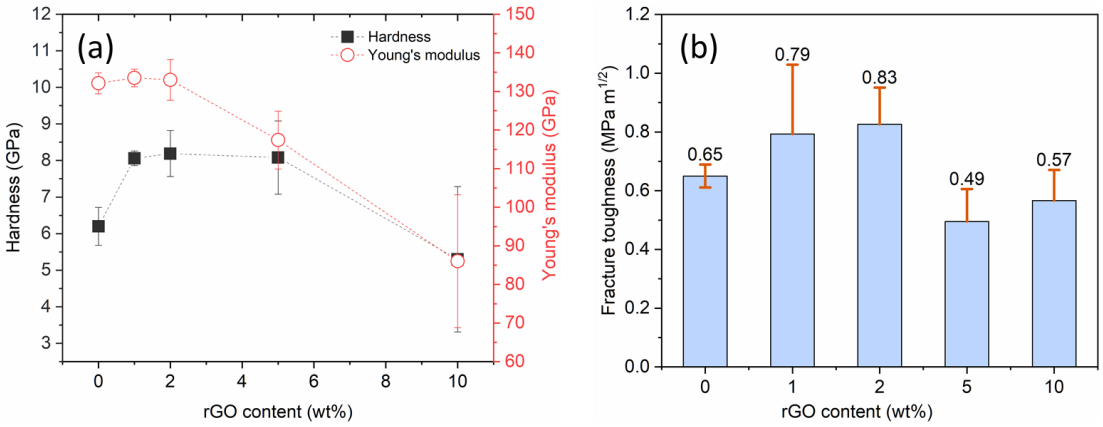

Figure 4.12 Mechanical properties of rGO reinforced HA composites as a function of rGO content: (a) Hardness and Young's modulus; (b) Fracture toughness.

In ordinary brittle materials, there is a conflict between hardness and toughness that the increase in hardness always results in the reduction of fracture toughness [62]. However, in the present rGO reinforced HA with rGO contents below 2 wt%, the hardness and fracture toughness were improved simultaneously. The hardness improvement was mainly attributed to rGO's effect on crystal structure refinement and the high stiffness of rGO, and the toughness improvement was mainly attributed to rGO's crack inhibition abilities.

To investigate the crack inhibition effect resulted from rGO addition, the cracks generated by indentation of pure HA and rGO-HA composites are compared, shown in Figure 4.13 (a-b), and the crack edges showed distinct microstructures between them. In monolithic HA ceramic, the cracks had fewer deflections, and the edges were smooth and straight. In contrast, the cracks were deflected and had finer microstructures in rGO-HA composites. Furthermore, debonded rGO pulled out from the HA matrices were observed to anchor along the crack surfaces. As a result, the crack deflection, crack bridging effects were the primary mechanisms for fracture toughness improvement.

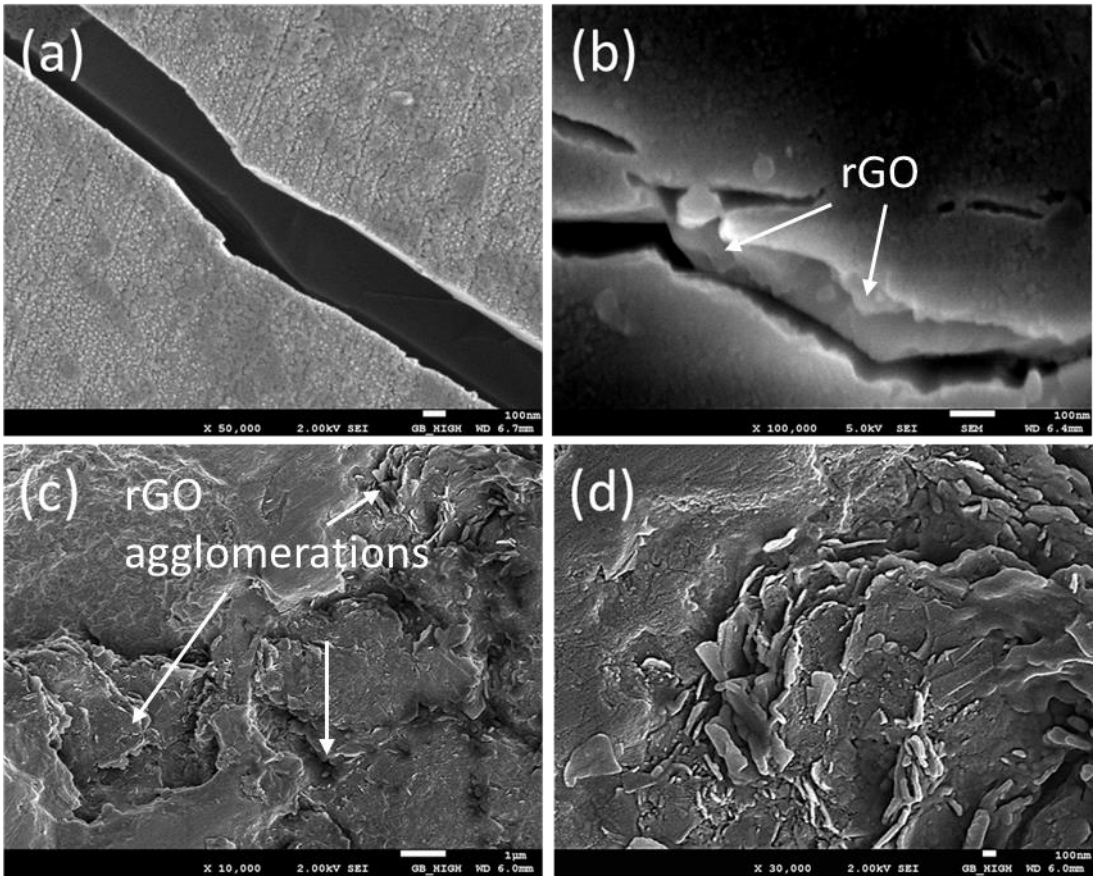

Figure 4.13 Microstructures of SPSed HA and rGO-HA composites: (a-b) crack morphologies generated by Vickers indentation; (c-d) defected areas induced by the high content of rGO agglomerates.

In the composites reinforced with a higher content of rGO, the major problem was the increased number of rGO agglomerations resulted from the increased difficulty in uniform dispersion of rGO into matrixes. Typical microstructures of rGO stacking areas at low and high magnifications are presented in Figure 4.13 (c-d). The stacking of rGO resulted in a higher discontinuity in the whole composites and the sliding between adjacent layers. In this way, the bulk mechanical properties of the composites decreased.

4.3 Effect of mixing method

It has been addressed by many researchers that the advantages of graphene in reinforcing composites can only be realized with good dispersion and distribution in

the composites [132-134]. To improve the dispersing efficiency of rGO into HA, the effects of mixing methods, classified as ultrasonication- and ball-milling- based methods, were studied. In the ultrasonication method, two methodologies were utilized: (a) using CTAB as the surfactant to disperse rGO with HA in a water solution, named as UT (C) in this section; (b) using ethanol as the solvent without surfactant, named as UT (E). In the ball-milling method, with the fixed 2h milling time, two rotation speeds were studied: (a) Lower speed at 80 rpm, named as BM (L); (b) Higher speed at 180 rpm, named as BM (H). According to section 4.2, 1 or 2 wt%, of rGO contents were optimal to reinforce HA, so a fixed content of 1 wt% rGO in composites was chosen in all the composites processed by the above mixing methods.

4.3.1 Mixing of rGO with HA by BM method

The composite powders mixed by ball milling methods at low and high speeds are presented in Figure 4.14 and the morphologies of ball milling mixed composite powders showed different microstructures relating to the milling speed. In lower speed, stacked rGO sheets were observed in BM (L) composite powders, showing a poor dispersing state of rGO. At a higher speed, HA nanorod particles were attached to rGO plates.

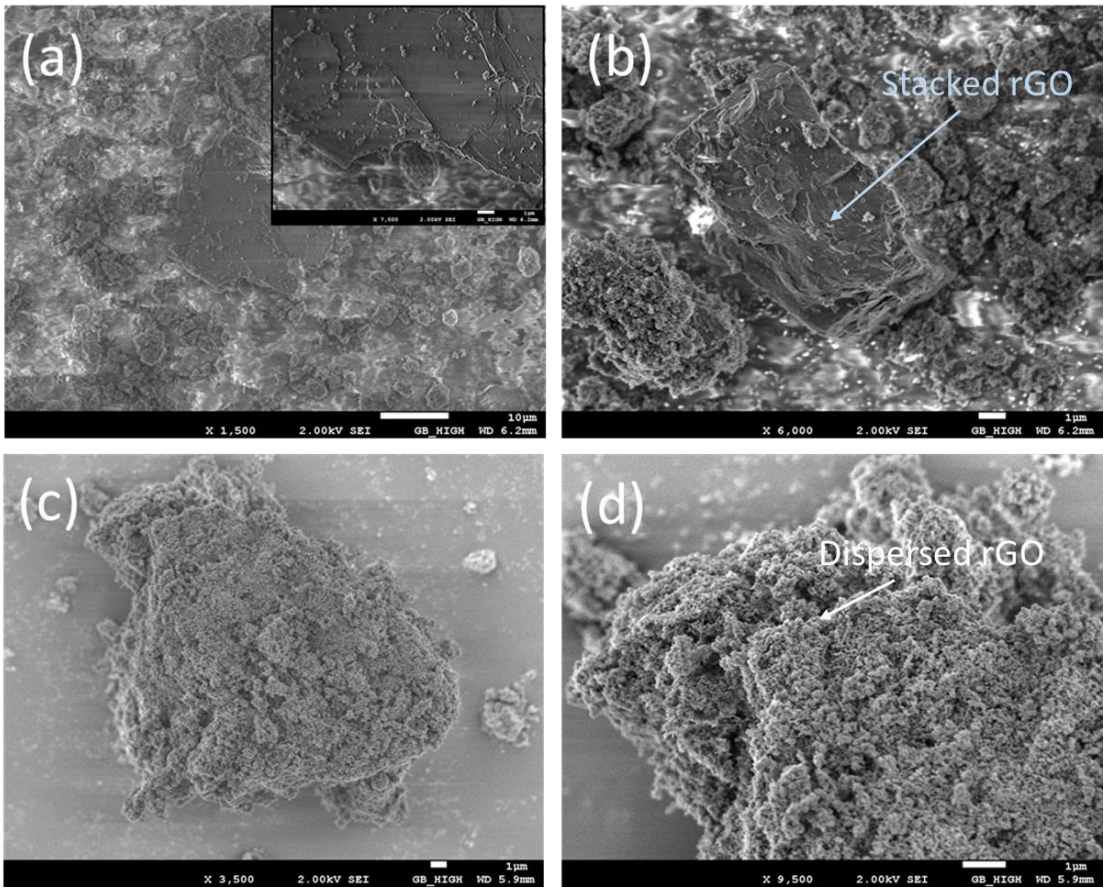

Figure 4.14 Morphologies of BM mixed powders: (a-b) BM (L); (c-d) BM (H).

4.3.2 Characterization of SPSed rGO-HA composites mixed by different methods

As shown in Figure 4.15 (a), the theoretical densities were above 98.2 % in all composites, disregarding the powder mixing methods used. There was no significant change in densities, implying with fixed rGO type and content, all the composites were almost fully densified after the SPS process. However, the mixing process of the composites influences the mechanical properties of rGO-HA composites.

The hardness, Young's modulus and fracture toughness of pure HA and rGO-HA composites mixed by various methods are summarized in Figure 4.15 (b-c). In ultrasonication mixed composites, both UT (S) and UT (E) composites had increased hardness, modulus, and fracture toughness. In addition, optimal mechanical properties

were achieved in UT(E) composites. In BMed composites, Young's modulus and fracture toughness of BM (L) sample were similar to that of monolithic HA sample, while in BM (H) sample the fracture toughness was much higher but the hardness was lower.

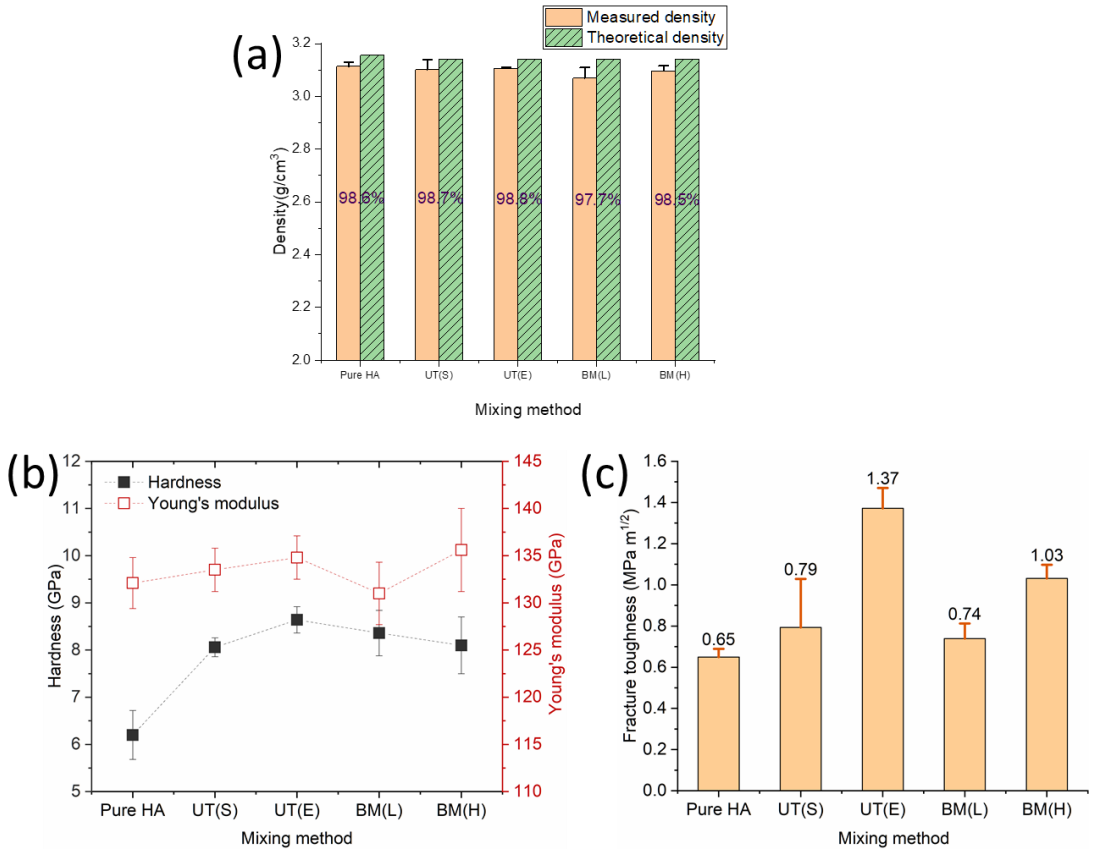

Figure 4.15 Density and mechanical properties of rGO reinforced HA composites as a function mixing methods: (a) density; (b) hardness and Young's modulus; (c) fracture toughness.

According to the XRD data in Figure 4.16 (a), the appearance of characteristic diffraction peaks of HA was observed in all samples. The crystallize sizes of UT (S), UT (E) and BM (H) were smaller than pure HA samples, while the increase of that in BM (L) samples probably resulted from the abnormal grain growth from rGO agglomerates, as the agglomerates of rGO stacked at grain boundaries assist rapid grain growth of matrixes in the densification process [135].

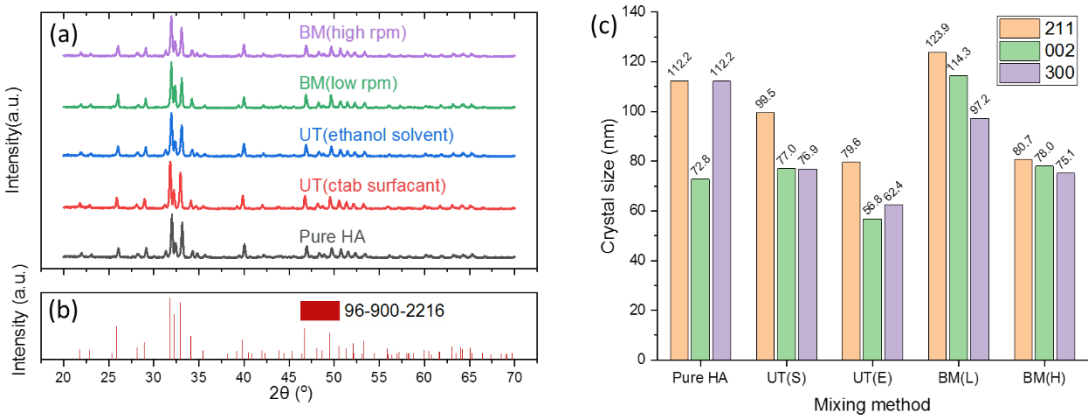

Figure 4.16 XRD patterns (a-b) and calculated crystallize sizes (c) by various crystal spacings of SPSed rGO-HA composites mixed by different methods.

Figure 4.17 presents the Raman spectra of SPSed pure HA and rGO-HA composites and all the spectra were normalized with the highest peaks, with the characteristic Raman spectra peaks listed in Table 4-4. Both HA peaks and rGO peaks were detected in all the rGO-HA composites.

The Raman spectra also showed the structural defects and thickness of rGO in the composites. In ultrasonication mixed composites, the positions of G and 2D bands were higher in UT (E) than UT (S) composites and the difference in I_D/I_G ratios between these two composites were not significant. These Raman analyses show that the dispersion of rGO was more uniform in UT (E) composites while the defects introduced were similar. In ball-milled composites, there were positive shifts in both G and 2D bands and higher I_D/I_G ratios for BM (H) samples than those in BM (L) samples. Under higher milling speeds, the destroying of rGO agglomerates and generation of defects co-occurred.

These results were related to the mechanical properties and structural analyses. Although better dispersion of rGO enhances the mechanical properties of the composites, the defects generated depress the intrinsic mechanical properties of rGO

that deteriorates the reinforcing effects. Influenced by the above synergistic effect, the optimal mechanical properties were achieved in UT (E) samples that had good dispersion and fewer defects.

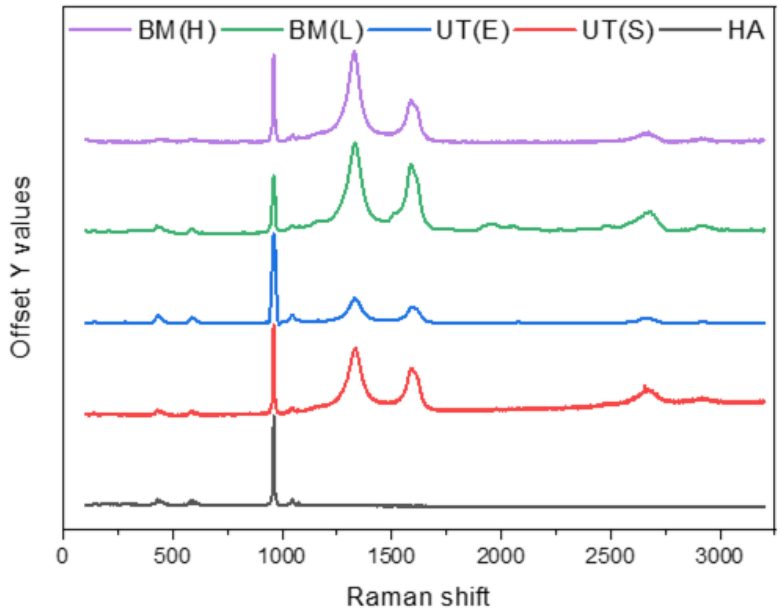

Figure 4.17 Raman analysis of SPSed rGO-HA composites processed by various mixing methods.

Table 4-4 Characteristic Raman spectra peaks of SPSed rGO-HA composites processed by various mixing methods.

Mixing method	$v_1PO_4^{3-}$	$v_2PO_4^{3-}$	$v_3PO_4^{3-}$	$v_4PO_4^{3-}$	D	G	2D	I_D/I_G
Pure HA	962	430	1045	590	-	-	-	-
UT(S)	960	430	1045	589	1331	1587	2658	1.47
UT(E)	961	430	1046	591	1334	1594	2680	1.41
BM(L)	960	430	1047	589	1333	1588	2679	1.44
BM(H)	960	433	1047	589	1329	1590	2681	2.17

As optimal mechanical properties were achieved by UT(E) mixing method, the microstructures from indentation induced radical crack and fracture surface were

studied and presented in Figure 4.18. At lower magnification, a curved and branched crack structure was observed, with the deflected and branched crack areas directly being pointed in the labeled figures. At higher magnification, it can be seen rGO was embedded inside the cracks in the direction parallel to the sample surface. In comparison with the UT(C) composites, shown previously in Figure 4.13 (a), visual inspection showed the density of rGO observed was much higher in UT(E) composites, indicating better rGO dispersion in the composites processed by this method. Thus, it is confirmed ethanol was an effective solvent to disperse rGO into the HA matrix. The fracture surfaces, shown in Figure 4.18 (c-d), indicate the characteristics of fine grains with minimum porosities in microstructure, with the rGO bonded to the HA matrix and being pointed with black arrows.

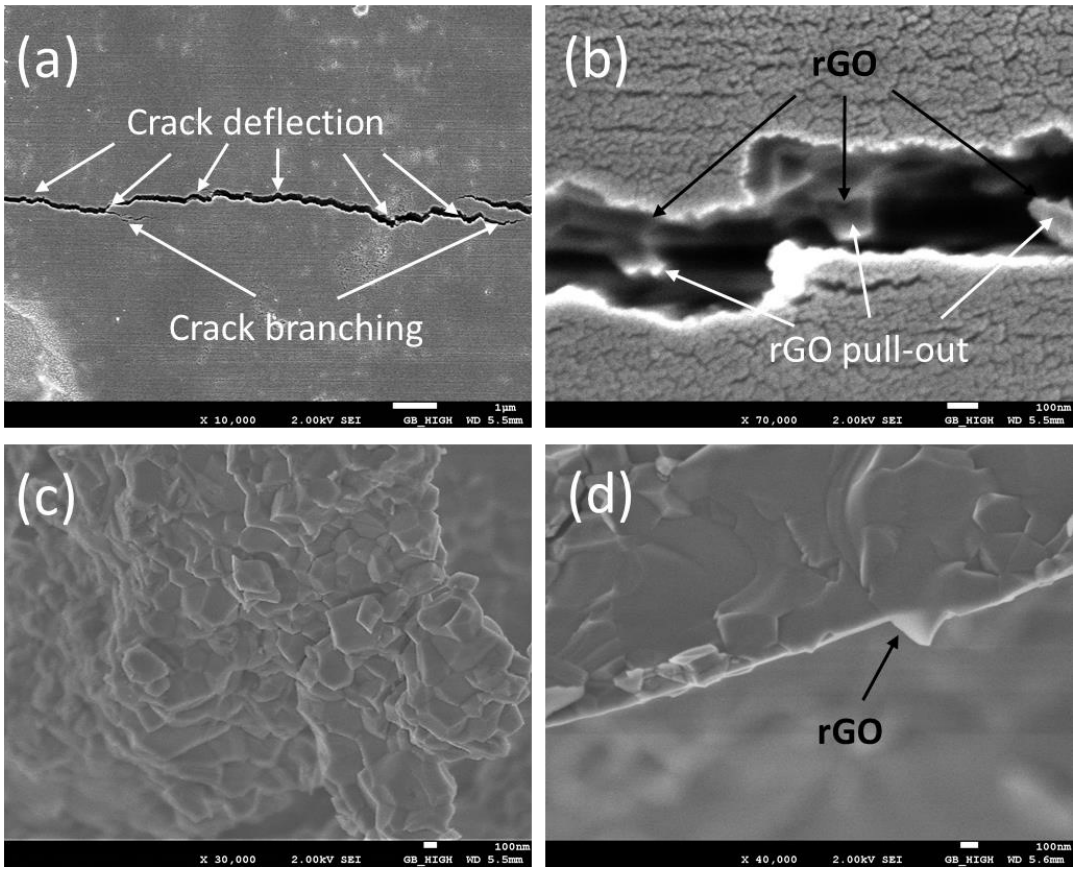

Figure 4.18 The crack generated by indentation (a-b) and fracture surfaces (c-d) of rGO-HA composites mixed in ethanol solvent with the assistance of ultrasonication.

4.4 Summary

To take the advantages of rGOs to enhance the mechanical properties of HA bioceramic, the 2 vital factors influencing the reinforced properties, namely nanocarbon content and mixing method, are studied in this chapter.

1. In terms of nanocarbon content, monolithic HA and HA reinforced with various contents of rGO (0, 1, 2, 5, and 10 wt%) were prepared and characterized. The hardness, Young's modulus and fracture toughness of the composites were increased with up to 2 wt% rGO and reduced with 5 and 10 wt% rGO as reinforcements. The improvement in mechanical properties was mainly attributed to the microstructural refinement of the composites, and the crack bridging and branching mechanisms by rGO. Furthermore, with increasing rGO concentration, the densification rate was decreased and the number of rGO agglomerations and porosities were increased.
2. In terms of mixing method, all the ultrasonication mixed and ball milled samples were almost fully densified. The hardness and fracture toughness of SPSed pellets were improved in all the rGO-HA composites and the highest values were obtained in UT (E) composite. Although high-speed wet ball milling method facilitates to well disperse nanocarbons into HA bioceramics, a large number of defects were introduced simultaneously. In contrast, the ultrasonication mixing method was superior with similar dispersion efficiency but fewer defects generated.

Therefore, the content of rGO reinforcements was up to 2 wt% to reinforce HA bioceramics and the ultrasonication mixing method was superior with better dispersion and fewer defects.

Chapter 5 Effect of carbon morphology on nanocarbon reinforced hydroxyapatite composites

5.1 Effect of nanocarbons' shape and size on nanocarbon reinforced hydroxyapatite composites

The apparent differences in carbon morphology, 1D CNT or 2D graphene, larger or smaller lateral sizes of graphene, influence the dispersion and reinforcing efficiencies of nanocarbons with bioceramics. In this section, the influence of the size and shape of nanocarbons, in the forms of CNT, rGO and GO, on their reinforcing performances in HA bioceramics were studied with the specimens prepared under the same processing conditions: ball milled composite powders were SPSed under the same dwell temperature and pressure.

5.1.1 Morphologies of mixed CNT-HA and GO-HA powders

5.1.1.1 CNT-HA composite powders

Figure 5.1 presents the morphologies of mixed CNT-HA composite powders. Compared with the pristine CNTs shown in Figure 4.1, unique structures of CNTs were formed after the ball milling process in CNT-HA composites. With directly marked in the figures, these features could be classified as: knotted tubes with nodes (shown in Figure 5.1 (a-c) under low and high magnifications), interconnected CNTs in vertical and smaller angles (shown in Figure 5.1 (d-e)), and twisted tubes with rough surfaces (shown in Figure 5.1 (f)).

In general, the formation of these structures in CNT increased the surface roughness of CNT and provided the "mechanical locking" places for improved mechanical contact

strength between CNT and HA. However, the side effects were introduced at the same time and mainly summarized to two sides: (a) the reduction in CNT's intrinsic mechanical properties that resulted from the less structural integrity of CNT [136]; (b) the shorten of CNT that might reduce the reinforcing effects [137-139].

Compared with other studies, the formation of these structures in CNT was mainly attributed to the following reasons: (a) the milling solution was water-based solution with low rGO-HA powder concentration, while most of the published ball-milled composites were performed under dry condition [140-142]; (b) The relative high ball to powder ratios and the unique ball shape used in this study.

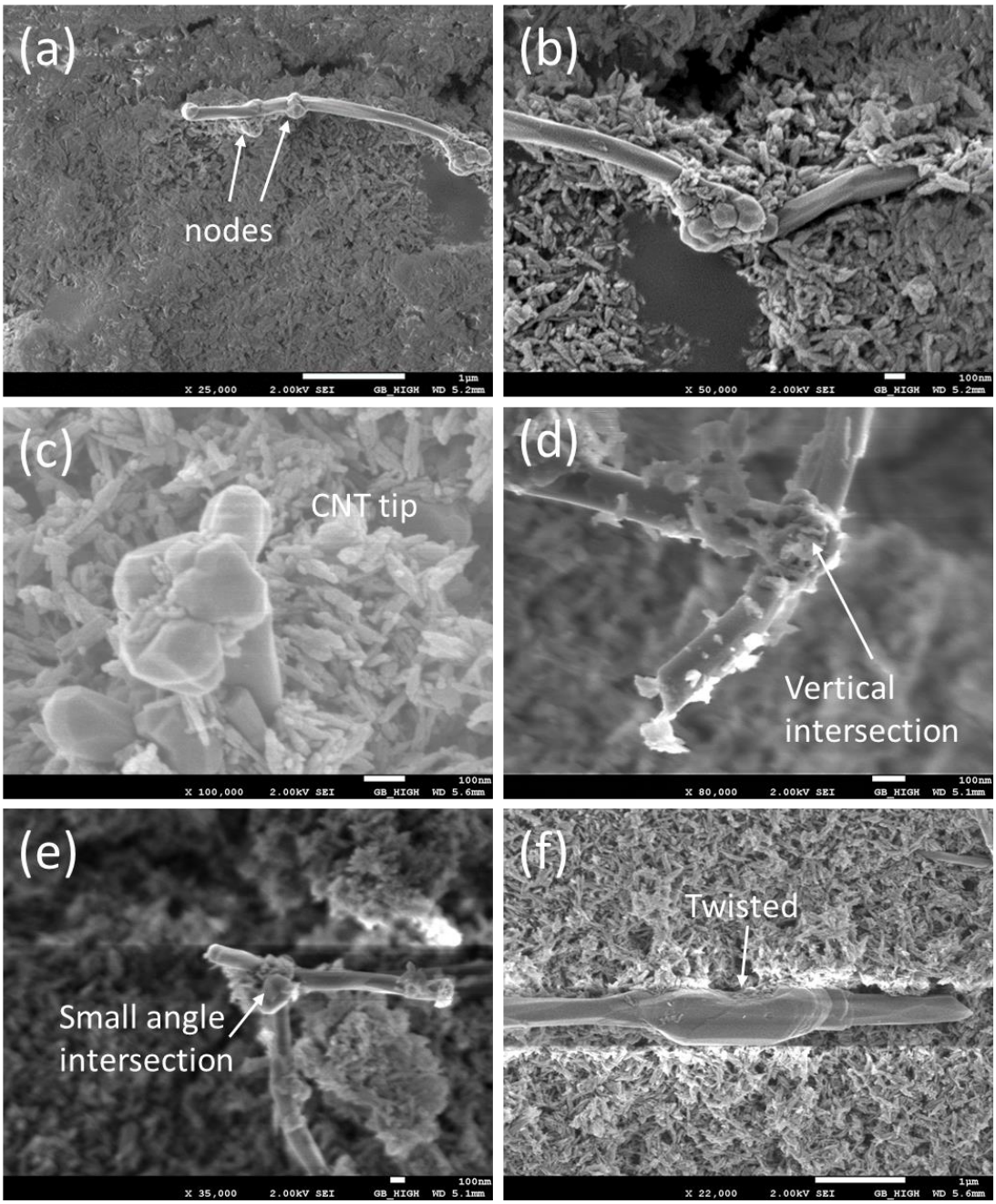

Figure 5.1 Morphologies of mixed CNT and HA composite powders.

The formation of the above unique structures proved that the high energy ball milling process provided a harsh environment for CNT. To study the ball milling process's effects on CNT, pure CNTs were ball milled under the same condition. The microstructures of ball milled CNTs are shown in Figure 5.2. By comparing the CNT morphologies shown in Figure 5.1 and Figure 5.2, the number of entanglements

between CNTs was increased while the structural integrity of CNT was higher in ball milled pure CNTs. Besides the entangles of CNTs, twined CNTs were also observed, shown in Figure 5.2 (e). In CNT-HA composites, HA nanorod particles filled the spaces between entangled CNTs. Also, CNTs were separated and broken in the complex milling environment.

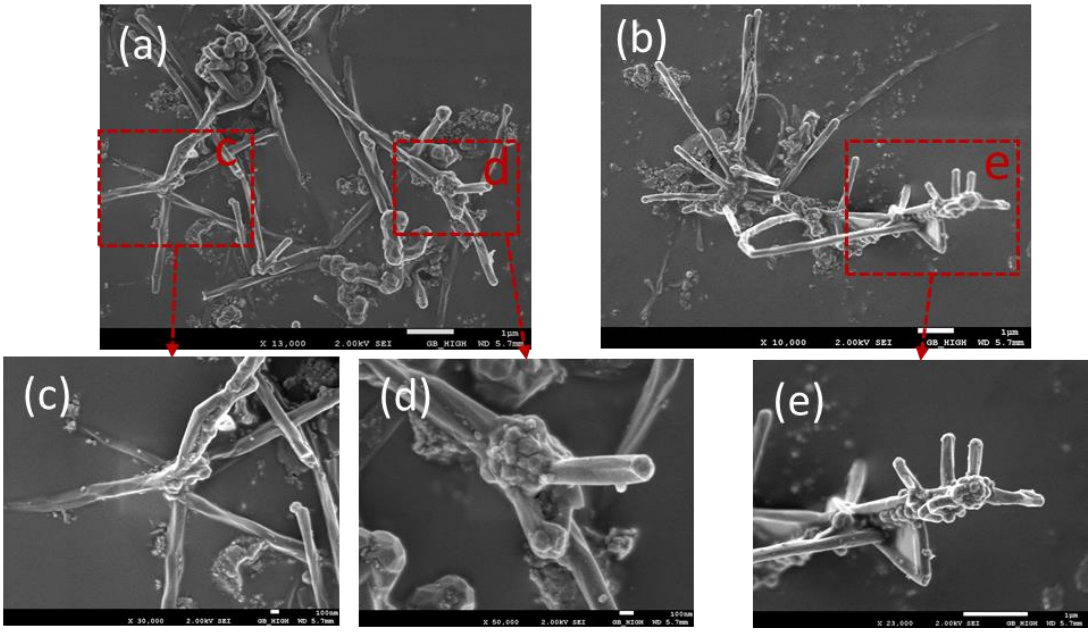

Figure 5.2 Morphologies of ball milled CNTs.

5.1.1.2 GO-HA composite powders

Compared with rGO, GO is an oxidized graphene derivative that contains epoxide and hydroxyl groups within graphene sheets and carboxyl and carbonyl groups at the sheet edges. As a result, GO has high dispersibility and processibility in an aqueous environment [143]. Shown in Figure 5.3, the FESEM images of mixed GO-HA composite powders showed GOs were well dispersed in HA matrixes. Furthermore, the lateral sizes of GO remained smaller than rGO after the mixing and drying process.

Compared with rGO, the GO used in this study has two-sided effects as reinforcements in HA bioceramic composites: (a) GO is easier to be dispersed in water for better mixing;

(b) weaker intrinsic mechanical properties compared with graphene because of the functional groups in GO [144] and smaller lateral size.

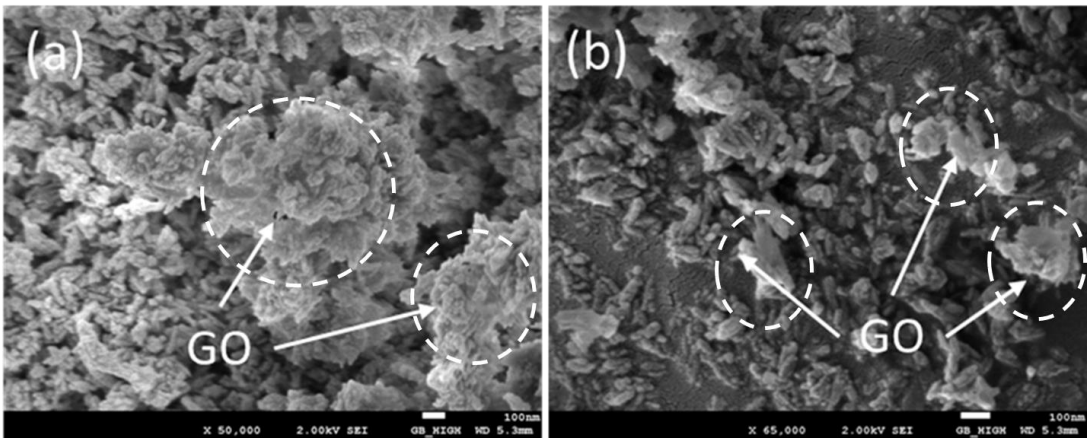

Figure 5.3 Morphologies of mixed GO and HA composite powders at different magnifications.

Therefore, it is interesting to further investigate the properties of densified rGO-HA, CNT-HA and GO-HA composites and the relationships between these microstructures and final properties.

5.1.2 Characterization of densified rGO-HA, CNT-HA, and GO-HA composites

The measured and theoretical densities, and the densification rates of SPSed composites are shown in Figure 5.4. Under the same processing conditions and the same content of nanocarbon precursors, the densities of the 3 types of carbon reinforced HA composites were above all 99.0 %. Compared with pure HA samples, the slightly 0.3% higher of density might because of the test deviations.

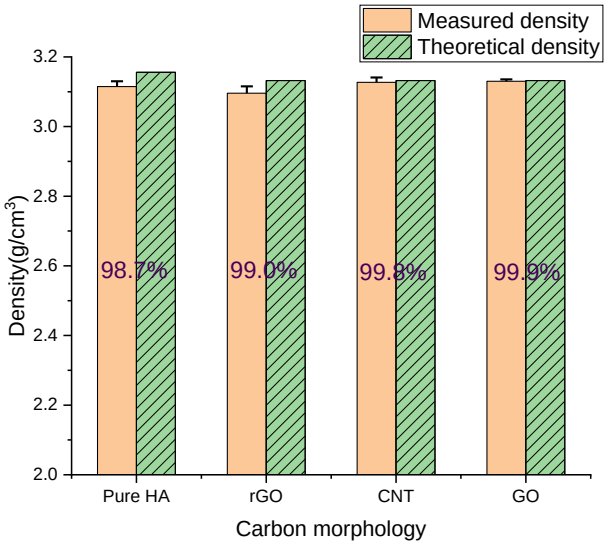

Figure 5.4 Density and mechanical properties of HA and HA reinforced with rGO, CNT, and GO.

X-ray diffraction patterns of SPSed monolithic HA and HA reinforced with rGO, CNT, and GO composites are shown in Figure 5.5 (a). In all the composites, similar characters were observed in the XRD patterns and the main phase was identified as HA. However, the calculated crystallize sizes differed. Compared with pure HA samples, the addition of CNT and GO did not significantly influence the crystallize sizes of HA. In contrary to rGO that could reduce the crystallize sizes by wrapping HA crystallizes in the SPS process [63, 145], the addition of CNT and GO did not significantly influence the crystallize sizes of HA. The reasons might because of the big outer diameter of CNT and the small lateral dimension of GO.

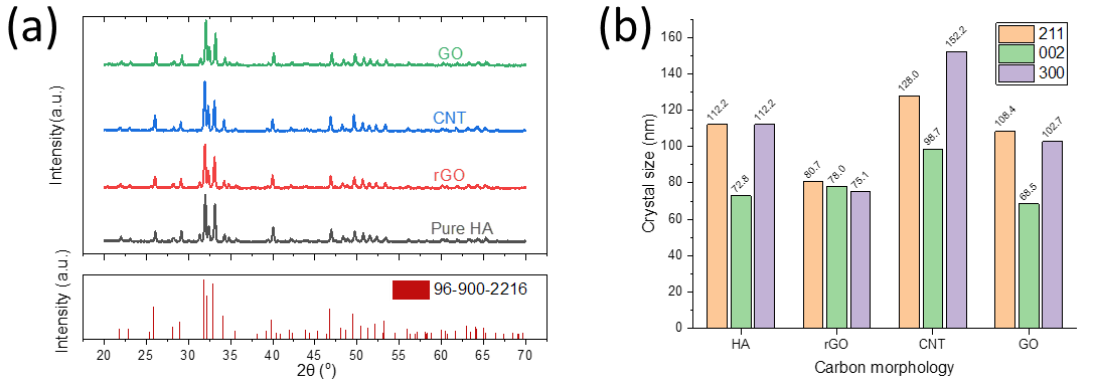

Figure 5.5 XRD patterns (a) and calculated crystallize sizes (b) from various planes of SPSed HA and HA-based composites reinforced with different types of nanocarbons.

Figure 5.6 shows the Raman spectra obtained from SPSed HA and HA reinforced with different types of nanocarbons and the corresponding characteristic peaks data is listed in Table 5-2. The characteristic D, G and 2D bands were observed in each composite and nanocarbons were retained after mixing and SPS processes. In all the three types of nanocarbon reinforced composites, the shifting of G bands to higher values after powder mixing and SPS processes were observed.

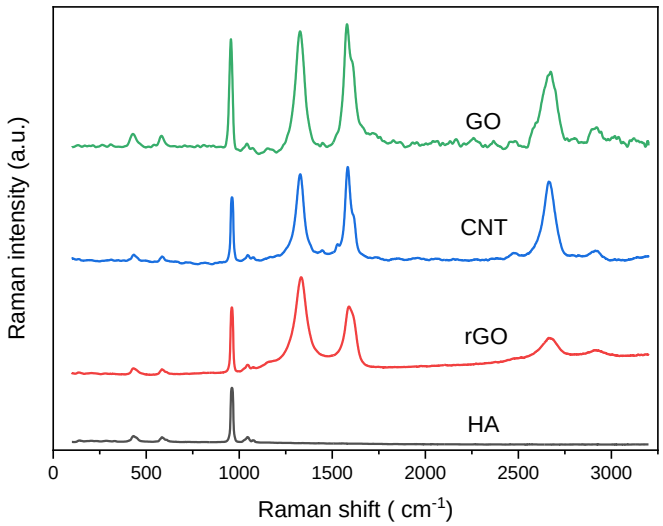

Figure 5.6 Raman analysis of SPSed HA and HA-based composites reinforced with different types of nanocarbons.

Table 5-1 Characteristic Raman spectra peaks of SPSed HA and HA-based composites reinforced with different types of nanocarbons.

	$v_1PO_4^{3-}$	$v_2PO_4^{3-}$	$v_3PO_4^{3-}$	$v_4PO_4^{3-}$	D	G	2D	I_D/I_G
HA	962	430	1045	590	-	-	-	-
rGO	960	430	1045	589	1331	1587	2658	1.47
CNT	961	432	1046	591	1327	1584	2668	0.96
GO	960	431	1045	588	1327	1579	2655	0.97

The mechanical properties of SPSed HA, rGO-HA, CNT-HA, GO-HA composites are shown in Figure 5.7. The hardness of all the three types of carbon reinforced HA was improved and rGO-HA composites had the highest hardness. This was due to the retained highest intrinsic mechanical properties of rGO that were stiffer than CNT and GO. Similar to hardness, Young's modulus and fracture toughness of nanocarbon reinforced composites were higher than pure HA. Especially, CNT-HA and GO-HA composites had higher fracture toughness values with 43.1% and 44.6% improvements than that of pure HA pellets. In terms of CNT, this improvement was mainly due to the unique mechanical locking structures as discussed in Section 5.1.1. The CNTs could arrest and bridge cracks in the HA matrix to suppress crack propagation at the nanoscale [146]. In terms of GO, this improvement was mainly due to the better mixing of GO in HA matrixes.

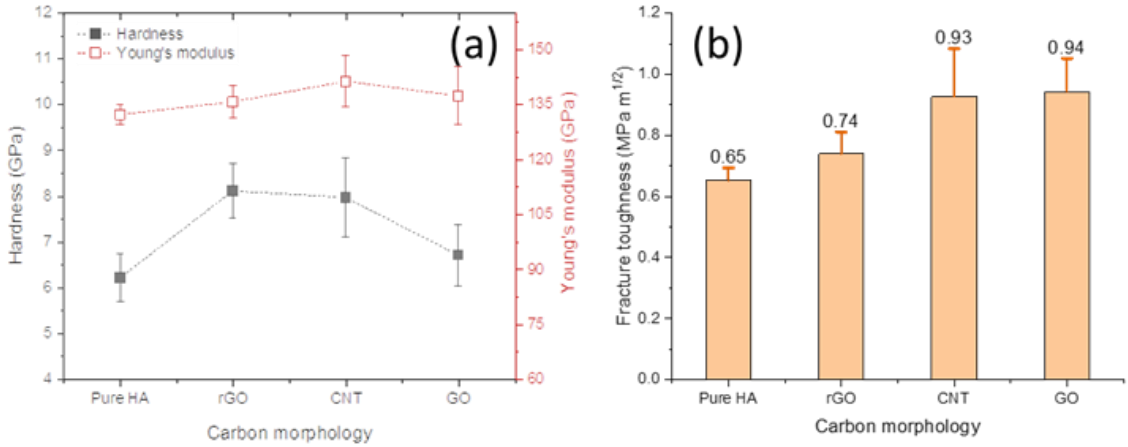

Figure 5.7 Hardness, Young's modulus (a) and fracture toughness (b) of HA and HA reinforced with rGO, CNT, and GO.

However, clusters of CNT entanglements were found in SPSed CNT-HA composites, shown in Figure 5.8 (b-c), that distinguished from well dispersed CNT, shown in Figure 5.8 (a). It is well known that the dispersion of CNT has an essential impact on the properties of CNT reinforced composites [147, 148]. The CNTs that were not disentangled in the fabrication process formed the clusters with air voids in the microstructure. The formation of these defected areas made the composite more compressible, also, the reinforcing effects were not fully utilized.

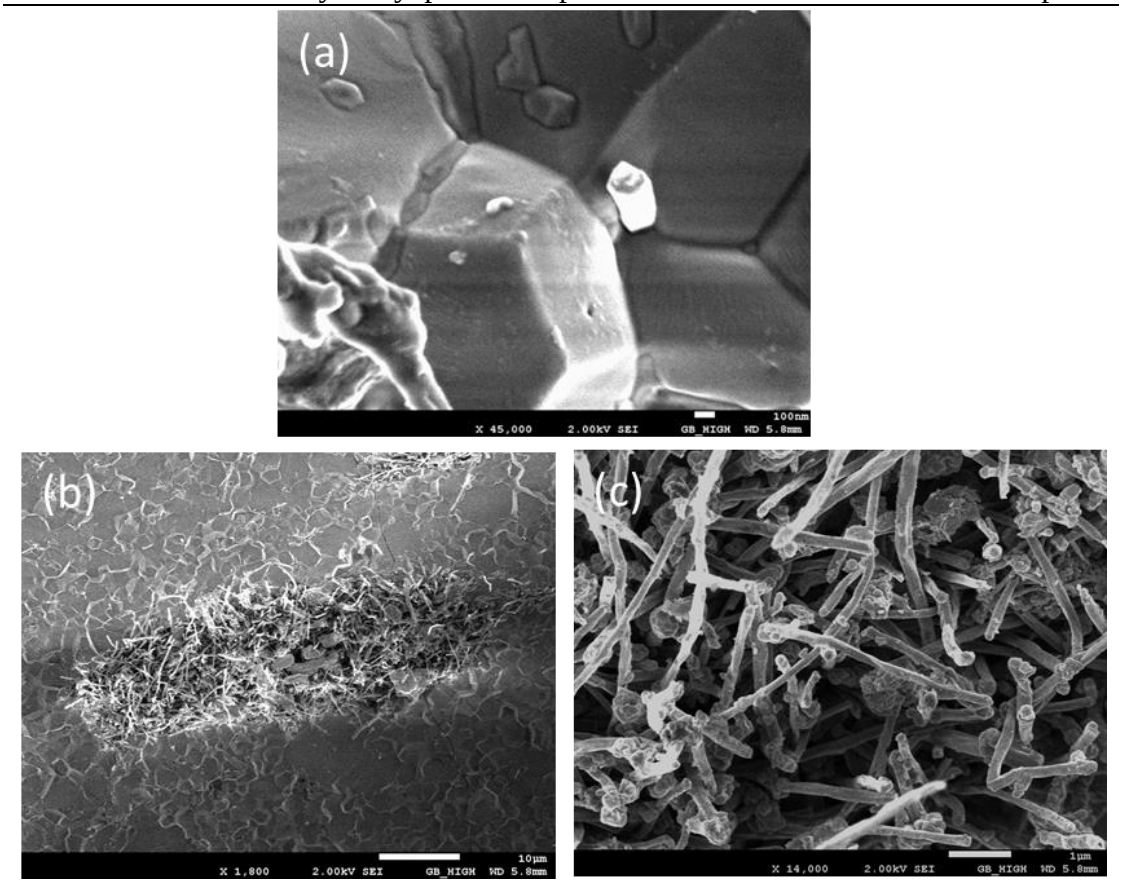

Figure 5.8 Microstructures of well dispersed (a) and agglomerated CNT clusters (b-c).

5.2 Hybrids of reduced graphene oxide and carbon nanotube reinforced hydroxyapatite bioceramics

In recent years, attempts have been made to the hybridization or heterostructuring of graphene and carbon nanotube and opened new sights for research and application of nanocarbons based composites. In various polymer based composites, such as PVA [149], epoxy [150, 151] and PVDF [152], the incorporation of combined graphene and carbon nanotube showed better reinforcing effects than the ones reinforced with one type of graphene or carbon nanotube. However, such a beneficial approach in combining graphene and carbon nanotube in composites are in their early stages.

Especially, in CMCs, few investigations have been made into the use of graphene and carbon nanotube hybrids as fillers into CMCs.

In this section, the hybrid of rGO and CNT were used as reinforcements in HA bioceramic with the ratio between rGO and CNT contents fixed to be 1:1. The samples were processed under same processing routes and two concentrations of nanocarbons were studied: (a) 0.5 wt% rGO and 0.5 wt% CNT, termed as 0.5 rGO + 0.5 CNT; (b) 1 wt% rGO and 1 wt% CNT, termed as 1 rGO + 1 CNT.

5.2.1 Mixing of rGO, CNT and HA powders

The FESEM and TEM images of mixed rGO and CNT reinforced HA composites are presented in Figure 5.9. Under low magnification FESEM image shown in Figure 5.9 (a), separated and connected rGO and CNT were observed, and their distribution was higher than those dispersed separately. Under higher magnifications showing the larger flakes of rGO, presented in Figure 5.9 (b-d), it can be observed CNTs were aligned to rGO flakes in the lateral planes and edges, with HA nanoparticles attached to rGO. The TEM observations of mixed powder showed rGO and CNT were overlapped and HA nanopowders filled the gaps between them. Thus, interconnected networks composed of rGO and CNT with better dispersion of nanocarbons were created.

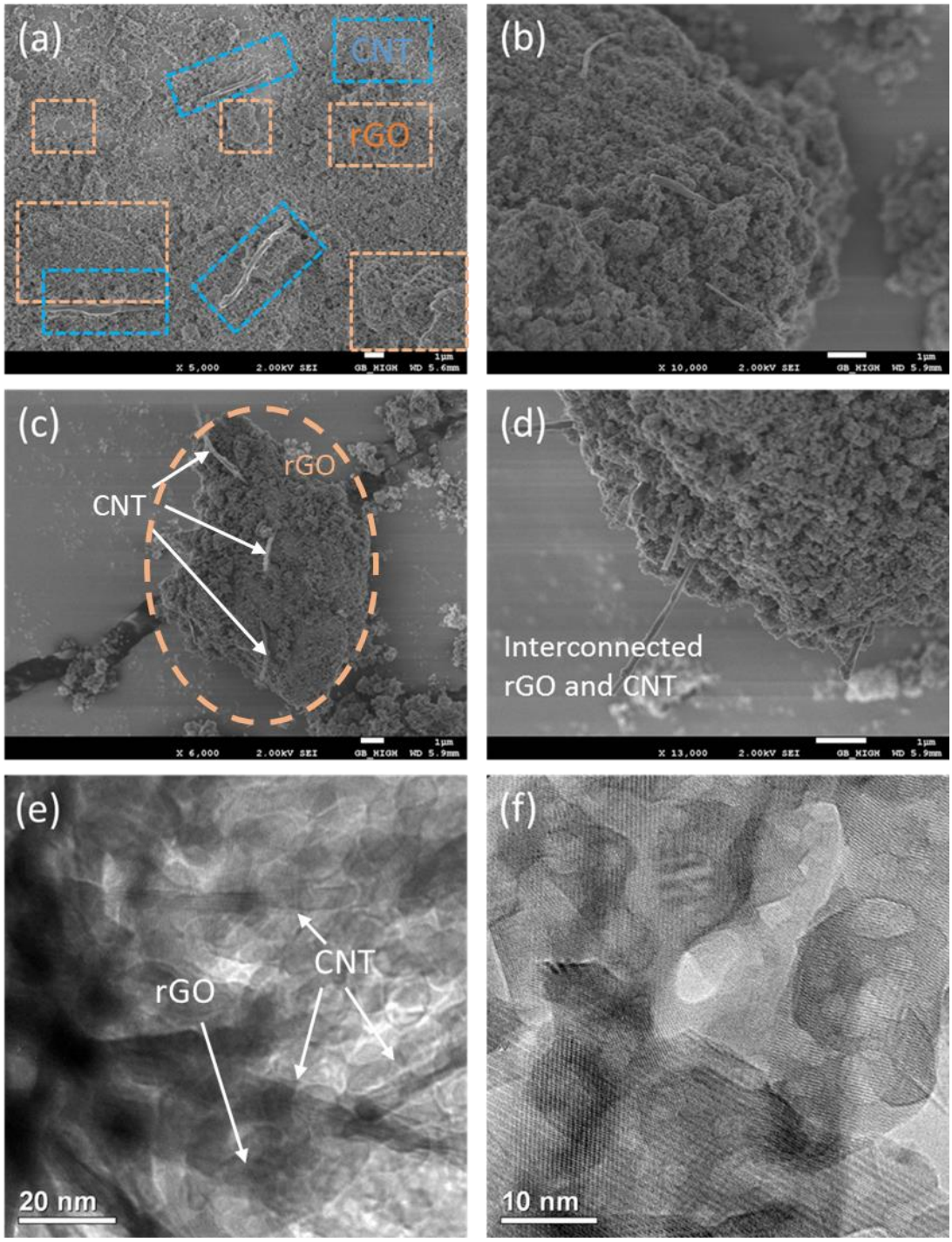

Figure 5.9 Morphologies of rGO and CNT hybrids reinforced HA composite powders: (a) Low magnification FESEM images with orange and blue boxes representing rGO and CNT, respectively; (b-d) Higher magnification FESEM images showing interconnected rGO and CNT; (e-f) TEM images under different magnifications.

5.2.2 Characterization of SPSed rGO/CNT – HA composites

Similar to rGO-HA composites, the densification rates of SPSed rGO/CNT - HA composites were decreased with increasing the content of nanocarbon fillers, shown in Figure 4.6 and Figure 5.10. Under the total nanocarbon content of 2 wt%, the densification rate in rGO + CNT based composites was similar to that of rGO reinforced composites.

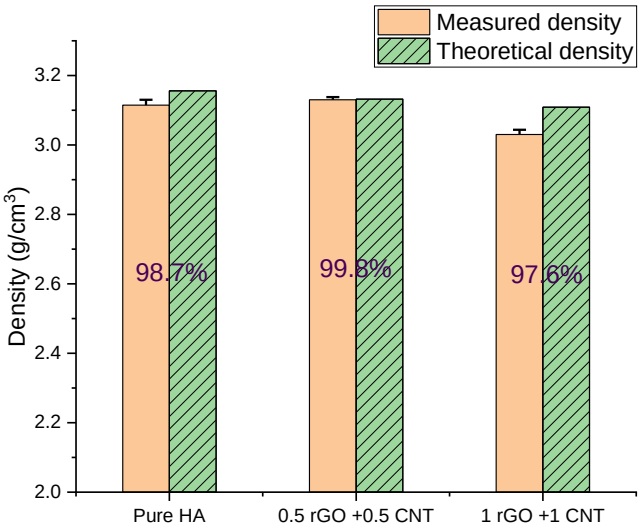

Figure 5.10 The theoretical and measured densities, and densification rates of HA reinforced with different contents of rGO and CNT hybrid.

The XRD analysis shown in Figure 5.11 confirmed that the major phase was HA in all the SPSed composites, despite a small α-TCP peak observed in pure HA pellet that indicated partial decomposition of HA into α-TCP. The crystallize size results are shown in Figure 5.11 (b) showing the addition of rGO and CNT hybrid affected the crystallize growth behaviors of HA. In 0.5 + 0.5 composites, the crystallite sizes were increased in all the planes, while the crystallize growth in (002) and (300) planes were significantly decreased. Under the low concentration of nanofillers, the increased crystallize growth was probably due to the dissimilarity in structural integrity by

nanocarbon addition. With increasing the concentration of nanocarbons to 2 wt%, the proportion of HA nanoparticles wrapped by rGO flakes was increased and crystallize growth was reduced.

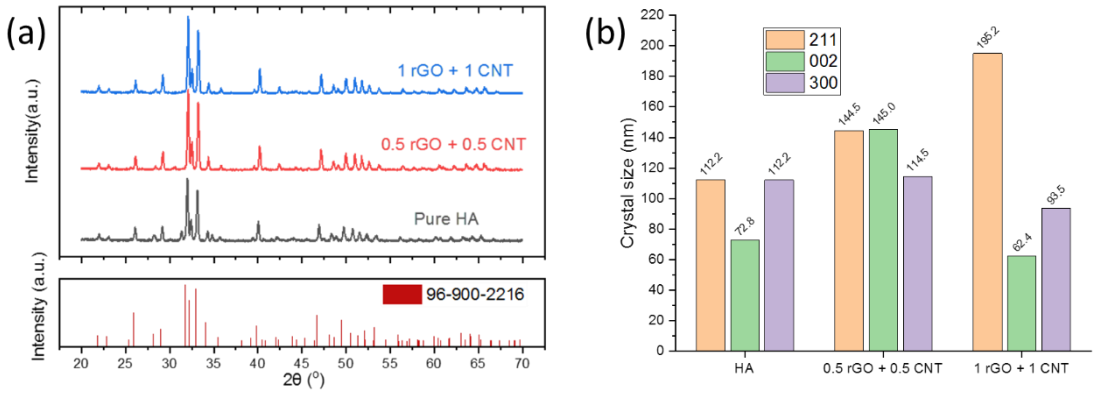

Figure 5.11 XRD patterns (a) and calculated HA crystallize sizes (b) from various planes of sintered rGO and CNT hybrid reinforced HA composites.

Figure 5.12 shows the Raman spectra of SPSed HA, 0.5 rGO + 0.5 CNT, and 1 rGO + 1 CNT composites and the data are listed in Table 5.2. Compared with the composites reinforced with neat rGO or CNT, the blue shift of the G band suggested overlapping of rGO and CNT, thus confirmed the formation of rGO and CNT networks in rGO/CNT reinforced composites [153]. The I_D/I_G ratios of rGO and CNT hybrid reinforced HA composites were between those of pristine rGO and CNT powders, and lower than those of SPSed rGO or CNT reinforced HA composites. This indicated that fewer defects were created by hybridizing rGO and CNT as reinforcements than neat rGO or CNT.

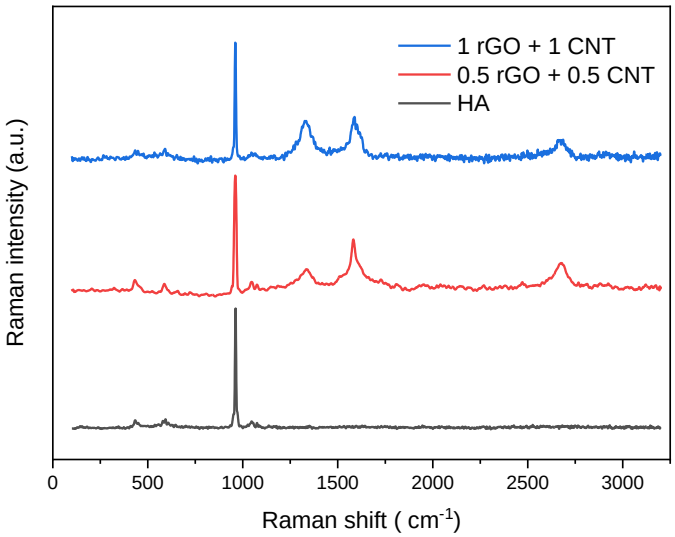

Figure 5.12 Raman spectrum analysis of SPSed HA and HA reinforced with different concentrations of rGO and CNT hybrid.

Table 5-2 Raman data of SPSed HA and HA reinforced with rGO and CNT hybrid.

	$v_1PO_4^{3-}$	$v_2PO_4^{3-}$	$v_3PO_4^{3-}$	$v_4PO_4^{3-}$	D	G	2D	I_D/I_G
HA	962	430	1045	590	-	-	-	-
0.5 rGO + 0.5 CNT	960	435	1045	589	1328	1577	2630	0.596
1 rGO + 1 CNT	960	430	1045	590	1322	1565	2640	1.176

Figure 5.13 shows the mechanical properties of pure HA were increased with rGO and CNT hybrid. Especially, the hardness and fracture toughness were dramatically increased as compared with other samples discussed previously. With increasing the total nanocarbon contents from 1 to 2 wt %, the hardness of rGO and CNT reinforced HA composites was increased by 30.2 % and 42.4 %, while the fracture toughness of these pellets was increased by 41.5 % and 78.9 %, respectively.

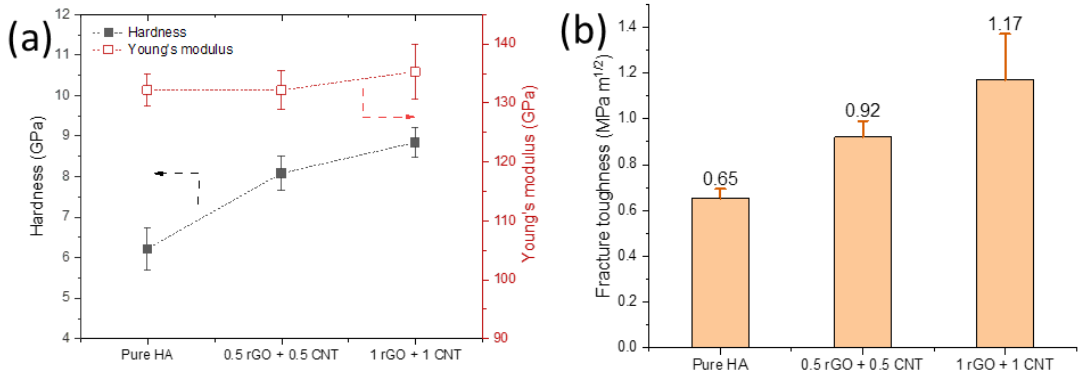

Figure 5.13 Mechanical properties of HA and HA reinforced with rGO and CNT hybrid: (a) hardness and Young's modulus; (b) fracture toughness.

The fracture surfaces of rGO and CNT hybrid reinforced HA composites showed a layered structure of the fractured composites. This layered structure was formed with rGO addition, and CNT bridged the adjacent layers. As pointed out in Figure 5.14 (a), CNT bridging and pullout mechanisms were observed. As shown in the circled area in Figure 5.14 (b), the small-sized CNT was inserted into the rGO flakes, indicating the formation of rGO and CNT networks and their strong interaction.

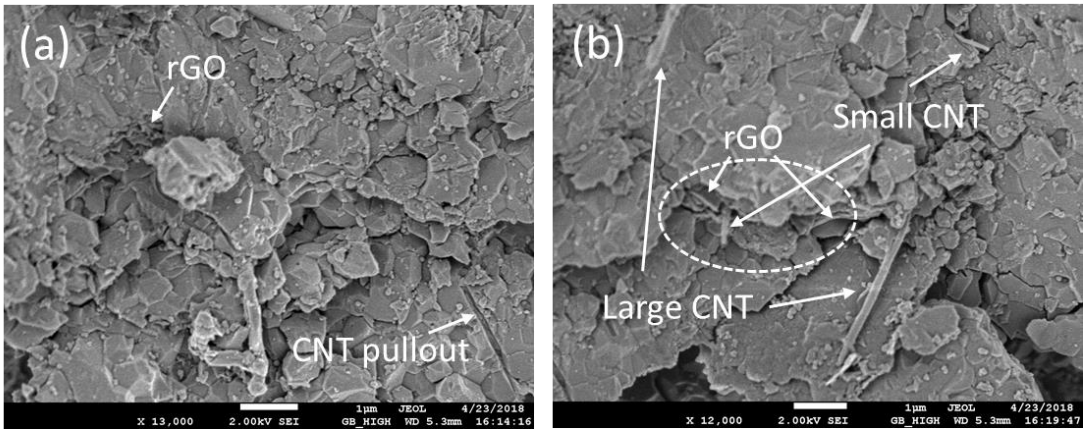

Figure 5.14 Fracture surfaces of HA reinforced with rGO and CNT hybrid composites.

TEM observations were carried out to observe the microstructure of SPSed rGO and CNT reinforced HA composites, shown in Figure 5.15. The TEM results indicated the composite exhibited strong bonding between nanocarbons and HA matrixes. The

interlayer space of 0.275 nm was assigned to the (211) plane of HA [154]. There was no additional phase detected in the bounding area and the bonding between nanocarbon and HA was mechanical bonding. From Bi et al. [155], the mechanical bonding between the nanocarbon and matrix has the following advantageous effects: first, the pull out of nanocarbons from the matrix dissipated the energy for crack propagation; second, the bridging of the matrix by nanocarbon strengthened the matrix; last, the loads transferring from the matrix to nanocarbons were promoted.

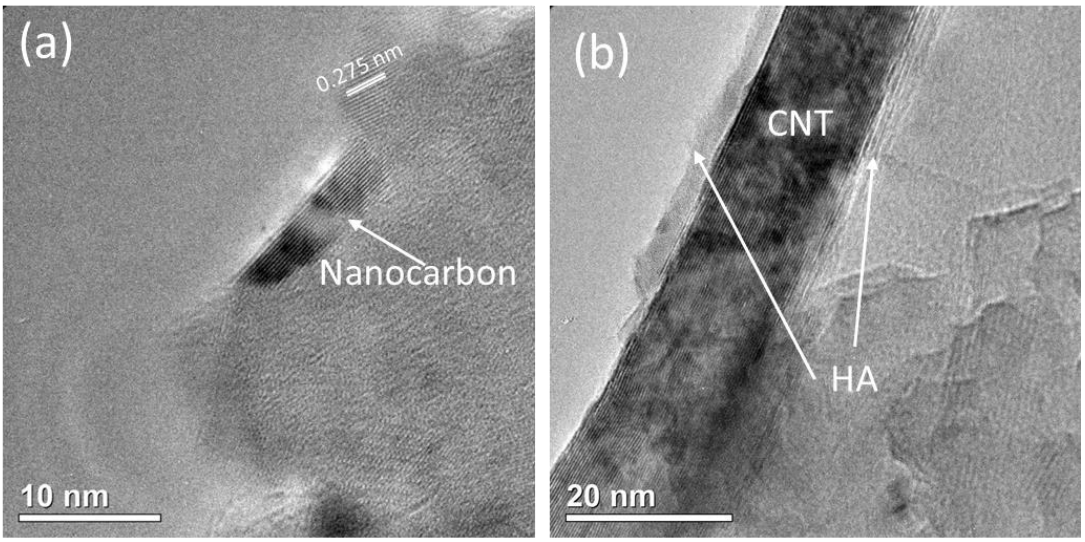

Figure 5.15 TEM images of HA reinforced with rGO and CNT hybrid composites.

5.3 Summary

In this chapter, the effect of nanocarbon morphology on its reinforcing effects in HA bioceramics was investigated by two studies: (a) using one type of nanocarbon with different morphologies as reinforcement, namely rGO, CNT and GO; (b) using rGO and CNT hybrids as reinforcements.

1. In terms of using 1 type of nanocarbon as reinforcement, the size and shape of nanocarbons significantly influenced the structural and mechanical behaviors of

the reinforced composites. The highest hardness and fracture toughness were in SPSed rGO-HA and the CNT-HA composites, with 30.6 % and 43.1 % improvements than those of pure HA samples, respectively. In rGO-HA composites, the rGO plates with large lateral dimensions could wrap HA grains for finer and layered microstructures of the composites for higher hardness. In CNT-HA composites, the interactions between CNTs and HA matrixes were enhanced by the unique mechanical locking structures in CNTs.

2. In terms of using rGO and CNT hybrid as reinforcements, the optimum dispersion of rGOs and CNTs, and strong interface bonding between the nanocarbons and HA matrixes were established in the composites. Furthermore, the small-sized CNTs were found inserted to rGO plates in the mixed powder and sintered pellets. As a result, the HA-based composites reinforced with rGO and CNT hybrids showed a significant improvement in mechanical properties with higher hardness and fracture toughness than the ones reinforced with 1 type of nanocarbon.

Therefore, the rGO and CNT were more efficient in strengthening and toughening HA bioceramics, respectively. The hybrid of rGO and CNT took the advantages of these beneficial effects and the mechanical properties of HA bioceramics were further increased.

Chapter 6 Tribological and fatigue behaviors of hydroxyapatite reinforced with reduced graphene oxide and carbon nanotube

6.1 Introduction

Friction, wear and fatigue behaviors are one of the most important properties that determine the long-term performances of bioceramic implants, especially for the substitution of hip joints and knees [156]. Due to the complex and aggressive environment of the human body, the implanted bioceramics are subjected to successive friction and wear because of the relative abrasion between implants and natural human tissues [157]. During the implantation, the reduction of the implant's mechanical properties would lead to failure of implantation [68, 95]. Furthermore, the poor fracture toughness of monolithic bioceramics also gives rise to lower wear resistance, that the wear resistance of ceramics is directly influenced by the fracture toughness [158].

The insufficient wear resistance of monolithic bioceramics can be improved by adding secondary carbonaceous reinforcement, such as carbon fiber [159] and graphite [160]. Due to the size effect of CNT and rGO, they have already shown their potential as reinforcements to improve biomaterials' tribological behaviors in the matrixes of Al_2O_3, HA, and 3YTZP [161-166]. However, reports on the tribological properties of rGO and CNT reinforced HA composites are still limited, especially both at nano- and micro-scale.

In this chapter, the micro-scale (by ball-on-disk tests) and nano-scale (by nanoscratching tests) tribological behaviors of HA reinforced with rGO and rGO/CNT hybrids were studied to understand the effects of nanocarbon morphology, nanocarbon

content, normal force, wear velocity and geometry of conterbody on the composites' tribological behaviors.

6.2 Micro-scale tribological behavior

In this section, the friction and wear performance of HA reinforced with rGO and CNT were studied in micro-scale by a ball-on-disk micro-tribometer (CSM High-Temperature Tribometer, Switzerland). The counter surface was provided by Si_3N_4 balls with a radius of 3 mm. A normal load (F) of 2 N was applied on the ball, which slid against the polished samples in a circular path (2 mm in diameter) for 10,000 laps at a sliding speed of 1.5 cm/s. The sintered pellets were successively polished by using grit #400, #800, #1200, #2400, #4000 sandpapers and 1 µm, 0.25µm diamond pastes to obtain mirrorlike surfaces and cleaned with ethanol.

6.2.1 Wear rate and wear track morphology

Optical microscopy observations of the wear scars of various compositions (Figure 6.1) show the width of wear scars. In general, compared with pure HA, the width of wear tracks was reduced in succession with increasing the total nanocarbon content from 1 to 2 wt%.

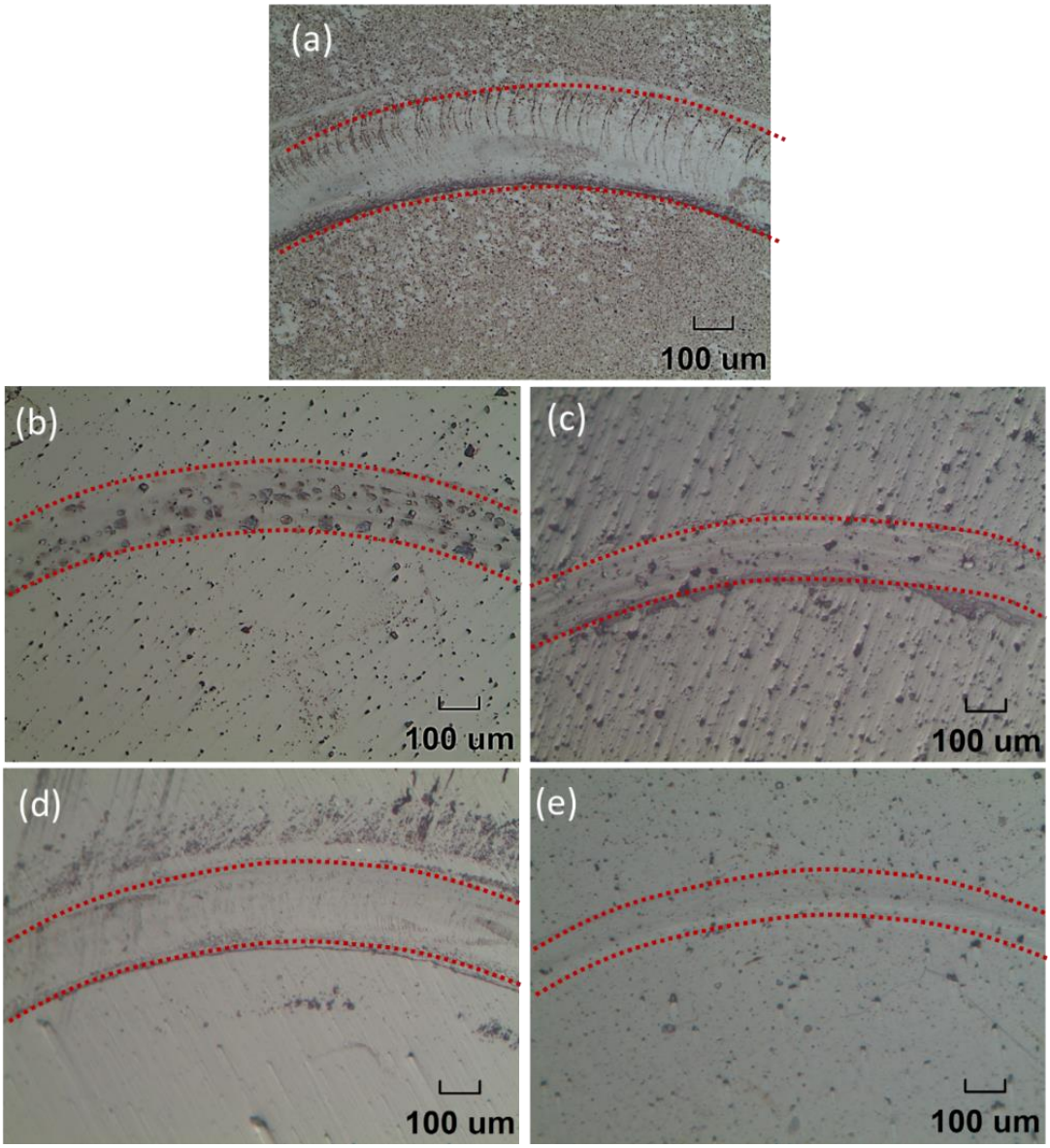

Figure 6.1 Optical microscopy of the wear tracks: (a) HA; (b) 1 rGO; (c) 2 rGO; (d) 0.5 rGO + 0.5 CNT; (e) 1 rGO + 1 CNT.

The wear volume (*V*) was calculated based on the width of wear tracks according to the following equation [167]:

$$V = 2\pi R\left[r^2 sin^{-1}\left(\frac{w}{2r}\right) - \left(\frac{w}{4}\right)\sqrt{4r^2 - W^2}\right] \qquad (6.1)$$

where *R* is the sliding radius, and *w* is the and the average width of the wear track. Term *r* is the radius of the ball equal to 3 mm. The wear rate of the plates (*W*) was calculated from the slope of wear volume versus sliding distance and normal force:

$$W = \frac{V}{L \times F_p} (10^{-15} m^3/m \times N) \quad (6.2)$$

where V is the wear volume loss derived from the equation (6.1), L is the sliding distance equal to 94.25 m and F_p is the applied normal load equal to 2 N.

The specific wear rates calculated from the above equations are shown in Figure 6.2. The addition of any kind of nanocarbon fillers to the HA matrix resulted in a significant improvement in wear resistance, compared to pure HA pellet (18.55 ± 1.70 10^{-15}m^3/m×N). However, this improvement was influenced by the loading content and morphology of the reinforcements.

In terms of loading content, by increasing the total nanocarbon loading from 1wt% to 2 wt%, the wear resistivities of both rGO and rGO + CNT reinforced composites were substantially increased. In rGO reinforced HA composites, the wear rate was decreased from 3.14 to 2.27 10^{-15}m^3/m×N; In rGO + CNT composites, this effect was more obvious, from 8.54 to 1.09 10^{-15}m^3/m×N. In terms of nanocarbon morphology, by comparing the rGO and rGO + CNT based composites that at the same nanocarbon content, the wear rates differ. At 1 wt% total nanocarbon loadings, 1 rGO based composites had a lower wear rate than 0.5 rGO +0.5 CNT based composites. At 2 wt% total nanocarbon loadings, 1 rGO + 1 CNT composites had higher wear resistance than 2 rGO composites.

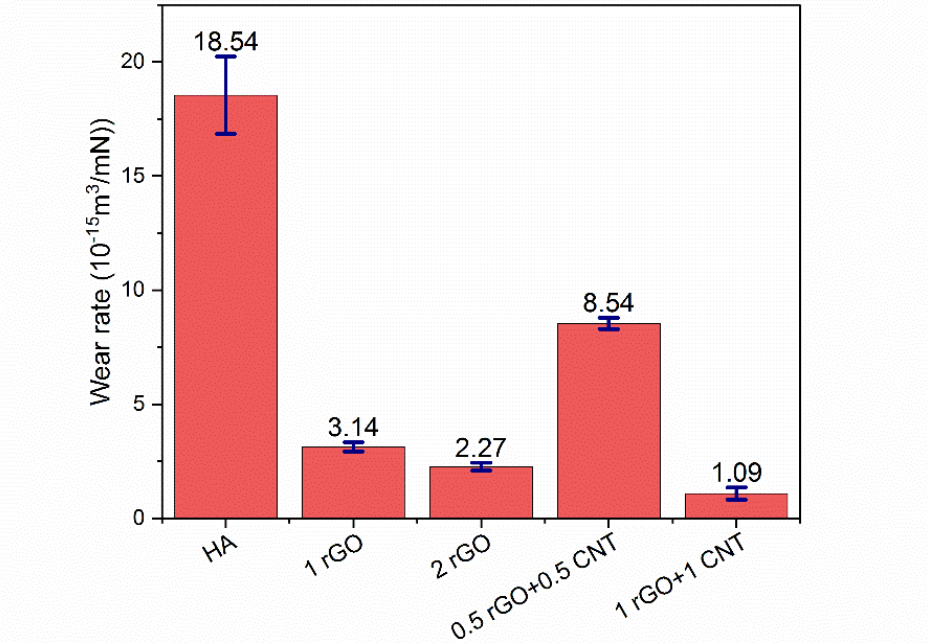

Figure 6.2 Wear rate in terms of composition in macro-scale tribological tests.

6.2.2 Coefficient of friction

To assess the relative friction performance of the composites, the typical behaviors of the friction coefficient (μ) during the ball-on-disk tests of pure HA and carbon reinforced composites were recorded in the whole wear cycle, shown in Figure 6.3. From Figure 6.3 (a), the friction process can be divided into two stages: wear in stage and stable wear stage [168]. It is observed these two stages were most distinct for the pure HA pellet. With low loading of carbons into HA, the low cof. stage of 0.5 rGO + 0.5 CNT pellets lasted for longer laps, compared with pure HA pellets. When the carbon contents were further increased to 2 wt%, the cof.s of both 2 rGO and 1 rGO + 1 CNT pellets were further decreased and maintained at lower values. In addition, it is interesting to see from Figure 6.3 (b) that at first few hundreds of laps, there was a significant drop of cof. when nanocarbons were introduced. Especially, this phenomenon is most obvious in the 2 wt% nanocarbon loaded composites, ie. 2 rGO and 1 rGO+ 1 CNT composites. This decrease in the friction response can be explained

by the lubrication nature of carbonaceous fillers and was enlarged with higher contents of nanocarbons [169].

From Reye's hypothesis, or energy dissipative hypothesis [170]. In the current experimental setup, with the sliding distance and normal force fixed, the work done was proportional to the integration of the friction coefficient during the whole wear cycle. Hence nanocarbon's addition on the reduction of friction coefficient effect contributes to improved wear behaviors.

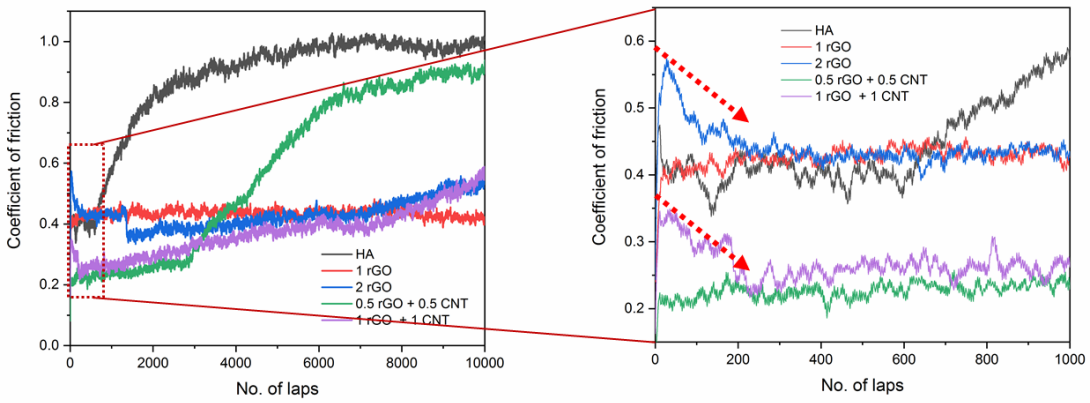

Figure 6.3 Number of laps vs. coefficient of friction in the microtribo test.

6.2.3 Mechanical properties of the worn surface

To study the change in mechanical properties, nanoindentations were done at the center of wear scars of each composition. In nanoindentation tests, the total work (W_t) done by the penetration process can be divided into these two parts, shown in Figure 6.4:

$$W_t = W_u + W_p \tag{6.3}$$

where W_u and W_p correspond to the elastic and plastic work done, respectively. The ratio of W_p over W_t is used to indicate the materials' elastic-plastic properties [162, 171]:

$$\frac{Wp}{Wt} = 1 - \left[\frac{1-3\left(\frac{h_f}{hm}\right)^2+2\left(\frac{h_f}{hm}\right)^3}{1-\left(\frac{h_f}{h_m}\right)^2}\right] \tag{6.4}$$

where h_m and h_f are the depth of the indent at peak load and the final one after elastic recovery, respectively.

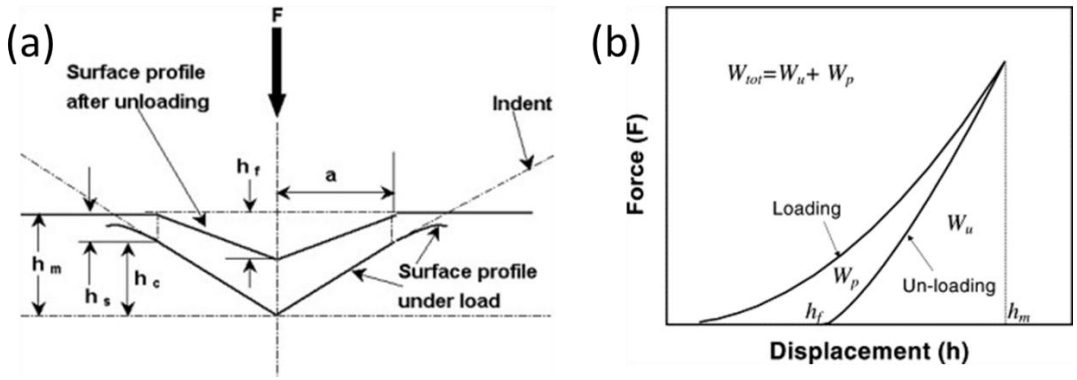

Figure 6.4 Schematic illustration of indentation process: (a) Deformations at peak load position and elastic recovered unloaded position [172]; (b) Displacement vs. force in a nanoindentation cycle [173].

In Figure 6.5 (a), the typical displacement into surface vs. load on sample is plotted. By using equations (6.3) and (6.4), the fraction of plastic work over total work in the nanoindentation process was computed, shown in Figure 6.5 (b). The fraction of plastic work became less after the wear process, so the worn surfaces were more elastic. Also, the composites reinforced with nanocarbons are more elastic than pure HA. In the wear process, if the portion of elastic behavior is increased, the boundary between stick and slip zones moves less, and wear is reduced [174, 175]. Furthermore, materials with higher elastic resilience would absorb more energy to reduce crack and recover after wear test [176, 177].

From Archard's Law [178], the surface hardness has long been considered as a major factor to affect the wear properties. From Figure 6.5 (c), the surface hardness of carbon reinforced composites was higher than pure HA prior to and after the wear test. The higher worn surface hardness results in a considerable reduction in the localized plastic deformation at the worn surfaces and the wear resistivity were improved [179, 180].

Nowadays, the hardness over modulus or H/E ratio is a popular parameter to predict the tribological properties. In Figure 6.5 (d), the H/E of the pellets before and after wear tests of various compositions are shown. Prior to wear tests, the samples' H/Es were around 0.062 for nanocarbon reinforced composites and around 0.047 for pure HA samples. Furthermore, on the worn surface, The H/E were all increased and the values in nanocarbon reinforced composites were still higher than that of pure HA. According to Hooke's law, by reducing elasticity modulus, the material is able to sustain higher elastic deformation prior to a failure at a given load [181].

Figure 6.5 suggests that the wear process has a more obvious influence on the surface mechanical properties in nanocarbon reinforced composites than pure HA, in terms of elasticity, hardness, elastic modulus, and their ratio. By comparing the wear rate and mechanical properties, it can be concluded that the higher elasticity, hardness, and hardness over elastic modulus ratio are favorable to enhance the composites' wear resistance.

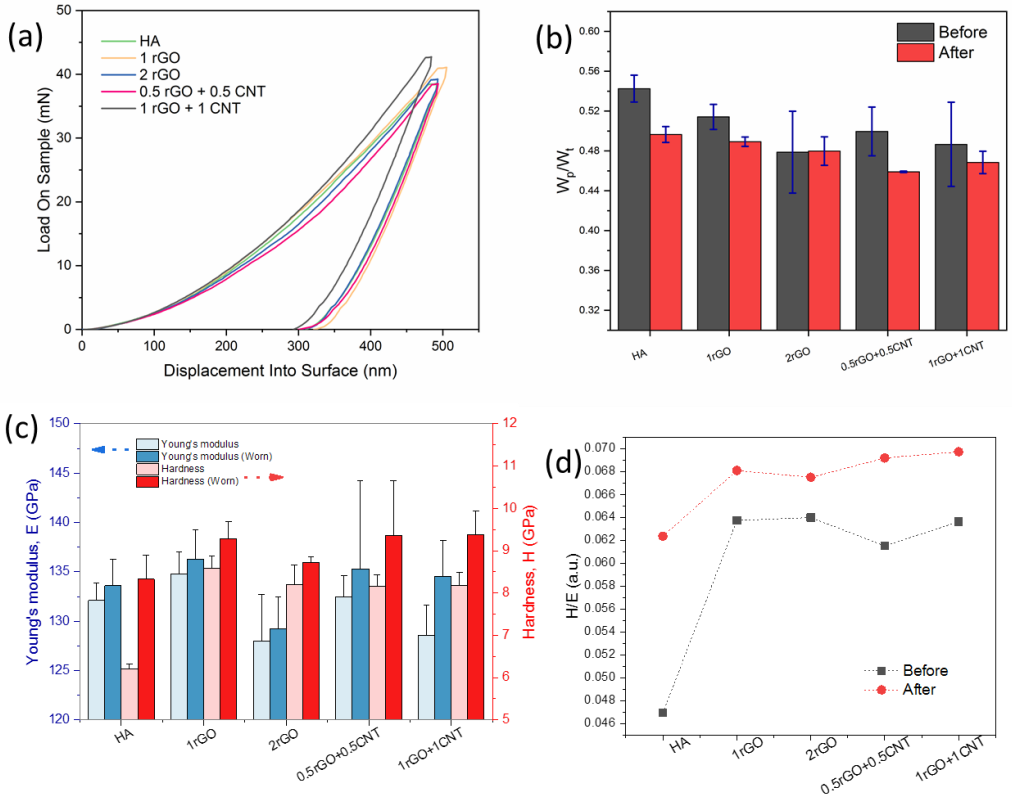

Figure 6.5 The effect of wear process on mechanical properties in various compositions: (a) Typical displacement vs. load curve indented into worn surfaces. (b) Elastic/plastic behaviors of sintered samples and worn surfaces. (c) Young's modulus and hardness of sintered samples and worn surfaces. (d) Hardness over modulus ratio of sintered samples and worn surfaces.

6.2.4 Raman Spectrum

Raman spectroscopy is a fast, nondestructive, and high-resolution tool for the characterization of the nanocarbon based composites [127]. The raman spectra of HA and composites before and after wear tests are illustrated in Figure 6.6. For all the spectra, the characteristic peaks of HA were identified, with the strongest peaks close to 961 cm^{-1} assigned to the v_1 vibration of PO_4^{3-}. In the carbon incorporated composites, there was a downshift of ~2 cm^{-1} for the $v_1PO_4^{3-}$ vibrational mode. By comparing the bands belonging to HA before and after the wear tests in each sample, there was no

significant wave number change. Additionally, no new peak was detected after wear tests, meaning the matrix material HA was chemically stable and there was no reaction between HA and Si_3N_4 counterbody in wear tests.

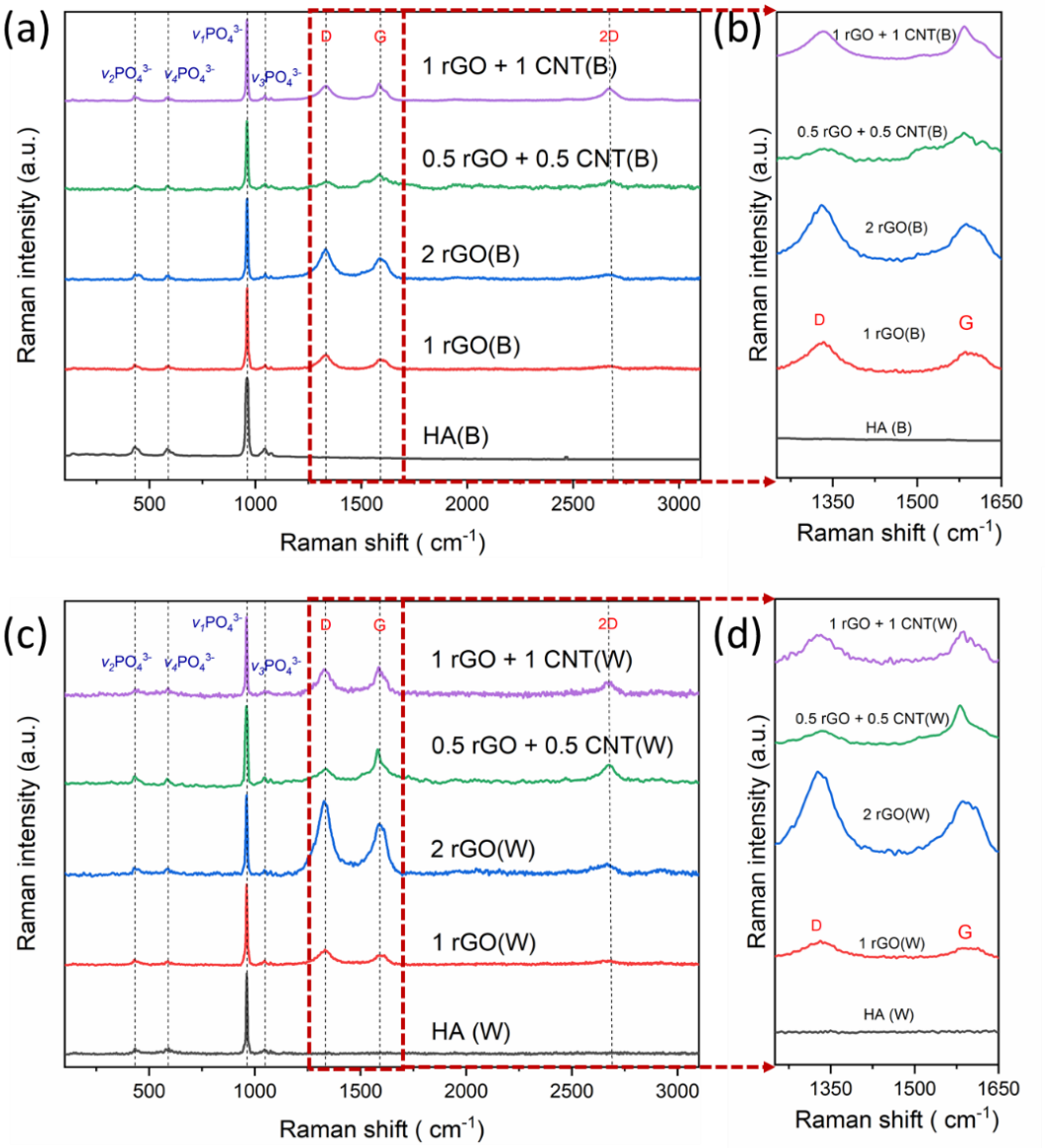

Figure 6.6 Raman spectra with the main bands and enlarged D and G peaks for: (a-b) fresh surfaces before wear test and (c-d) worn surfaces.

Also, the presence of carbon bands in raman spectra of rGO and rGO + CNT reinforced composites shows the survival of nanocarbons after the sintering and wear processes. The calculated intensity ratios of D peak and G peak (I_D/I_G) are shown in Table 6.1 to

indicate the degree of structural defects of rGO and CNT. After the wear tests, the I_D/I_G ratios were increased in each composition. This increasement is directly related to the number of edges and defects, indicating the fragmentation of rGO and CNT. By comparing the increasement of I_D/I_G ratios due to wear process in rGO composites and rGO + CNT composites, the increasement was less in rGO + CNT hybrid composites. The "rebar graphene" structure was formed with CNT addition. Both the higher stability and more lubrication area of the hybrid carbons contributed to the improved friction and wear properties [182, 183].

In raman spectra, the G band shifts to higher wavenumber when the number of graphene layers decreases [127, 128]. After the wear tests, the G bands had positive shifting in all the samples, confirming the thinning of nanocarbons induced by the wear process.

A summary of the identified bands and its assignations for both sintered pellets and worn surface of HA, nanocarbon reinforced composites, Stoichiometric HA and natural bone are tabulated in Table 6.1.

Table 6-1 Comparison of Raman spectroscopic band assignments for the sintered and worn samples, stoichiometric HA and Bone.

		$v_1PO_4^{3-}$	$v_2PO_4^{3-}$	$v_3PO_4^{3-}$	$v_4PO_4^{3-}$	D	G	2D	I_D/I_G
Before	HA	962	430	1045	590	-	-	-	-
	HA 1 rGO	961	431	1047	590	1335	1586	2666	1.47
	HA 2 rGO	961	433	1047	588	1329	1588	2670	1.42
	HA 0.5 rGO + 0.5 CNT	960	435	1045	589	1336	1584	2674	0.59
	HA 1 rGO + 1 CNT	960	430	1045	590	1333	1584	2671	1.18
Worn	HA	962	433	1047	592	-	-	-	
	HA 1 rGO	961	430	1046	588	1332	1591	2660	1.78
	HA 2 rGO	961	428	1046	590	1328	1591	2658	1.85
	HA 0.5 rGO + 0.5 CNT	960	431	1046	586	1334	1585	2679	0.58
	HA 1 rGO + 1 CNT	960	433	1046	590	1326	1588	2666	1.43
Reference	Stoichiometric HA [184]	964	433	1048	591	-	-	-	-
	Bone [116]	961	432	1044	590	-	-	-	-

6.2.5 Wear track microstructure

The morphology of wear tracks also plays a vital role in the properties. The worn surfaces of all samples were compared, as shown in Figure 6.7. The examination of the surface morphology of the wear tracks clearly indicated that HA and nanocarbon reinforced composites had undergone abrasive wear.

In pure HA samples, microcracks were formed in wear track randomly. It is quite straightforward that worn surfaces of reinforced composites were smoother than pure HA samples, besides the presence of some grooves. In nanocarbon reinforced composites, the microcracks observed in HA were rarely visible and only little bigger cracks were observed. The reduction in microcracks can be explained by the self-lubricating ability of rGO and CNT that play a vital role in obtaining smoother surface and the bigger cracks were formed by the existence agglomerating or stacking of nanocarbons.

.

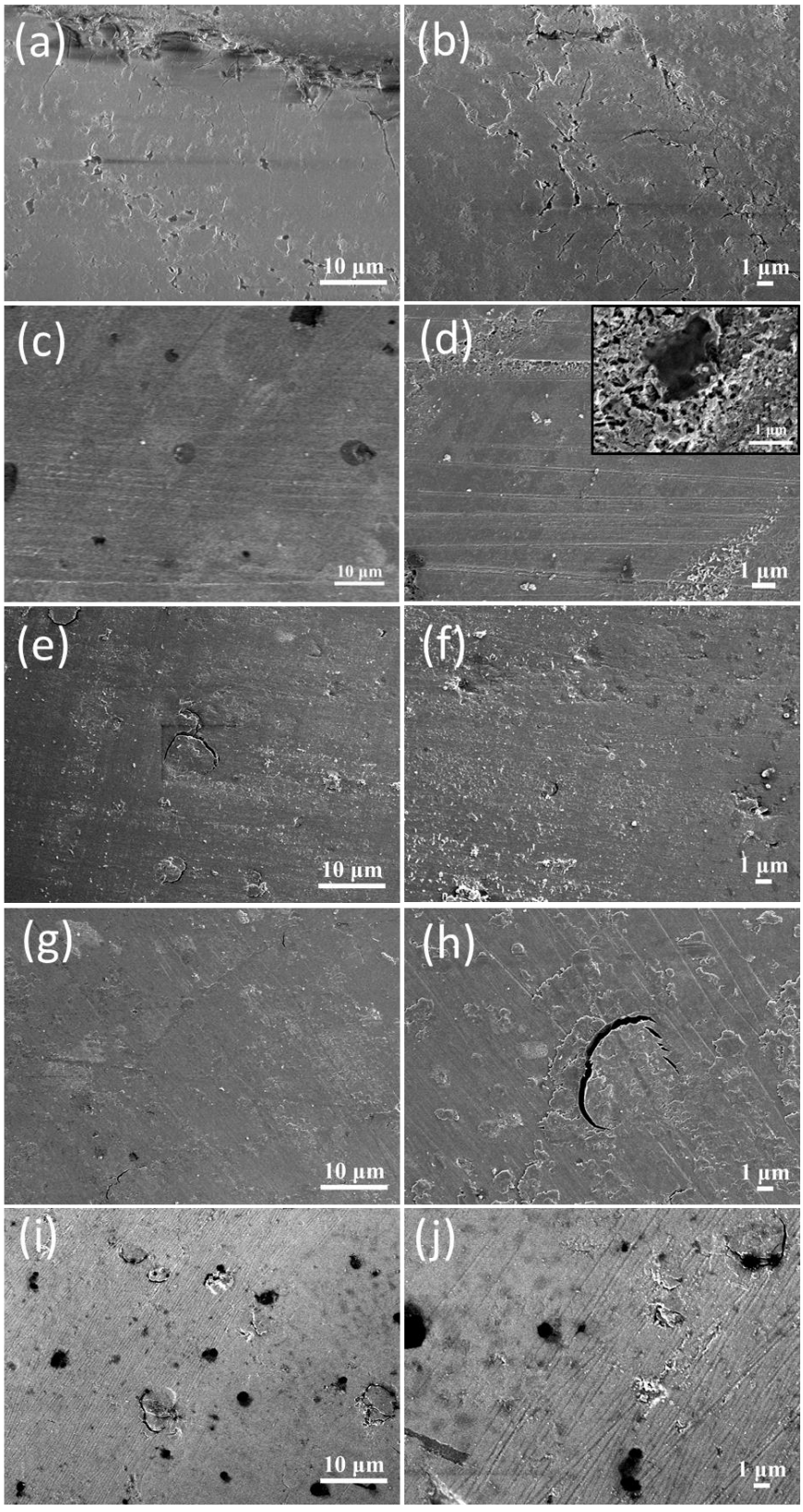

Figure 6.7 Low-mag wear track FESEM images of various compositions at 1000X and 5000X: (a-b) HA; (c-d) 1 rGO, inset: rGO had strong bonding with HA matrix; (e-f) 2 rGO; (g-h) 0.5 rGO + 0.5 CNT ; (i-j) 1 rGO + 1 CNT.

To study the role rGO and CNT played in improving tribological properties, the wear track morphologies of 2 wt% nanocarbon, in forms of rGO and rGO + CNT hybrid, reinforced HA composites were examined by FESEM under LABE mode at higher magnifications, shown in Figure 6.8-9.

Figure 6.8 shows the worn and fresh surfaces of 2 wt% rGO reinforced HA composites. As can be seen in Figure 6.8 (a), there was a clear boundary between the fresh and worn surfaces, marked with a blue dotted line. The fresh surfaces were flat and dense with no crack, while grooves were parallelly aligned in the worn surface. From Figure 6.8 (c) showing the fresh surface at higher magnification, the shaded area indicates the distribution of rGO in HA. From Figure 6.8 (b,d) showing the worn surface, fragments of rGO were attached firmly in the grooves. This confirms the strong bonding between rGO and HA could survive in the harsh wear process.

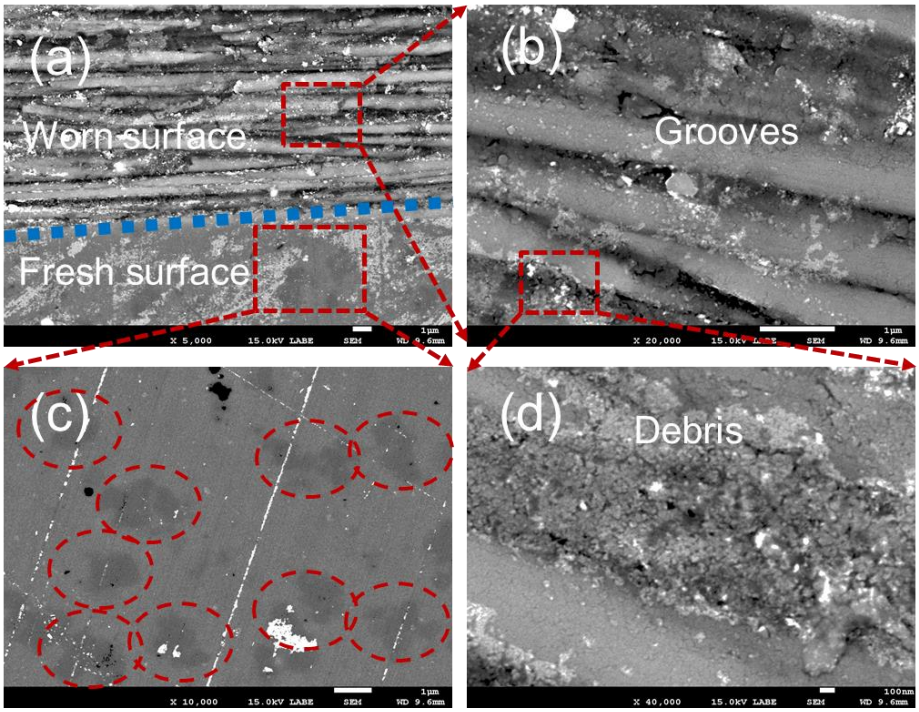

Figure 6.8 FESEM LABE images of 2 rGO reinforced HA composites showing the fresh and worn surfaces: (a) fresh and worn surfaces at lower magnification; (b-d) worn surfaces at higher magnifications; (c) fresh surface at higher magnification.

Figure 6.9 shows the fresh and worn surfaces of 1 rGO + 1 CNT reinforced HA composites. As shown in Figure 6.9 (c), a boundary between fresh and worn surfaces was marked in the dotted blue line. The fresh surfaces, shown in Figure 6.9 (a-b) were as smooth as that of 2 rGO composite. Similarly, tribofilms were formed and composed of rGO and CNT. During the wear process, rGOs were fragmented into smaller and thinner pieces and CNTs were cut off and fell off by the Si_3N_4 counter surface. As a result, rGO and CNT were ground on the test surfaces and a solid lubricant film composes of carbon was formed. Usually, the reinforcements act as load bearing components at contact surfaces which tend to protect the surface from plowing during sliding [185]. The formation of tribofilm was in accordance with the coefficient of friction results that there was a significant drop of cof. in the first hundreds of cycles in the composites with high nanocarbon added. This result explains the reduction in wear rate that the contact between the two sliding surfaces changed from HA-to-Si_3N_4 contact to carbon protected HA-to-Si_3N_4 contact. Moreover, pressure on the tribosurface could be transferred effectively from the matrix to the strong rGOs and CNTs due to the strong interface bonding. As a result, the resistance to plastic deformation was improved and the wear resistance of the composites was further improved.

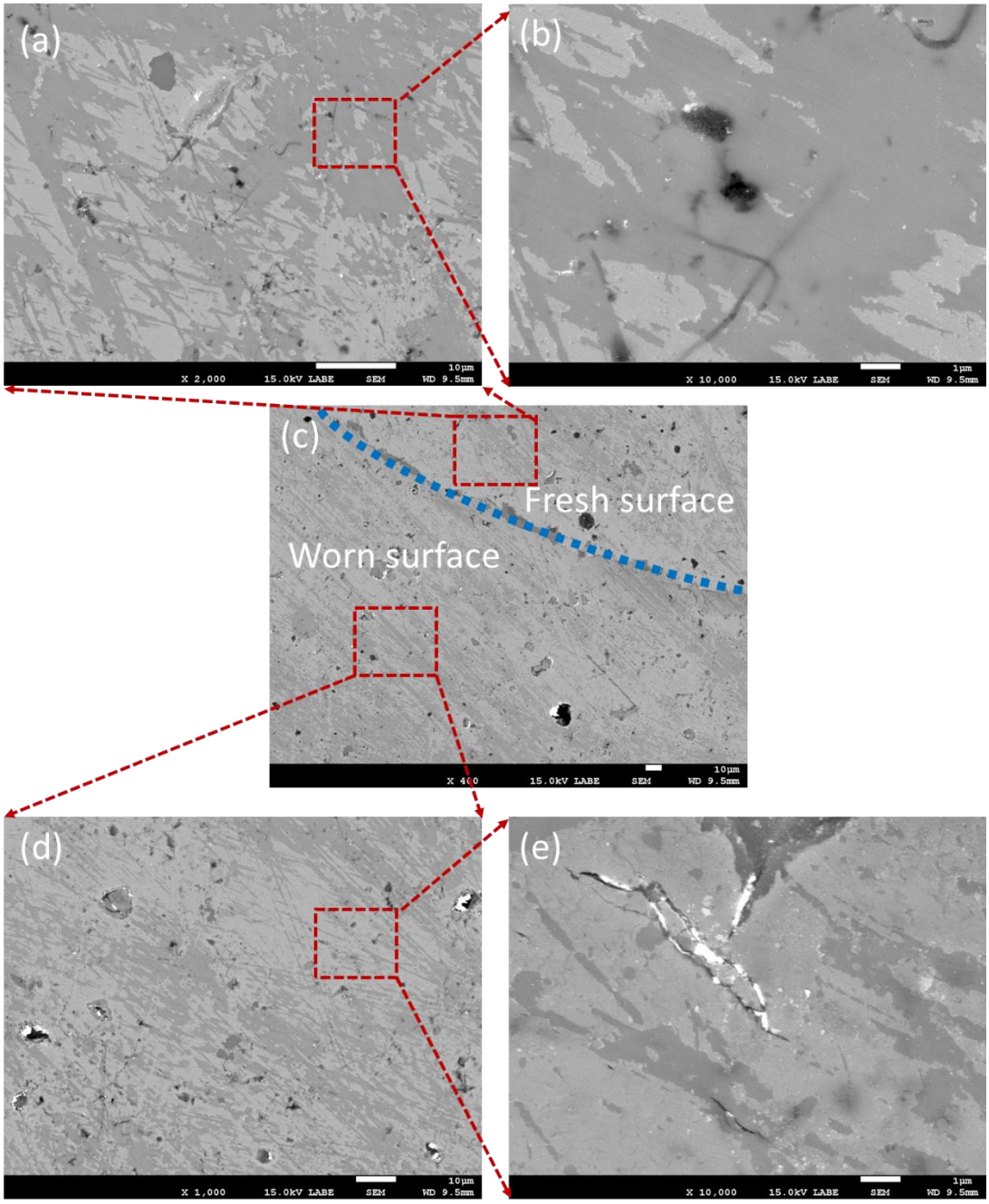

Figure 6.9 FESEM LABE images of 1 CNT + 1 rGO reinforced HA composites showing the fresh and worn surfaces: (a-b) the fresh surfaces at higher magnifications; (c) fresh surface and worn surface at lower magnification; (d-e) the worn surfaces at higher magnifications.

The formation of tribofilm was also confirmed by EDS analysis, shown in Figure 6.10. In Figure 6.10 (a), both the EDS line scan and area atom scans confirm the variation of

carbon atom concentration induced by the wear process. The carbon atom under the line scan showed a significant drop from wear track to the fresh surface. The values given by the area atom scans taken ~15 μm away from the line scan have shown the same trend and the value of carbon weight percentage dropped from ~12.3 to 5.6%. The EDS results indicate that a carbon rick layer was formed uniformly after the wear process in 2 rGO reinforced HA composite. In Figure 6.10 (b), EDS mapping was done on the worn surface of 1 CNT + 1 rGO composite. From the atom mapping and spectral analysis, the detected atoms were belonging to HA (calcium, phosphate, and oxygen) and CNT/rGO (carbon and oxygen), and no silicon or nitrogen atoms were detected. Thus it is further confirmed by EDS that there was no reaction between HA and Si_3N_4 counter ball during the wear process. By comparing the distributions of carbon and oxygen atoms, rGO and CNT were reduced mostly after the wear process. The reduction temperature for rGO is around 150 ~ 250 ^oC in air [186] and high temperature was generated in a ball on disk wear tests that induced by the friction work in the process [187]. During the reduction process, the expansion of CO or CO_2 gases evolved into the spaces between graphene sheets will create huge pressure between the stacked layers [188]. In this way, the stacked rGO platelets are separated and rGO was thinned. The formation of a tribofilm also explains the reduction of cof as discussed previously.

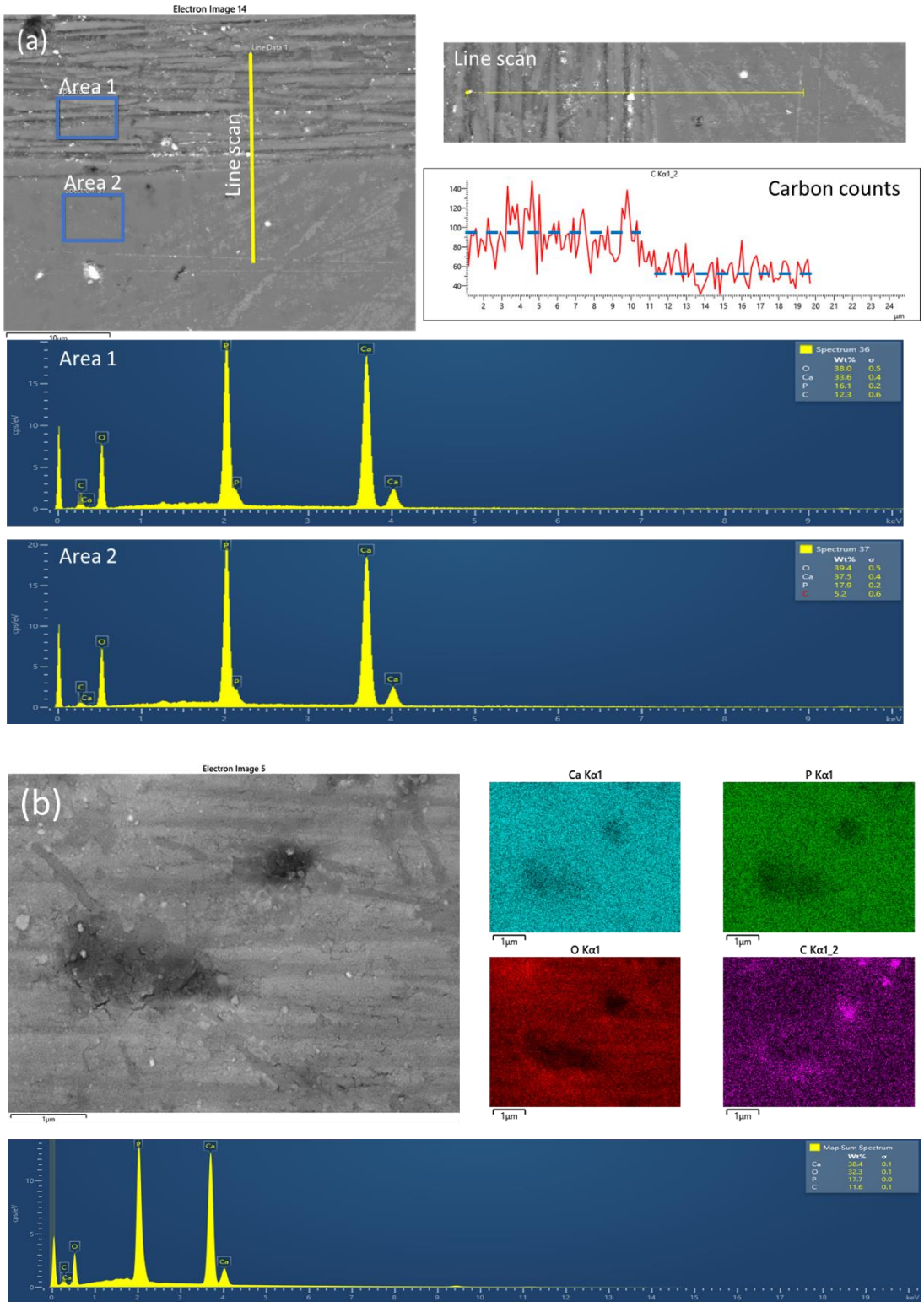

Figure 6.10 EDS analysis of the wear tracks of 2 rGO (a) and 1 rGO + 1 CNT (b) reinforced HA composites.

6.2.6 Mechanism

The incorporation of rGO and CNT + rGO hybrid have both reduced the friction between sintered pellets and Si_3N_4 counter ball, and the sintered pellets' wear resistance was improved. A tribo film was formed during the wear process due to the thinning and pinning effects of rGO and CNT. As a result, friction was lower due to the nature of rGO and CNT and local hardening was introduced with higher hardness and hardness over modulus ratio. In addition, CNT served as the framework in rGO + CNT composites that enhanced the connection between rGO and HA, making the composites more resistant to wear. A schematic illustration of the above wear process of the composites reinforced with rGO and CNT + rGO hybrid is shown in Figure 6.11.

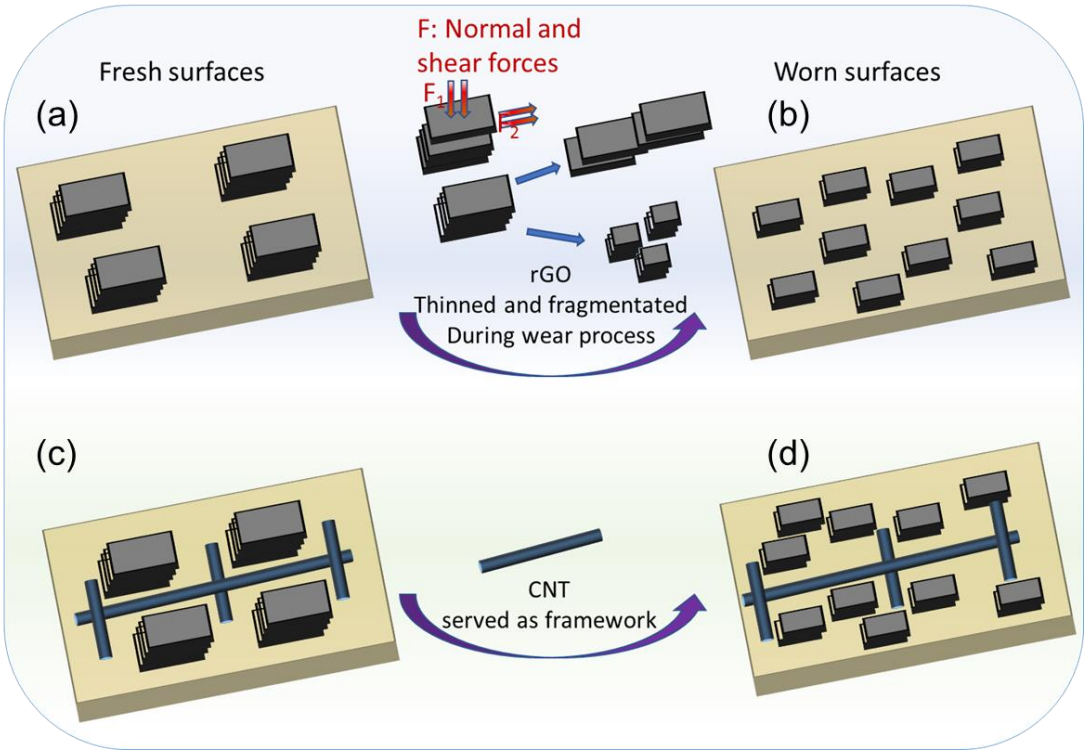

Figure 6.11 Schematic illustration of the surfaces before and after wear tests: (a-b) rGO reinforced HA composites; (c-d) rGO + CNT reinforced HA composites.

6.3 Nano-scale tribological behavior

The nano-scale tribological test, or nanoscratch, is a newly developed technique and has been shown to be an effective low cycle wear and fatigue test [189, 190]. In addition to the nano-scale tribological tests, the constant load, unidirectional multipass scratch tests were conducted.

6.3.1 Experimental setup

The nano-scale tribological behaviors of the sintered pellets were evaluated with single direction multicycle nanoscratch tests using Agilent G200 (Keysight Technologies, US). The schematic illustration of experimental systems is shown in Figure 6.12. In the present study, a Berkovich diamond tip (Micro Star Technologies B-style, tip radius ~20 nm) was used and the tip-area calibration was done using a standard fused silica substrate of known modulus (72 GPa). Similar to nano-scale tribological tests, the sample surface was polished to mirrorlike and cleaned with ethanol. The polished specimens were then mounted on the workbench of the nanoindenter with hot glue and cleaned with ethanol.

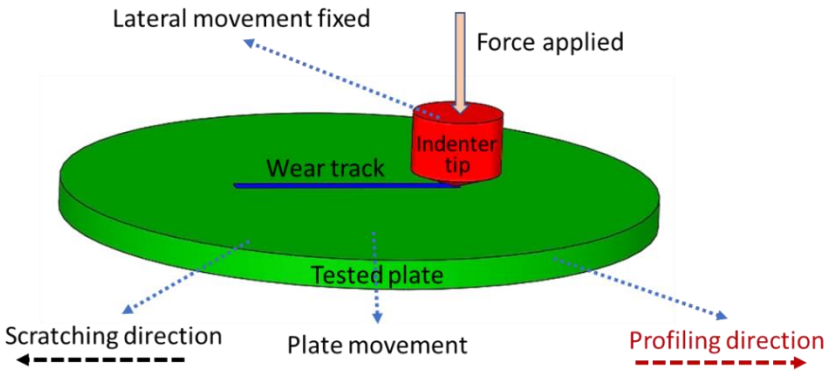

Figure 6.12 Schematic illustration of experimental systems used in nano-tribo tests.

In order to describe the nanoscratching process clearly, the typical recorded time vs. load in the 10 whole cycles and scratch distance vs. scratching load in one cycle is shown in Figure 6.13. In each test, after the indenter tip approaching the test surface, a

pre-profile scan was performed 1.4 times the wear path length to determine the surface roughness before the test with a constant load of ~90 µN. Then the indenter tip was returned to the origin position, the wear segment was conducted at a constant load of 5 mN or 20 mN and velocity of 1 µm/s or 5 µm/s to eliminate the thermal effect [191, 192]. After the wear segment, post-profile was conducted to evaluate the residual wear depth after the elastic recovery of the specimen. These 3 above-mentioned processes of pre-profile, wear segment and post-profile are considered as a complete cycle. In each test, 10 cycles were done.

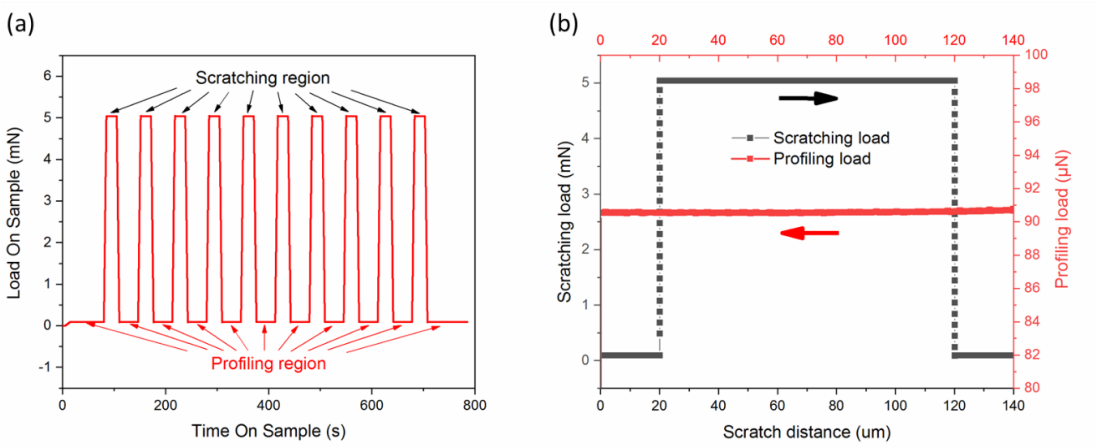

Figure 6.13 Typical recorded load in the test: (a) Time vs. load in the 10 whole cycles; (b) Scratch distance vs. scratching load in a cycle.

6.3.2 Wear track deformation and wear volume loss

Nanoindenter measures both the displacement into the surface, or the depth penetrated by the indenter in wear segment and the residual groove depth after elastic recovery in the post-profile section in each cycle. As shown in Figure 6.14 (a), the depth recorded in the post-profile section is much smaller than the wear segment. Arvind Agarwal et. al. [193] defined these two depths as the contact depth and true depth. The contact depth recorded in the wear segment is the instantaneous depth of penetration of the indenter during scratching. The true depth recorded in the post-profile section was measured

after the elastic recovery process had taken place. Based on the geometry of Berkovich indenter shown in Figure 6.14 (b), both the maximum wear track deformation and accumulated wear volume were calculated. The maximum wear track deformation was calculated associated with the contact depth using formula

$$A = \frac{1}{2}h[h\,tan\,\alpha + h\,tan(\theta - \alpha)] \qquad (6.5)$$

The accumulated wear volume (W_v) was calculated using the average true depth in each cycle to represent the true volume of material removed due to the nanoscratching tests, given by

$$W_v = \int_{-l/2}^{l/2} A(x)dx = \int_{-l/2}^{l/2} \frac{1}{2}h[h\,tan\,\alpha + h\,tan(\theta - \alpha)]dx \qquad (6.6)$$

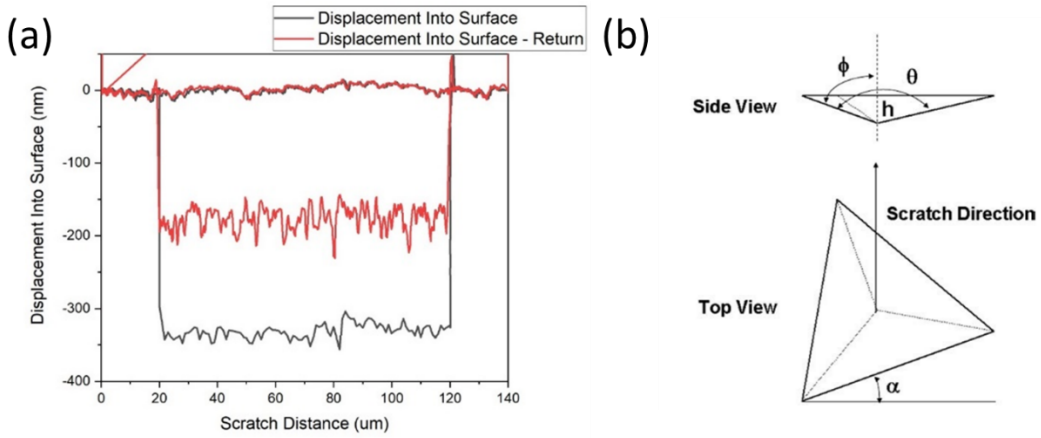

Figure 6.14 (a) Typical recorded depth during the wear segment and post-profile section in the nanoscratch test. (b) Figure showing the top view and side view of Berkovich indenter [193].

The calculated maximum wear track deformation in the wear segment follows quadratic constitutive relations with cycle number, shown in Figure 6.15 and listed in Table 6-2. In all the tests, the slope decreases linearly. The wear track deformation was increased fast in the first few cycles and became more stable in the higher cycle. This can be explained by the reduction in contact pressure between the indenter and test surface

through the wear test [194]. In higher cycle numbers, the indenter scratches on the residual groove produced by the previous cycle. As a result, the contact area was increased, while the normal force was fixed, so the contact pressure was decreased.

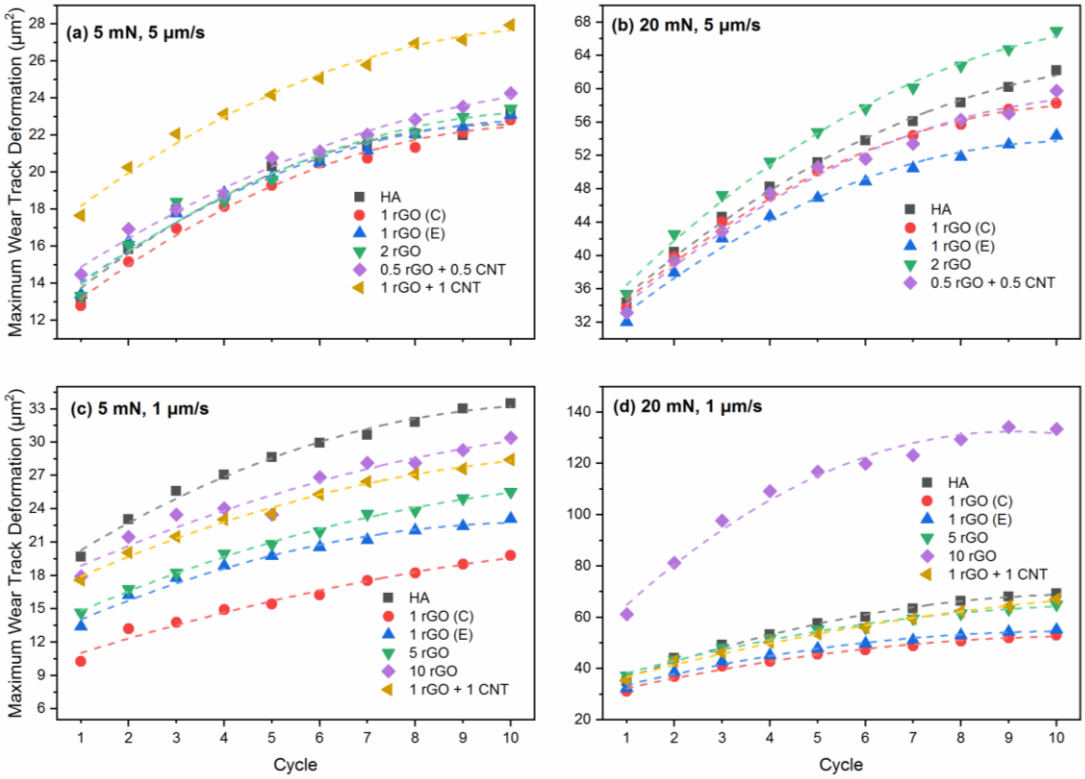

Figure 6.15 Maximum deformations after each cycle under various compositions and test conditions: (a) 5 mN, 5 µm/s; (b) 20 mN, 5 µm/s; (c) 5 mN, 1 µm/s; (d) 20 mN, 1 µm/s.

It is quite straightforward that maximum wear track deformation varies while changing the normal force, scan speed, and composition. In terms of normal force, by comparing results in Figure 6.15 (a) and (b) under 5 µm/s and Fig 6.15 (c) and (d) under 1 µm/s, the maximum wear track deformation increases in all the compositions by increasing the load from 5 mN to 20 mN. However, with the incorporation of rGO, the increasement in deformation became less. Under 5 µm/s and increasing the normal force from 5 mN to 20 mN, pure HA was increased by 168.1% from 23.2 to 62.2 μm^3, while 1 rGO composite was increased by 83.5% from 23.1 to 54.4 μm^3. This

reinforcement was caused by the local hardening induced by the grain pinning effects of rGO fillers that reduced the deformation of the composite [162]. Furthermore, the 0.5 CNT + 0.5 rGO composite was increased by 146.1% from 24.3 to 59.8 μm3 that its reinforcing effect was inferior to 1 rGO.

The composition effect was more obvious under slower scanning speed (1 μm/s), ie. lower strain rate. At 5 mN normal force, the rGO and/or CNT composites deformed less in wear segment with rGO loading up to 10 wt % and rGO + CNT loading up to 2 wt%. With 1 wt% rGO incorporation, the maximum wear track deformation was reduced from 33.48 μm^3 for pure HA to 19.79 μm^3 for 1 rGO and 23.09 μm^3 for rGO (E), respectively. While maintaining the velocity constant and increasing the normal load to 20 mN, results indicated that the effect of the addition of rGO and CNT on reducing penetration depth was less sensitive.

Table 6-2 Fitting parameters of wear cycle versus maximum wear track deformation under various compositions and test parameters.

Composition	Normal force (mN)	Profiling speed (μm/s)	Fitted curve	Adj. R-Square
HA	5	5	y = 11.630 + 2.226*x - 0.113*x^2	0.973
1 rGO (C)	5	5	y = 11.171 + 2.103*x - 0.098*x^2	0.989
1 rGO (E)	5	5	y = 12.131 + 2.003*x - 0.094*x^2	0.981
2 rGO	5	5	y = 12.015 + 2.046*x - 0.093*x^2	0.971
0.5 rGO + 0.5 CNT	5	5	y = 13.190 + 1.755*x - 0.067*x^2	0.987
1 rGO + 1 CNT	5	5	y = 16.198 + 2.066*x - 0.092*x^2	0.988
HA	20	5	y = 30.184 + 5.241*x - 0.209*x^2	0.996
1 rGO (C)	20	5	y = 29.586 + 5.301*x - 0.246*x^2	0.993
1 rGO (E)	20	5	y = 28.519 + 4.858*x - 0.234*x^2	0.988
2 rGO	20	5	y = 30.698 + 6.033*x - 0.246*x^2	0.995
0.5 rGO + 0.5 CNT	20	5	y = 29.144 + 5.240*x - 0.228*x^2	0.985
HA	5	1	y = 17.579 + 2.834*x - 0.126*x^2	0.990
1 rGO (C)	5	1	y = 9.662 + 1.421*x - 0.043*x^2	0.970
1 rGO (E)	5	1	y = 12.131 + 2.003*x - 0.094*x^2	0.981

5 rGO	5	1	y = 12.904 + 1.985*x - 0.073*x^2	0.996
10 rGO	5	1	y = 16.947 + 1.994*x - 0.067*x^2	0.938
1 rGO + 1 CNT	5	1	y = 15.951 + 2.032*x - 0.079*x^2	0.992
HA	20	1	y = 11.630 + 2.226*x - 0.113*x^2	0.993
1 rGO (C)	20	1	y = 11.171 + 2.102*x - 0.097*x^2	0.987
1 rGO (E)	20	1	y = 12.131 + 2.003*x - 0.094*x^2	0.987
5 rGO	20	1	y = 12.013 + 2.046*x - 0.092*x^2	0.991
10 rGO	20	1	y = 13.189 + 1.754*x - 0.066*x^2	0.980
1 rGO + 1 CNT	20	1	y = 16.197 + 2.066*x - 0.092*x^2	0.993

The addition of rGO and CNT induced wear resistance improvement of HA was also evaluated by calculating the volume removed. Figure 6.16 shows the wear volume loss under various compositions and test conditions. All the tests above demonstrated a nearly perfect linear relationship between wear cycle and accumulated wear loss. The slope of the fitted curve indicates the wear volume loss rate upon cycle number. The Adj. R-Square, standing for the quality of fitting, indicates the material's stability of wear loss rate under nanoscratching wear performance. The Adj. R-Square closer to 1 means the wear volume loss in each cycle is more stable. Under all the four test conditions, the Adj. R-Square of HA was closer to 1 than that of CNT and rGO reinforced composites. Especially, the deviation of Adj. R-Square from 1 increased with increasing the nanocarbon loading. This may arise from the heterogeneous structure of the composites that caused by the difference in size and properties between reinforcement and HA matrix. In this study, both the CNT and rGO are larger than HA grains. The CNT used was multiwalled CNT with an outer diameter of ~120 nm and the rGO were multiple layered ones as well, whereas the sizes of HA grains were less than 100 nm. Nevertheless, these values are all above 0.8 and the fittings are reliable.

Under the gentle wear condition of 5 mN normal force and 5 μm/s velocity, shown in Figure 6.16 (a), the slope of wear volume loss rate was reduced from 0.046 to 0.032 – 0.035 μm^3/cycle by adding 1 wt% nanocarbon (rGO or rGO + CNT hybrid) to HA.

When the nanocarbon contents were increased to 2 wt%, the wear resistance deteriorated with the sloping increased to 0.051-0.053 μm^3/cycle. Under this test condition, the threshold value of the total nanocarbon weight percentage was 1 wt% to improve HA's wear resistance.

By increasing the normal load 4 times from 5 mN to 20 mN and fixing the same velocity of 5 μm/s, shown in Figure 6.16 (b), the above slope was increased significantly to around an order of magnitude for the compositions. Similarly, the threshold was 1 wt% under this condition. However, the wear loss reduction effect between 1 rGO (E) and HA compositions was improved from 30.4 % to 37.2 %, meaning the reinforcement's effect on the improvement of wear resistance was more effective under rush conditions.

By reducing the velocity from 5 μm/s to 1 μm/s, Figure 6.16 (c-d), there was more wear volume loss in all the compositions. However, the nanocarbon weight percentage threshold became higher. Under 5 mN, the threshold increased from 1 wt% up to 10 wt% rGO. While under 20 mN, the threshold increased from 1 wt% up to 5 wt%. Nevertheless, the optimal nanocarbon carbon loading is 1 rGO (E) as well.

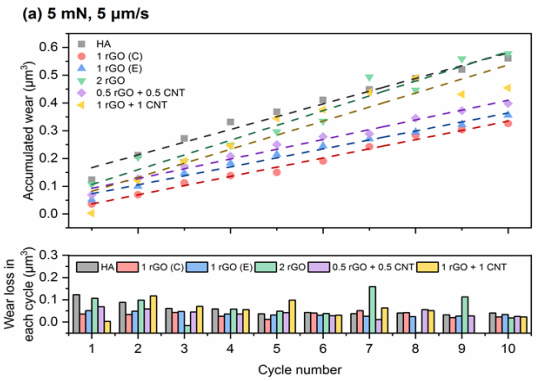

Composition	Slope	Adj. R-Square
HA	0.046	0.975
1 rGO (C)	0.033	0.988
1 rGO (E)	0.032	0.985
2 rGO	0.053	0.947
0.5 rGO + 0.5 CNT	0.035	0.984
1 rGO + 1 CNT	0.051	0.870

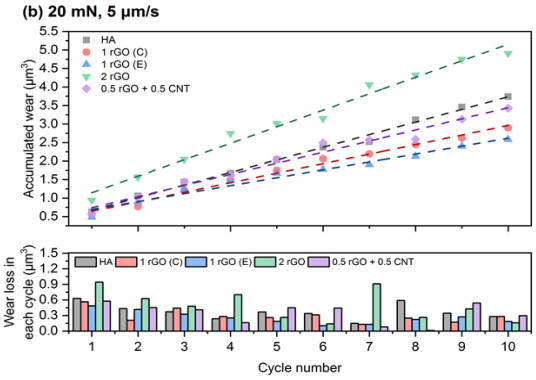

Composition	Slope	Adj. R-Square
HA	0.341	0.993
1 rGO (C)	0.258	0.986
1 rGO (E)	0.214	0.971
2 rGO	0.445	0.980
0.5 rGO + 0.5 CNT	0.300	0.973

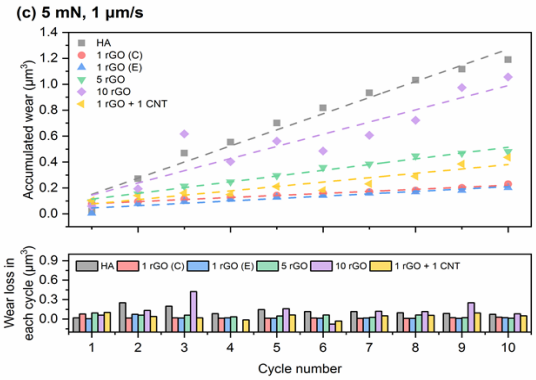

Composition	Slope	Adj. R-Square
HA	0.124	0.968
1 rGO (C)	0.016	0.989
1 rGO (E)	0.018	0.906
5 rGO	0.044	0.982
10 rGO	0.094	0.822
1 rGO + 1 CNT	0.034	0.852

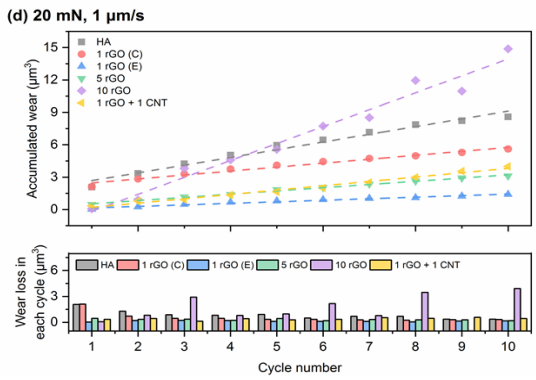

Composition	Slope	Adj. R-Square
HA	0.714	0.973
1 rGO (C)	0.365	0.974
1 rGO (E)	0.142	0.969
5 rGO	0.297	0.994
10 rGO	1.567	0.967
1 rGO + 1 CNT	0.402	0.982

Figure 6.16 Accumulated and each cycle's wear loss under various compositions and test conditions and the parameters of linear fitted curve: (a) 5 mN, 5 μm/s; (b) 20 mN, 5 μm/s; (c) 5 mN, 1 μm/s; (d) 20 mN, 1 μm/s.

By considering the loading force and sliding distance effects on accumulated wear loss, the wear rate (W_r) is defined as

$$W_r = \frac{W_v}{F_p \times L} \quad (6.7)$$

where W_v is the worn volume, F_p is the loading force and L is the sliding distance equal to 100 μm.

The effects of load and velocity in wear segment on wear rate for both pure HA and reinforced composites are compared in Figure 6.17. From Figure 6.17 (a), the wear rate increases with increasing the wear load from 5 mN to 20 mN for all the composites. For pure HA, the wear rate was increased by 66.8%. In the composites, the increasement in wear rate of 1 rGO(C), 1 rGO(E) and 0.5 rGO+0.5 CNT composites show higher values of 112.07%, 81.8%, and 115.4%, respectively. Nonetheless, under ether load, the composites all have a lower wear rate than pure HA.

The rGO reinforcing effect was more relevant to the wear velocity or strain rate, as shown in Figure 6.17 (b). By reducing the velocity from 5 μm/s to 1 μm/s, the wear rate of HA was increased by 112.3% from 112.16 to 238.01 10^{-15} m^3/N.m. However, it has been observed that there was considerably less sensitivity to velocity in rGO reinforced composites. The increase in wear rate were 9.0% and 20.0% for 1 rGO and 2 rGO composites. The results suggest that rGO reinforced composites have higher capabilities to be used as artificial substrates in human beings, under which environments and loads suffered are more complex.

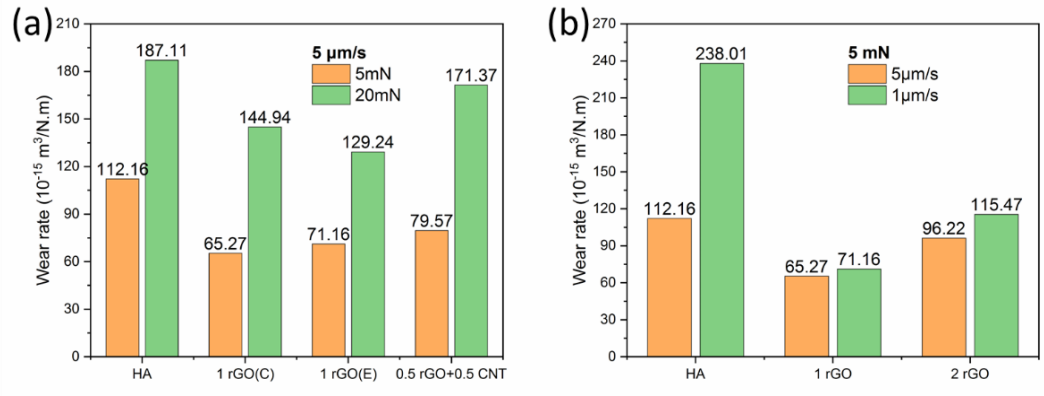

Figure 6.17 Comparison of (a) load and (b) velocity effects on wear rate.

6.3.3 Elastic-plastic behaviors

6.3.3.1 Elasticity before nanoscratching

The plasticity indexes of both rGO and rGO + CNT reinforced HA are smaller than that of pure HA sample, as shown in Figure 6.18. This calculation shows that nanocarbon reinforced HA composites are more prone to recovery upon deformation. Up to 10 wt% rGO as reinforcements, the plasticity index decreases accordingly. A similar trend was also found in rGO + CNT reinforced HA composites.

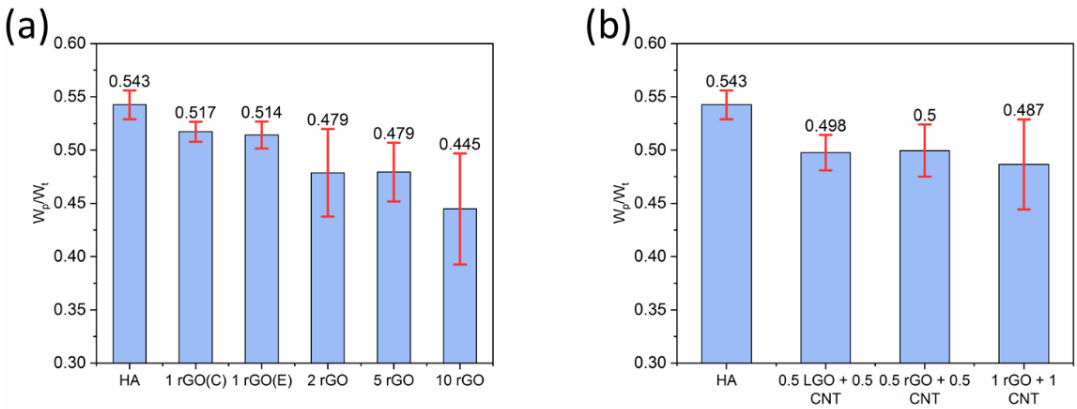

Figure 6.18 Plasticity index of: (a) HA and rGO based composites; (b) HA and rGO + CNT composites.

6.3.3.2 Fatigue properties as a function of wear cycle

The fatigue wear properties were evaluated by calculating the scratch recovery as a function of the wear cycle. The scratch recovery is defined as the ratio between the difference of on-load depth and residual depth, and the on-load depth [195]. To understand the test conditions' effect on materials' scratch recovery properties, the scratch recovery of pure HA under various normal forces and scratch velocities were evaluated. Close examination of data in Figure 6.19 reveals that for HA pellets, by increasing normal load or reducing wear velocity, there is a decreasing trend in scratch recovery as a function of cycle number in the above 4 test conditions. The increase in residual wear depth and decrease in scratch recovery with each cycle confirm that the multiple cycle nanoscratching tests for HA-based materials are a fatigue process [189]. Under higher normal force or slower velocity, the scratch recovery became less and the fatigue process had a higher impact.

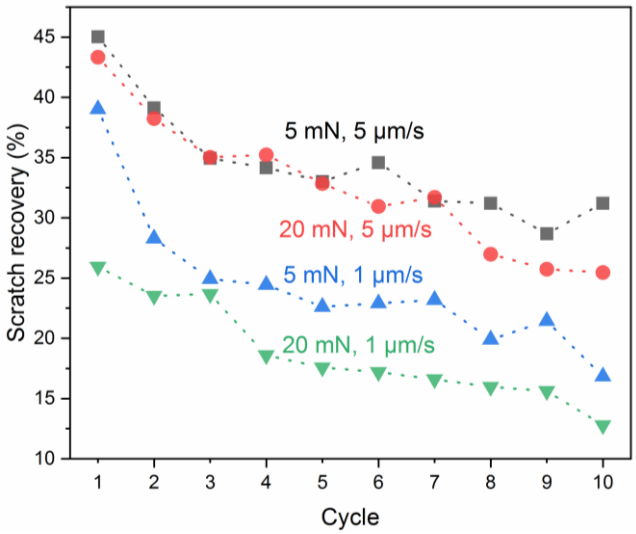

Figure 6.19 Scratch recovery of HA as a function of cycle number under various test conditions.

The scratch recovery properties of various rGO and rGO + CNT composites were evaluated under the above test conditions, shown in Figure 6.20. It is quite

straightforward that the nanocarbon reinforced HA had the same trend of decreasing scratch recovery rate as the cycle number increases. Overall, the scratch recovery properties were significantly enhanced with nanocarbons in the form of rGO or rGO + CNT and contents of up to 10 wt% as reinforcements. Similarly, this trend of increased recovery of the depth with nanocarbon adding and especially in higher nanocarbon contents was observed under the normal nanoindentation process as well. A similar trend was also observed in CNT reinforced Al composites by Arvind el. [196].

It is noted that the mismatch between the trend in the plasticity index and wear rate could be due to the defected areas caused by the introduction of nanocarbons. The dispersion of nanocarbons into the HA matrix was inevitably becoming worse with increasing the contents of nanocarbon. More rGO agglomerates and CNT clusters were found with increasing the nanocarbon loadings that would result in more defected areas that could be removed due to the super high pressure in the scratching process. It can also be explained by comparing the maximum wear track deformation and final wear volume loss. The high elastic recovery of high content composites was not sufficient to compensate for the greater scratch penetration and material removal during the scratch process. The increasement in maximum wear track deformation resulted from the nanocarbon content increasement was higher than that of the composites' scratch recovery abilities.

Overall, the material's recovery rate influenced by normal force and scratching velocity of nanocarbon based composites were distinct from that of pure HA samples, especially under the lower velocity of 1 μm/s.

Under 5 μm/s velocity, shown in Figure 6.20 (a-b), the nanocarbon based composites had ~ 5 % reduction of scratch recovery rate with increasing the load from 5 mN to 20 mN, while HA had half reduction. Under 1 μm/s velocity, shown in Figure 6.20 (c-d),

there is a more distinct trend in scratch recovery between HA and nanocarbon based composites in various compositions. Under either load, the scratch recovery rate became higher for the composites while lower in pure HA sample when the velocity was reduced from 5 μm/s to 1 μm/s. Furthermore, under the harshest condition of 20 mN and 1 μm/s, the scratch recovery rates of nanocarbon based composites were increased with higher nanocarbon contents.

It's also worthy to note that the trend of material recovery properties influenced by rGO and rGO + CNT additions were similar between nanoindentation and multi-cycled scratching tests. Therefore, it is concluded that the addition of nanocarbons improves the elastic recovery of HA in both the transient nanoindentation process and the dynamic multi-cycled nanoscratching process [157].

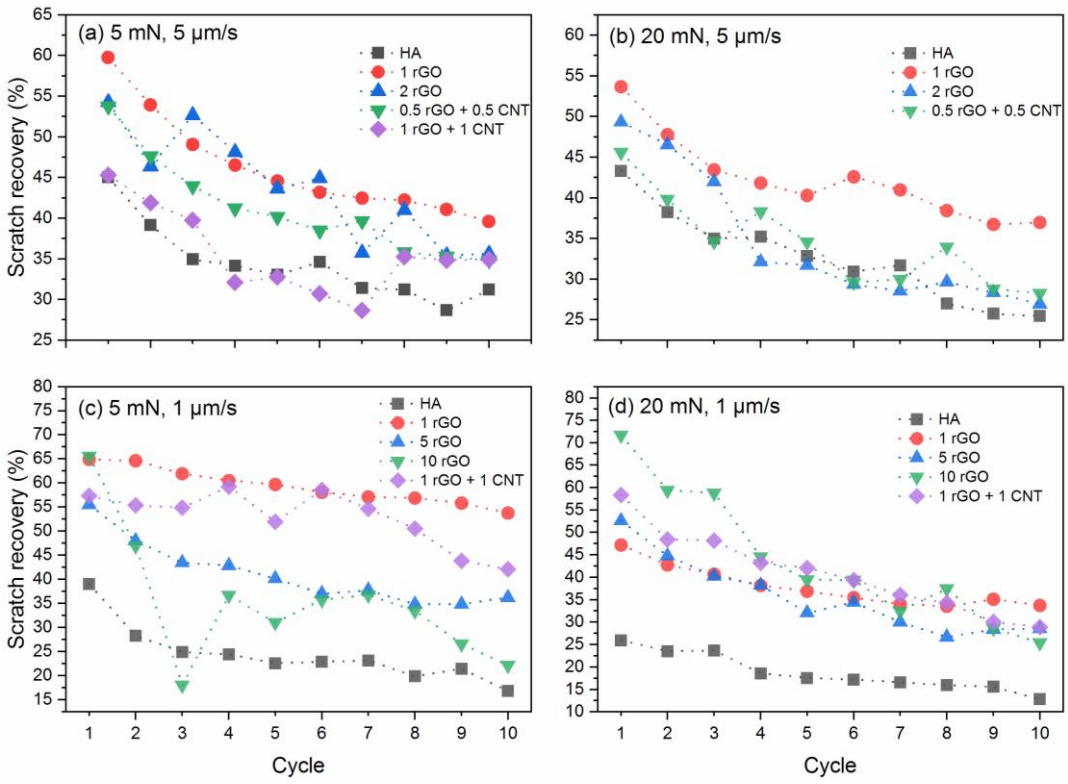

Figure 6.20 Scratch recovery of HA-based composites as a function of cycle number under various test conditions: (a) 5 mN 5 μm/s; (b) 20 mN 5 μm/s; (c) 5 mN 1 μm/s; (d) 20 mN 5 μm/s.

6.3.4 Microstructural characterization

To examine the microstructure change induced by the nanoscratching process, some typical surface morphologies of scratched grooves and wear debris caused after 10 cycle wear process under different compositions and normal forces are shown in Figure 6.21-24.

Figure 6.21 shows the wear track morphologies under 5 mN. The 1 rGO composite displayed the scratches with the narrowest width and least debris that corresponds to the calculated wear volume loss. It can be seen fishbone traces were observed in HA and rGO + CNT wear tracks, while absent in rGO composites. The formation of the fishbone structure was due to the "stick-slip" mechanism that resulted from the competition between static and kinetic friction coefficients during the nanoscratch process [197, 198]. In contrast, the wear track surfaces of 1 rGO were smooth and absent of microcracks. In 2 rGO, the fishbone feature was not observed, while some nano-cracks were formed at the center of wear track, as shown in the interset of Figure 6.21 (c). This proves that under the gentle nanoscratching tests, the rGO based HA composites had the lowest friction forces. The angle of cracks' intersection, ie. plastic flow angle [199], differ in these two compositions. In HA the angle was 107.384 ± 1.768, and the angle in rGO + CNT was 119.314 ± 3.642.

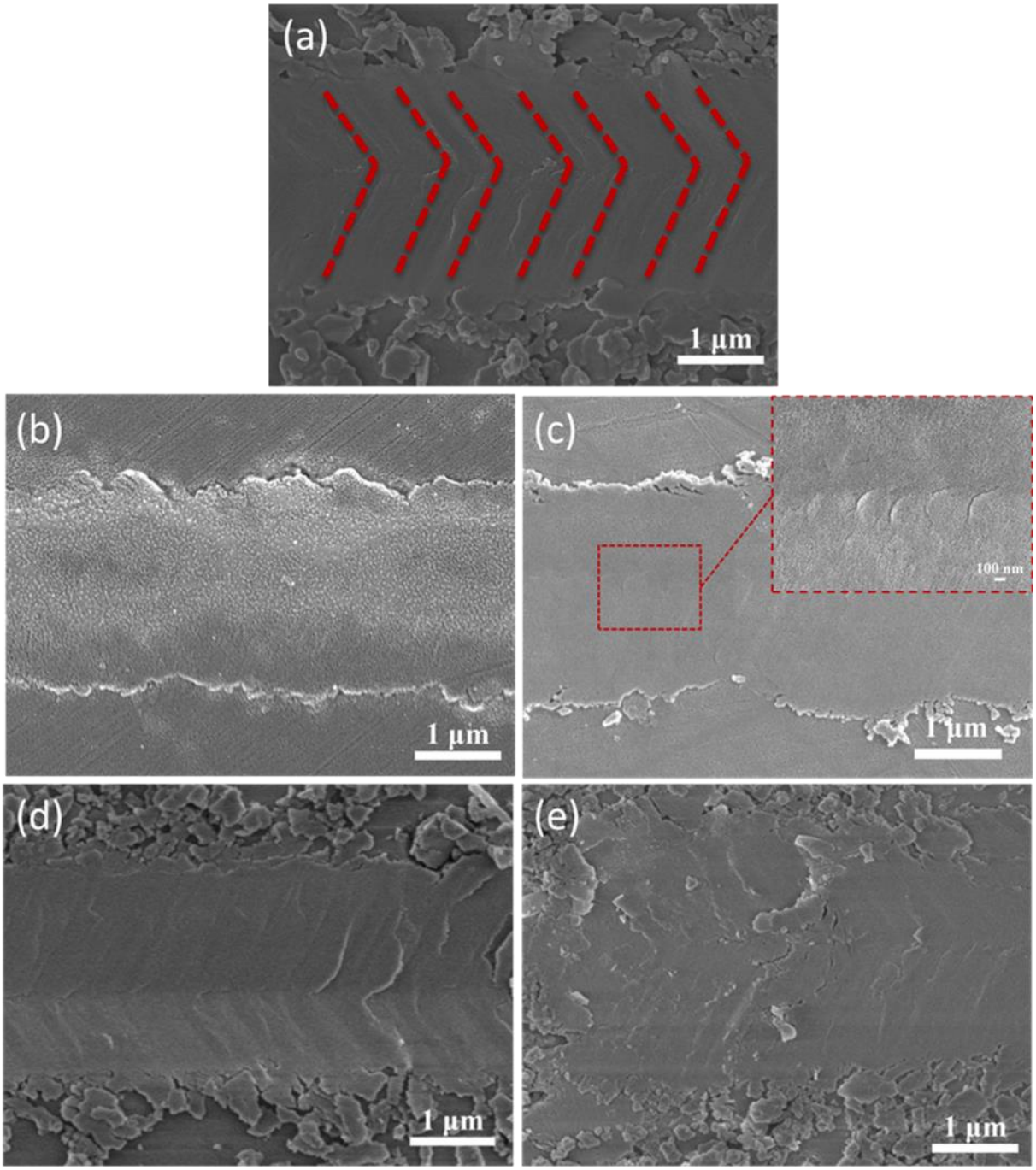

Figure 6.21 Wear track morphologies under 5 mN: (a) HA, 5 μm/s; (b) 1 rGO, 5 μm/s; (c) 2 rGO, 5 μm/s; (d) 0.5 rGO + 0.5 CNT, 1 μm/s; (e) 1 rGO + 1 CNT, 1 μm/s.

Figure 6.22 shows the wear track morphologies under the higher normal force of 20 mN. In any composition, a higher load resulted in more cracks and debris and 1 rGO composite displayed the optimal result as well. Figure 6.22 (c,d) show the morphologies of rGO and CNT hybrid as reinforcements under the total nanocarbon contents of 1 and

2 wt%, respectively. With double nanocarbon content, it can be seen severe cracks occurred and long segments were left along the wear track and on the scratch edges. This results from the increased agglomeration and stacking of nanocarbons at higher contents that can be easily piled up and peeled out under high stresses induced by nanoindenter.

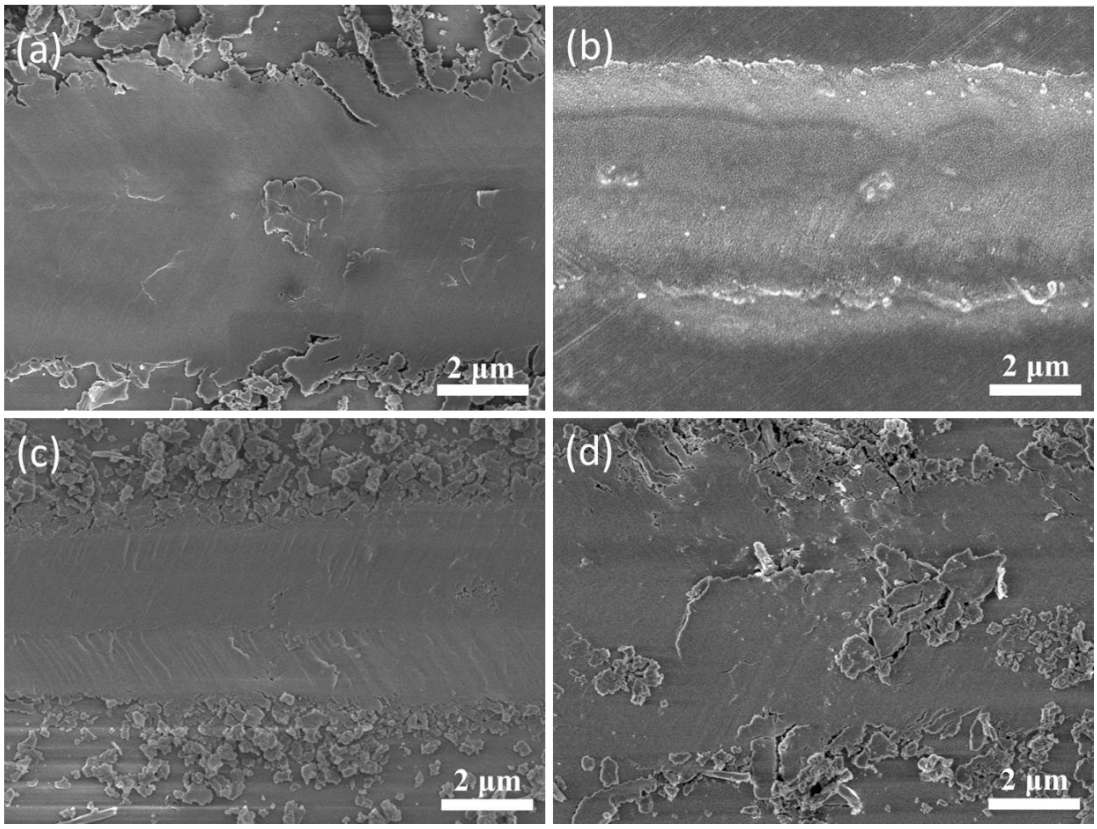

Figure 6.22 Wear track morphologies under 20 mN: (a) HA, 5 μm/s; (b) 1 rGO, 5 μm/s; (c) 0.5 rGO + 0.5 CNT, 1 μm/s; (d) 1 rGO + 1 CNT, 1 μm/s.

For most ceramics under nanoscratching, severe brittle fracture and chips were formed due to the rapid propagation and coalescence of cracks [199]. Figure 6.23 shows the wear debris under 5 mN. With the addition of nanocarbons, the wear debris changed to smaller discontinuous segmental chips. This was due to the lower lateral force by the lubrication effects of rGO and CNT [200].

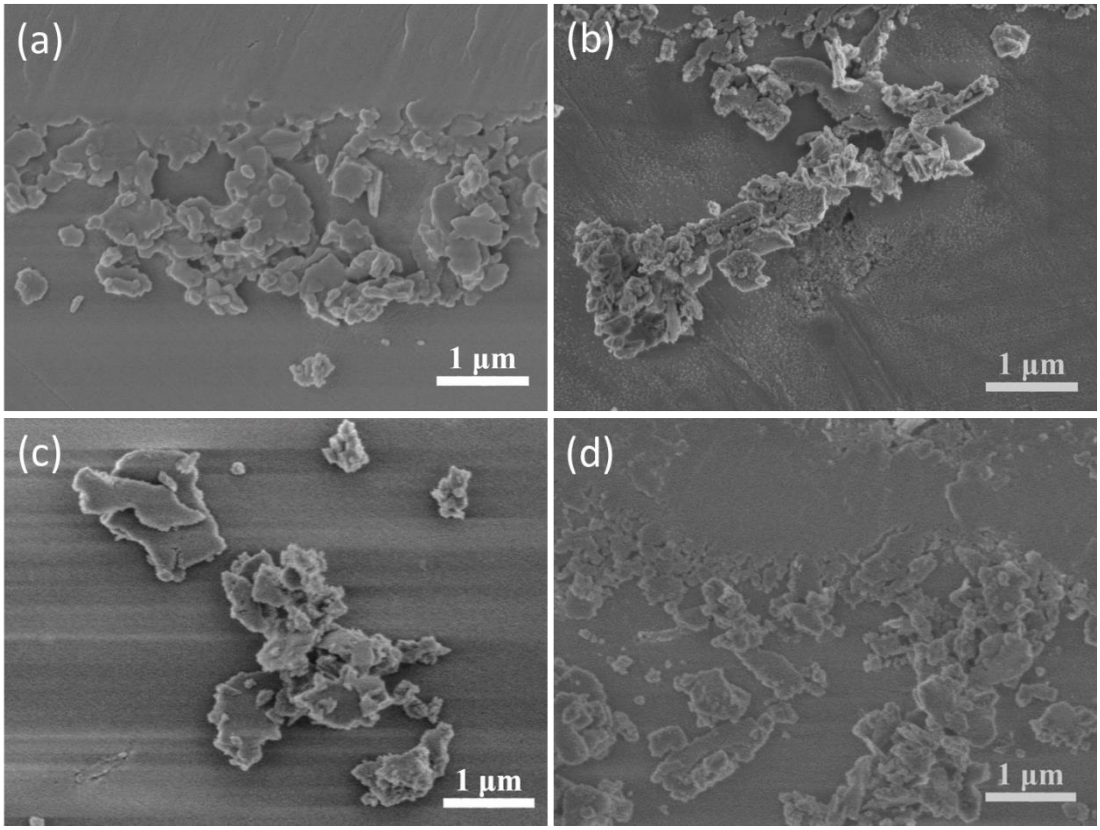

Figure 6.23 Wear debris of under 5 mN: (a) HA, 5 μm/s; (b) 2 rGO, 5 μm/s; (c) 0.5 rGO + 0.5 CNT, 1 μm/s; (d) 1 rGO + 1 CNT, 1 μm/s.

Under the higher normal load of 20 mN, the differences in size and morphology of wear debris were more distinct, shown in Figure 6.24. The wear debris changed from ductile chips to brittle chips generated by crack propagation [201]. In 1 rGO + 1 CNT composite, large rGO and CNT were observed in wear debris.

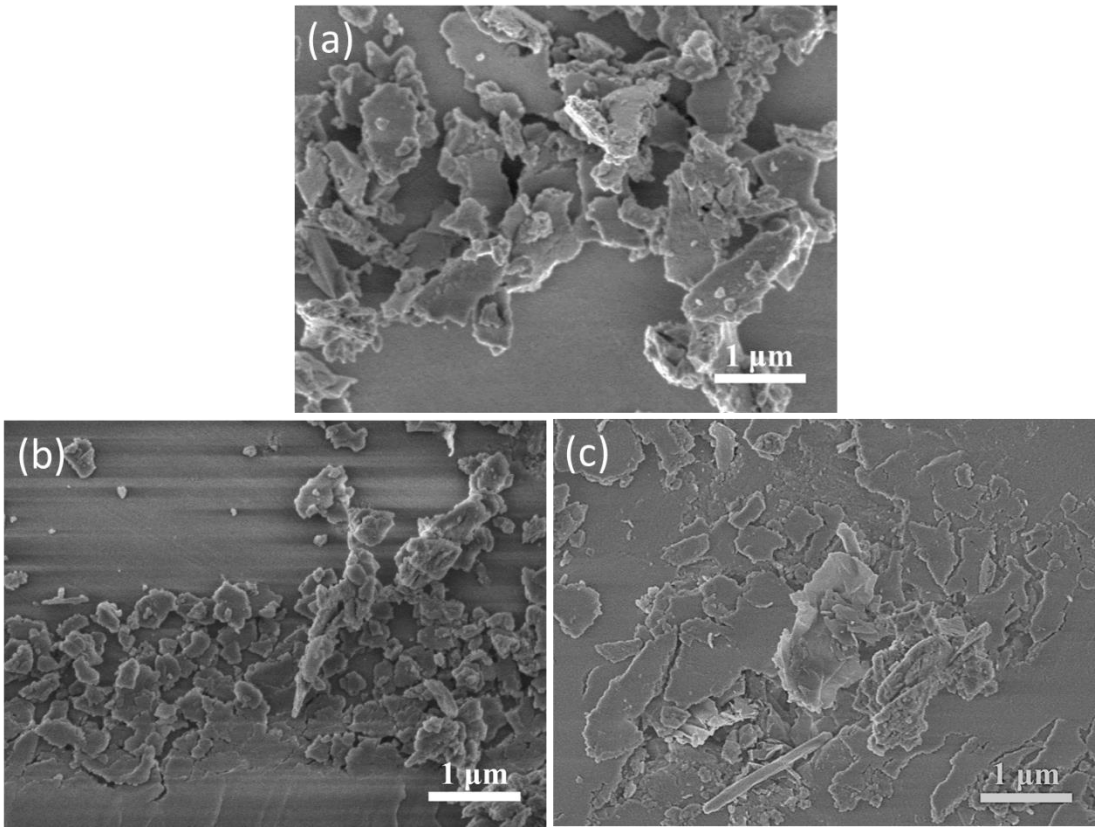

Figure 6.24 Wear debris under 20 mN: (a) HA; (b) 0.5 rGO + 0.5 CNT; (c) 1 rGO + 1 CNT.

Higher magnification FESEM LABE images of 0.5 rGO + 0.5 CNT were taken along the wear tracks to study nanocarbons' behaviors under nanoscratching tests. Figure 6.25 (a) shows CNT survived after the nanoscratching tests and anchored vertically inside the wear track. During nanoscratching tests, CNT bent and served as lubrication media to dissipate the energy to reduce wear. However, some microcracks were formed at the position after the vertically inserted CNT. This may be generated by the stress concentration arisen from the blocking effect of CNT. At higher magnification shown in Figure 6.25 (b), the well-dispersed rGOs were embedded inside the wear track in the direction parallel to the wear track surface. Along the nanoscratching direction, nanoscale cracks were observed to be smaller than 100 nm. The appearance of microcracking indicates the occurrence of brittle fracture during the scratch process that

may propagation to cause chipping in the scratch process. However, these cracks were not seen where rGO embedded. With rGO as reinforcements, rGOs were firmly adhered to the HA matrix and served as lubrication media between HA and indenter to prevent direct contact between the indenter and the composite. Also by the strong interface bonding between HA and rGO or CNT, the stress was reduced. This nano crack propagation inhibition behavior by the introduction of rGO partially contributes to improved wear resistance.

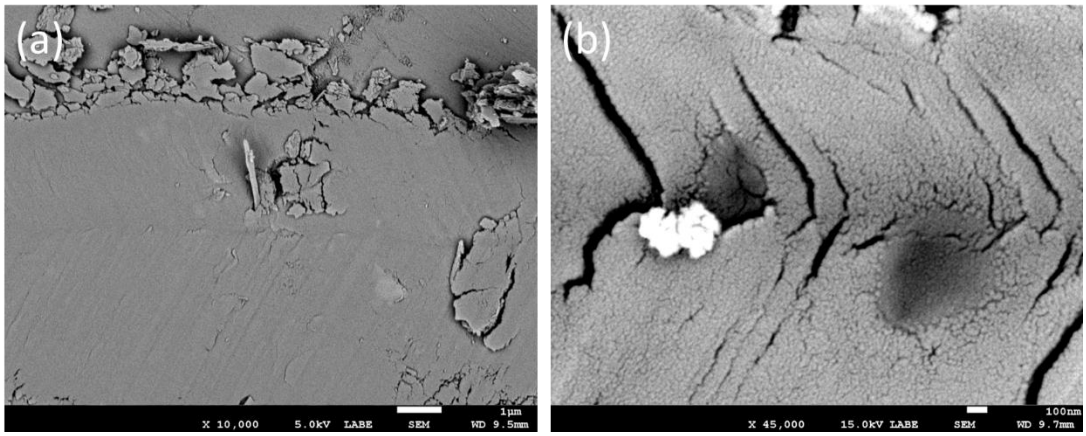

Figure 6.25 LABE wear track morphologies of 0.5 rGO + 0.5 CNT based composite.

6.3.5 Contact pressure

In the nano-scale nanoscratching tests, the contact pressure was evaluated by dividing the normal force (F) with the projected area (A_{proj}) as follows [202]:

$$P_{Ber} = \frac{F}{A_{proj}} \qquad (6.8)$$

and the projected area was calculated by the following formula:

$$A_{proj} = \frac{\sqrt{3}}{4} \times tan^2\left(\frac{\pi}{2} - \alpha\right) \times h_p \times \left(3h_p - 2h_f\right) \qquad (6.9)$$

where α equals to 12.95º, h_p and h_f are penetration depth and recovered depth, respectively.

Typical pressure analysis of HA as a function of cycle number is shown in Figure 6.26. The order of magnitudes was around 8 GPa in the first cycle and dropped to 2.5 GPa in the tenth cycle. To compare the pressure in nanoscratching with that in macro-scale ball-on-disk tribological tests, the contact configuration was regarded as spherical on plate contact and the contact pressure was computed. The maximum Hertzian contact pressure (p_{max}) [203] was 736.9 MPa, while the max shear stress (τ_{max}) was 228.5 MPa within sintered pellets. the pressure in the nanoscratching test was around 1 magnitude higher than that of the ball on disk tests in the present configuration. For GO sheets and graphene sheets, Aksay et. al. calculated the pressure needed to overcome van der waals binding between adjacent layers are 2.5 Mpa and 7.2 MPa, respectively [9]. For multiwall CNTs, the removal of a single graphene layer from multiwall CNT requires a force in the range of 11-63 Gpa [204]. These calculations show that under either scale, rGO was fragmented and thinned while CNT maintained its original structure during the wear tests. CNTs served as the frameworks in the composites and rGOs served as the protecting films during the tests.

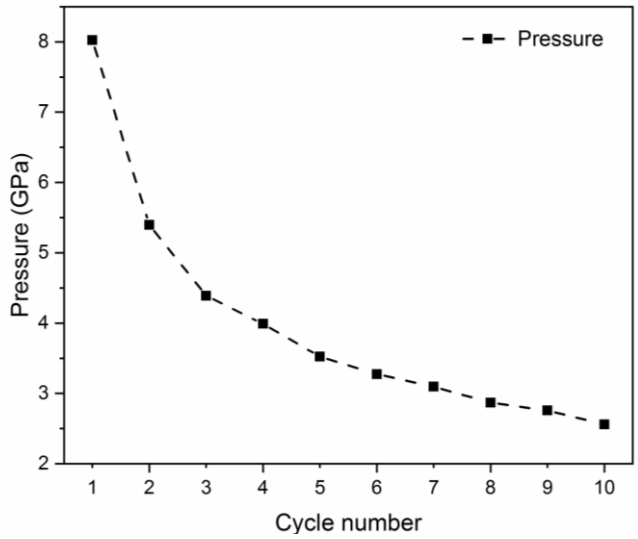

Figure 6.26 Contact pressure of HA as a function of cycle number tested under 5 mN and 5 μm/s nano-scale tribological test.

6.3.6 Comparison between micro- and nano- scale wear results

With 1 wt% nanocarbon content as reinforcements, the wear resistance of HA was strengthened both in nano- and micro- scale by adding rGO and rGO + CNT. The trend in nano-scale wear rate with varying the nanocarbon morphology corresponds with that of macro-scale wear and solo rGO is superior to the combination of rGO and CNT. With 2 wt %, nanocarbon content as reinforcements, the behaviors of nano- and micro-tribological tests became more distinct. In nanoscratching tests, the wear rates became higher in both rGO and rGO +CNT reinforced HA composites. However, in the ball on disk tests, the lowest wear rate in all the compositions of 1.09 10^{-15} m^3/N.m was achieved by using CNT + rGO hybrid as reinforcements. Therefore, the wear resistance of rGO and CNT reinforced HA was found to be strongly dependent on both the test conditions and reinforcements: (a) nano- and micro- scale wear behaviors; (b) the concentration and morphology of nanocarbon.

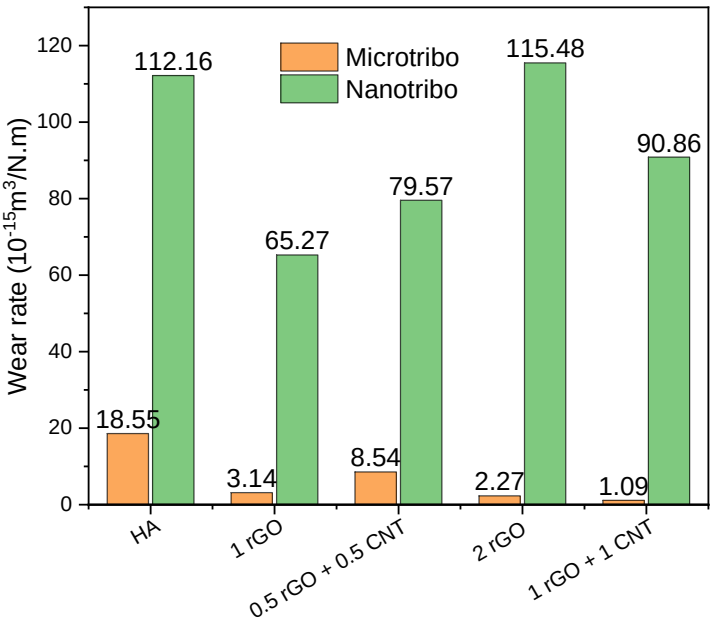

Figure 6.27 Comparison of nano- and micro- tribo results of various compositions.

6.4 Summary

By introducing rGO and CNT as reinforcements in HA bioceramic, the wear resistance was improved both at the micro- and nano- scale. However, the reinforcing effects and mechanisms diverse:

1. In the micro-scale ball-on-disk tribological tests, the wear resistance and friction performances were strongly dependent on nanocarbon content and morphology. By increasing the total nanocarbon loadings from 1 wt.% to 2 wt.%, the wear resistivity of both rGO and rGO + CNT reinforced composites were substantially increased. Under 2 wt% total nanocarbon content and the morphology of rGO/CNT hybrid, the wear resistance was improved ~17 times with the incorporation of 1 wt.% rGO and 1 wt.% CNT.
2. The reinforcing mechanism was due to the formation of carbonaceous films between the surfaces of composite and counterbody that served as solid lubrication films. The formation of tribo film was confirmed by FESEM, EDS and Raman analyses. The tribo film resulted in lower friction of coefficient, higher hardness, and hardness over modulus ratio that contribute to the improved wear performance.
3. In the case of nanoscratching tribology test, the wear and fatigue performances were dependent on nanocarbon morphology, nanocarbon content, normal force and wear velocity. The maximum wear track deformation, wear volume loss and elastic recovery rate were evaluated as a function of wear cycle. The maximum wear track deformation and wear volume loss demonstrated nearly quadratic and linear relations, respectively.
4. The 1 rGO composite exhibited ~3.35 times lower wear rate than that of pure HA under 1 μm/s and 5 mN condition. The reinforcing mechanism was due to

the lubrication and pinning effects of rGO, that resulted in higher resistance to penetration, elastic recovery capability, low-cycle fatigue resistance, and microcrack propagation inhibition properties.

In summary, the results at both micro- and nano- scale suggested that rGO and CNT reinforced HA bioceramic composites have higher long-term capabilities to be used as artificial substrates in human beings to sustain the complex environments and load scales. The durability of HA reinforced with rGO and CNT is enhanced and the clinical applications of HA are expected to be extended.

Chapter 7 Conclusions and suggested future work

7.1 Conclusions

The conclusions of this thesis are summarized as follows:

1. The content of rGO reinforcements was up to 2 wt% to reinforce HA bioceramics. The hardness, Young's modulus and fracture toughness of the composites were increased with 1 and 2 wt% rGO additions and reduced with 5 and 10 wt% rGO as reinforcements. By adding 2 wt% rGO as reinforcements, the hardness and fracture toughness of HA based composites were increased by 32.2 % and 27.7%, respectively. With increasing rGO concentration, the densification rates of the composites were decreased, and the number of rGO agglomerations and porosities were increased. The improvement in mechanical properties was mainly attributed to the microstructural refinement of the composites, the high intrinsic properties of rGO, and the crack bridging and branching mechanisms by rGO. *(Section 4.2)*
2. In terms of mixing method, all the ultrasonication mixed and ball milled 1 wt% rGO reinforced HA composites were almost fully densified. The hardness and fracture toughness of SPSed pellets were improved in all the rGO-HA composites, and the highest values were obtained in the composites mixed with ultrasonication in ethanol solvent. Although high-speed wet ball milling method facilitated to disperse nanocarbons into HA bioceramics well, a large number of defects were introduced simultaneously. In contrast, the ultrasonication mixing method was superior with similar dispersion efficiency but fewer defects generated on rGO. *(Section 4.3)*

3. In terms of using 1 type of nanocarbons, the size and shape of nanocarbons significantly influenced the structural and mechanical behaviors of the reinforced composites. The highest hardness and fracture toughness were in SPSed rGO-HA and the CNT-HA composites, with 30.6 % and 43.1 % improvements than pure HA samples, respectively. In rGO-HA composites, the rGO plates with large lateral dimensions could wrap HA grains for finer and layered microstructures of the composites. In CNT-HA composites, the interactions between CNTs and HA matrixes were enhanced by the formation of the unique mechanical locking structures in CNTs. *(Section 5.1)*
4. In terms of using rGO and CNT hybrid as reinforcement, the optimum dispersion of rGOs and CNTs, and strong interface bonding between the nanocarbons and HA matrixes were established in the composites. Furthermore, the small-sized CNTs were found inserted to rGO plates in the mixed powder and sintered pellets. As a result, the HA composites reinforced with rGO and CNT hybrid showed a significant improvement in mechanical properties with higher hardness and fracture toughness than the ones reinforced with 1 type of nanocarbon. *(Section 5.2)*
5. In the micro-scale ball-on-disk tribological tests, the wear resistance and friction performances were strongly dependent on nanocarbon content and morphology. By increasing the total nanocarbon contents from 1 wt.% to 2 wt.%, the wear resistance of both rGO and rGO + CNT hybrids reinforced composites were substantially increased. Under 2 wt% total nanocarbon content and the morphology as rGO and CNT hybrids, the wear rate was reduced by 94.2 % than monolithic HA. *(Section 6.2)*

6. In the nano-scale tribological tests, the wear and fatigue performances were dependent on nanocarbon morphology, nanocarbon content, normal force and wear velocity. The maximum wear track deformation and wear volume loss demonstrated nearly perfect quadratic and linear relations, respectively. The 1 rGO composites exhibited ~3.35 times lower wear rate than that of pure HA sample under the test conditions of 1 μm/s scratching speed and 5 mN normal force. The reinforcing mechanism was due to the lubrication and pinning effects of rGO, that resulted in higher resistance to penetration, higher elastic recovery capability, low-cycle fatigue resistance, and nano-crack propagation inhibition properties. *(Section 6.3)*

To sum up, by varying nanocarbon content, and optimizing the mixing method and nanocarbon morphology, the HA bioceramics were strengthened and toughened. Furthermore, the tribological results at both micro- and nano- scale suggested that nanocarbon reinforced HA bioceramic composites had higher wear resistance, indicating their higher long-term capabilities to sustain the complex environments and load scales.

7.2 Suggested future work

The suggested future work are as follows:

1. *Evaluating the biological properties of the densified composites*.

   As the biological performances of bioceramics are critical when implanted into human tissues [205], the biocompatibility and bioactivity of the densified samples are suggested to be evaluated. In this account, *in vitro* experiments, namely simulated body fluid (SBF) immersion and cell culturing, are suggested

for bioceramics with/without the reinforcements to study influences and interactions between nanocarbons and HA matrixes in biological aspect.

2. *Evaluating the electrical properties of nanocarbon reinforced composites*.

   The natural bone is the electrically-active porous nanocomposite material [206] and the dielectric properties of HA are useful for bone repairing [207]. It has already been proved that the externally applied electrical stimulation can potentially enhance the osseointegration *in vitro* and *in vivo* [208], and the DC electrical conductivity can be improved by several orders of magnitudes in ceramics [209-211]. In this aspect, the permittivity of the nanocarbon reinforced HA is suggested to be investigated to seek novel cure methods for bone repair.

3. *Investigating the feasibility and performance of using novel nanostructured fillers in bioceramics*.

   In recent years, the surge in graphene as fillers for composite applications has stimulated interest in the investigation of various other nanomaterials [212]. Among the various newly derived 1D or 2D nano-reinforcements, phosphorene and silicene are suggested to be studied as reinforcements in bioceramics. They are potentially effective reinforcements in bioceramics not only due to their large surface areas and strong intrinsic mechanical properties, but also because of their compositional similarities with the bone that are promising for excellent biological properties.

References

[1] F.J. O'Brien, Biomaterials & scaffolds for tissue engineering, Materials Today 14(3) (2011) 88-95.

[2] S.V. Dorozhkin, Bioceramics of calcium orthophosphates, Biomaterials 31(7) (2010) 1465-85.

[3] J. Zhang, W. Liu, V. Schnitzler, F. Tancret, J.M. Bouler, Calcium phosphate cements for bone substitution: chemistry, handling and mechanical properties, Acta Biomater 10(3) (2014) 1035-49.

[4] L.L. Hench, Bioceramics - from Concept to Clinic, J Am Ceram Soc 74(7) (1991) 1487-1510.

[5] M. Prakasam, J. Locs, K. Salma-Ancane, D. Loca, A. Largeteau, L. Berzina-Cimdina, Fabrication, Properties and Applications of Dense Hydroxyapatite: A Review, J Funct Biomater 6(4) (2015) 1099-140.

[6] Y. Liu, J. Huang, M. Niinomi, H. Li, Inhibited grain growth in hydroxyapatite–graphene nanocomposites during high temperature treatment and their enhanced mechanical properties, Ceram Int 42(9) (2016) 11248-11255.

[7] S. Baradaran, E. Moghaddam, W.J. Basirun, M. Mehrali, M. Sookhakian, M. Hamdi, M.R.N. Moghaddam, Y. Alias, Mechanical properties and biomedical applications of a nanotube hydroxyapatite-reduced graphene oxide composite, Carbon 69 (2014) 32-45.

[8] Y.-J. Wan, L.-C. Tang, D. Yan, L. Zhao, Y.-B. Li, L.-B. Wu, J.-X. Jiang, G.-Q. Lai, Improved dispersion and interface in the graphene/epoxy composites via a facile surfactant-assisted process, Compos Sci Technol 82 (2013) 60-68.

[9] M.J. McAllister, J.-L. Li, D.H. Adamson, H.C. Schniepp, A.A. Abdala, J. Liu, M. Herrera-Alonso, D.L. Milius, R. Car, R.K. Prud'homme, I.A. Aksay, Single Sheet Functionalized Graphene by Oxidation and Thermal Expansion of Graphite, Chem Mater 19(18) (2007) 4396-4404.

[10] A. Zeinedini, M.M. Shokrieh, A. Ebrahimi, The effect of agglomeration on the fracture toughness of CNTs-reinforced nanocomposites, Theoretical and Applied Fracture Mechanics 94 (2018) 84-94.

[11] T. Gong, J. Xie, J. Liao, T. Zhang, S. Lin, Y. Lin, Nanomaterials and bone regeneration, Bone Res 3 (2015) 15029.

[12] W. Wang, K.W.K. Yeung, Bone grafts and biomaterials substitutes for bone defect repair: A review, Bioact Mater 2(4) (2017) 224-247.

[13] M. Aminzare, A. Eskandari, M.H. Baroonian, A. Berenov, Z. Razavi Hesabi, M. Taheri, S.K. Sadrnezhaad, Hydroxyapatite nanocomposites: Synthesis, sintering and mechanical properties, Ceram Int 39(3) (2013) 2197-2206.

[14] S.V. Dorozhkin, Multiphasic calcium orthophosphate (CaPO 4) bioceramics and their biomedical applications, Ceram Int 42(6) (2016) 6529-6554.

[15] J.-Y. Rho, L. Kuhn-Spearing, P. Zioupos, Mechanical properties and the hierarchical structure of bone, Medical Engineering & Physics 20(2) (1998) 92-102.

[16] R. Murugan, S. Ramakrishna, Development of nanocomposites for bone grafting, Compos Sci Technol 65(15-16) (2005) 2385-2406.

[17] R. Dimitriou, E. Jones, D. McGonagle, P.V. Giannoudis, Bone regeneration: current concepts and future directions, BMC medicine 9(1) (2011) 66.

[18] R. Agarwal, A.J. Garcia, Biomaterial strategies for engineering implants for enhanced osseointegration and bone repair, Adv Drug Deliv Rev 94 (2015) 53-62.

[19] N. Eliaz, N. Metoki, Calcium Phosphate Bioceramics: A Review of Their History, Structure, Properties, Coating Technologies and Biomedical Applications, Materials (Basel) 10(4) (2017).

[20] S. Feroz, A.S. Khan, 7.1 Structure of hydroxyapatite, Handbook of Ionic Substituted Hydroxyapatites (2019) 175.

[21] J.H. Shepherd, D.V. Shepherd, S.M. Best, Substituted hydroxyapatites for bone repair, Journal of materials science. Materials in medicine 23(10) (2012) 2335-47.

[22] P. Cheang, K. Khor, Addressing processing problems associated with plasma spraying of hydroxyapatite coatings, Biomaterials 17(5) (1996) 537-544.

[23] M.I. Kay, R.A. Young, A.S. Posner, Crystal Structure of Hydroxyapatite, Nature 204(4963) (1964) 1050-1052.

[24] H.B. Guo, X. Miao, Y. Chen, P. Cheang, K.A. Khor, Characterization of hydroxyapatite- and bioglass-316L fibre composites prepared by spark plasma sintering, Mater Lett 58(3-4) (2004) 304-307.

[25] F. Gao, C.Y. Xu, H.T. Hu, Q. Wang, Y.Y. Gao, H. Chen, Q.N. Guo, D.Z. Chen, D. Eder, Biomimetic synthesis and characterization of hydroxyapatite/graphene oxide hybrid coating on Mg alloy with enhanced corrosion resistance, Mater Lett 138(0) (2015) 25-28.

[26] G. Miranda, A. Araújo, F. Bartolomeu, M. Buciumeanu, O. Carvalho, J.C.M. Souza, F.S. Silva, B. Henriques, Design of Ti6Al4V-HA composites produced by hot pressing for biomedical applications, Mater Design 108 (2016) 488-493.

[27] E. Fidancevska, G. Ruseska, J. Bossert, Y.-M. Lin, A.R. Boccaccini, Fabrication and characterization of porous bioceramic composites based on hydroxyapatite and titania, Materials Chemistry and Physics 103(1) (2007) 95-100.

[28] V.B. Mohan, K.-t. Lau, D. Hui, D. Bhattacharyya, Graphene-based materials and their composites: A review on production, applications and product limitations, Composites Part B: Engineering 142 (2018) 200-220.

[29] I.A. Kinloch, J. Suhr, J. Lou, R.J. Young, P.M. Ajayan, Composites with carbon nanotubes and graphene: An outlook, Science 362(6414) (2018) 547-553.

[30] H. Xie, T. Cao, F.J. Rodriguez-Lozano, E.K. Luong-Van, V. Rosa, Graphene for the development of the next-generation of biocomposites for dental and medical applications, Dent Mater 33(7) (2017) 765-774.

[31] A. Nieto, A. Bisht, D. Lahiri, C. Zhang, A. Agarwal, Graphene reinforced metal and ceramic matrix composites: a review, Int Mater Rev (2016) 1-62.

[32] P. Palmero, Structural ceramic nanocomposites: a review of properties and powders' synthesis methods, Nanomaterials 5(2) (2015) 656-696.

[33] X. Xie, M. Cerruti, Graphene-Bioceramic Composites, Handbook of Bioceramics and Biocomposites (2016) 431-467.

[34] S. Stankovich, D.A. Dikin, G.H. Dommett, K.M. Kohlhaas, E.J. Zimney, E.A. Stach, R.D. Piner, S.T. Nguyen, R.S. Ruoff, Graphene-based composite materials, Nature 442(7100) (2006) 282-6.

[35] A.K. Geim, K.S. Novoselov, The rise of graphene, Nat Mater 6(3) (2007) 183-91.

[36] X. Zhang, B.R.S. Rajaraman, H.H. Liu, S. Ramakrishna, Graphene's potential in materials science and engineering, Rsc Advances 4(55) (2014) 28987-29011.

[37] Y. Li, J.C. Wu, N. Chopra, Nano-carbon-based hybrids and heterostructures: progress in growth and application for lithium-ion batteries, J Mater Sci 50(24) (2015) 7843-7865.

[38] H.C. Zhang, G. Gruner, Y.L. Zhao, Recent advancements of graphene in biomedicine, J Mater Chem B 1(20) (2013) 2542-2567.

[39] V.C. Tung, L.M. Chen, M.J. Allen, J.K. Wassei, K. Nelson, R.B. Kaner, Y. Yang, Low-temperature solution processing of graphene-carbon nanotube hybrid materials for high-performance transparent conductors, Nano Lett 9(5) (2009) 1949-55.

[40] D. Yu, L. Dai, Self-assembled graphene/carbon nanotube hybrid films for supercapacitors, The Journal of Physical Chemistry Letters 1(2) (2009) 467-470.

[41] M.A. Rafiee, J. Rafiee, Z. Wang, H. Song, Z.Z. Yu, N. Koratkar, Enhanced mechanical properties of nanocomposites at low graphene content, ACS Nano 3(12) (2009) 3884-90.

[42] L.S. Walker, V.R. Marotto, M.A. Rafiee, N. Koratkar, E.L. Corral, Toughening in graphene ceramic composites, ACS Nano 5(4) (2011) 3182-90.

[43] S.R. Shin, Y.C. Li, H.L. Jang, P. Khoshakhlagh, M. Akbari, A. Nasajpour, Y.S. Zhang, A. Tamayol, A. Khademhosseini, Graphene-based materials for tissue engineering, Adv Drug Deliv Rev 105(Pt B) (2016) 255-274.

[44] C.J. Shearer, A. Cherevan, D. Eder, Application and future challenges of functional nanocarbon hybrids, Adv Mater 26(15) (2014) 2295-318.

[45] C. Lee, X. Wei, J.W. Kysar, J. Hone, Measurement of the elastic properties and intrinsic strength of monolayer graphene, Science 321(5887) (2008) 385-8.

[46] Y. Zhu, S. Murali, W. Cai, X. Li, J.W. Suk, J.R. Potts, R.S. Ruoff, Graphene and graphene oxide: synthesis, properties, and applications, Adv Mater 22(35) (2010) 3906-24.

[47] D. Chen, H. Feng, J. Li, Graphene oxide: preparation, functionalization, and electrochemical applications, Chem Rev 112(11) (2012) 6027-53.

[48] D. Lahiri, S. Ghosh, A. Agarwal, Carbon nanotube reinforced hydroxyapatite composite for orthopedic application: A review, Mat Sci Eng C-Mater 32(7) (2012) 1727-1758.

[49] G. Mittal, V. Dhand, K.Y. Rhee, S.J. Park, W.R. Lee, A review on carbon nanotubes and graphene as fillers in reinforced polymer nanocomposites, Journal of Industrial and Engineering Chemistry 21 (2015) 11-25.

[50] X.L. Xie, Y.W. Mai, X.P. Zhou, Dispersion and alignment of carbon nanotubes in polymer matrix: A review, Mat Sci Eng R 49(4) (2005) 89-112.

[51] T. Kokubo, H. Takadama, How useful is SBF in predicting in vivo bone bioactivity?, Biomaterials 27(15) (2006) 2907-2915.

[52] A. Abbott, Cell culture: biology's new dimension, Nature 424(6951) (2003) 870-2.

[53] I. Ahmad, B. Yazdani, Y.Q. Zhu, Recent Advances on Carbon Nanotubes and Graphene Reinforced Ceramics Nanocomposites, Nanomaterials 5(1) (2015) 90-114.

[54] H. Schmidt, Chemistry of material preparation by the sol-gel process, J Non-Cryst Solids 100(1-3) (1988) 51-64.

[55] Q.G. Jiang, Z.M. Ao, D.W. Chu, Q. Jiang, Reversible Transition of Graphene from Hydrophobic to Hydrophilic in the Presence of an Electric Field, Journal of Physical Chemistry C 116(36) (2012) 19321-19326.

[56] P. Harshit, T. Peter, G. Salvatore, H. Chunfeng, R.B. Aldo, D. Ivo, J.R. Mike, Toughened and machinable glass matrix composites reinforced with graphene and graphene-oxide nano platelets, Science and Technology of Advanced Materials 14(5) (2013) 055007.

[57] D.R. Dreyer, S. Park, C.W. Bielawski, R.S. Ruoff, The chemistry of graphene oxide, Chem Soc Rev 39(1) (2010) 228-40.

[58] T. Kuila, S. Bose, A.K. Mishra, P. Khanra, N.H. Kim, J.H. Lee, Chemical functionalization of graphene and its applications, Progress in Materials Science 57(7) (2012) 1061-1105.

[59] J.D. Randall, D.J. Eyckens, L. Servinis, F. Stojcevski, L.A. O'Dell, T.R. Gengenbach, B. Demir, T.R. Walsh, L.C. Henderson, Designing carbon fiber composite interfaces using a 'graft-to' approach: Surface grafting density versus interphase penetration, Carbon 146 (2019) 88-96.

[60] X. Zhang, C. Shi, E. Liu, N. Zhao, C. He, Effect of Interface Structure on the Mechanical Properties of Graphene Nanosheets Reinforced Copper Matrix Composites, ACS Appl Mater Interfaces 10(43) (2018) 37586-37601.

[61] K.S. Hu, D.D. Kulkarni, I. Choi, V.V. Tsukruk, Graphene-polymer nanocomposites for structural and functional applications, Progress in Polymer Science 39(11) (2014) 1934-1972.

[62] R.O. Ritchie, The conflicts between strength and toughness, Nat. Mater. 10(11) (2011) 817-822.

[63] Y. Liu, Y. Liu, Q. Zhang, C. Zhang, J. Wang, Y. Wu, P. Han, Z. Gao, L. Wang, X. Wu, Control of the microstructure and mechanical properties of electrodeposited graphene/Ni composite, Materials Science and Engineering: A 727 (2018) 133-139.

[64] B. Milsom, H. Porwal, G. Viola, Z. Gao, M.J. Reece, Understanding and quantification of grain growth mechanism in ZrO2-carbon nanotube composites, Mater Design 133 (2017) 325-331.

[65] D.G. Papageorgiou, I.A. Kinloch, R.J. Young, Mechanical properties of graphene and graphene-based nanocomposites, Progress in Materials Science 90 (2017) 75-127.

[66] G. Muralithran, S. Ramesh, The effects of sintering temperature on the properties of hydroxyapatite, Ceram Int 26(2) (2000) 221-230.

[67] B.N. Kim, K. Hiraga, K. Morita, H. Yoshida, Y.J. Park, Y. Sakka, Dynamic grain growth during low-temperature spark plasma sintering of alumina, Scripta Mater 80 (2014) 29-32.

[68] M. Li, P. Xiong, F. Yan, S. Li, C. Ren, Z. Yin, A. Li, H. Li, X. Ji, Y. Zheng, Y. Cheng, An overview of graphene-based hydroxyapatite composites for orthopedic applications, Bioact Mater 3(1) (2018) 1-18.

[69] S.C. Zhang, W.G. Fahrenholtz, G.E. Hilmas, E.J. Yadlowsky, Pressureless sintering of carbon nanotube–Al2O3 composites, J Eur Ceram Soc 30(6) (2010) 1373-1380.

[70] P. Rutkowski, L. Stobierski, D. Zientara, L. Jaworska, P. Klimczyk, M. Urbanik, The influence of the graphene additive on mechanical properties and wear of hot-pressed Si3N4 matrix composites, J Eur Ceram Soc 35(1) (2015) 87-94.

[71] M. Shahedi Asl, M. Ghassemi Kakroudi, Characterization of hot-pressed graphene reinforced ZrB2-SiC composite, Mater. Sci. Eng. A 625 (2015) 385-392.

[72] Y. Cheng, Y. Zhang, T. Wan, Z. Yin, J. Wang, Mechanical properties and toughening mechanisms of graphene platelets reinforced Al2O3/TiC composite ceramic tool materials by microwave sintering, Materials Science and Engineering: A 680 (2017) 190-196.

[73] A. Nieto, D. Lahiri, A. Agarwal, Graphene NanoPlatelets reinforced tantalum carbide consolidated by spark plasma sintering, Materials Science and Engineering: A 582 (2013) 338-346.

[74] P. Guyot, G. Antou, N. Pradeilles, A. Weibel, M. Vandenhende, G. Chevallier, A. Peigney, C. Estournes, A. Maitre, Hot pressing and spark plasma sintering of alumina: Discussion about an analytical modelling used for sintering mechanism determination, Scripta Mater 84-85 (2014) 35-38.

[75] Q.Z. Xu, X. Ai, J. Zhao, W.Z. Qin, Y.T. Wang, F. Gong, Comparison of Ti(C,N)-based cermets processed by hot-pressing sintering and conventional pressureless sintering, Journal of Alloys and Compounds 619 (2015) 538-543.

[76] R. Orru, R. Licheri, A.M. Locci, A. Cincotti, G.C. Cao, Consolidation/synthesis of materials by electric current activated/assisted sintering, Mat Sci Eng R 63(4-6) (2009) 127-287.

[77] D.M. Hulbert, A. Anders, D.V. Dudina, J. Andersson, D. Jiang, C. Unuvar, U. Anselmi-Tamburini, E.J. Lavernia, A.K. Mukherjee, The absence of plasma in "spark plasma sintering", J Appl Phys 104(3) (2008).

[78] A. Nieto, D. Lahiri, A. Agarwal, Synthesis and properties of bulk graphene nanoplatelets consolidated by spark plasma sintering, Carbon 50(11) (2012) 4068-4077.

[79] J.E. Garay, Current-Activated, Pressure-Assisted Densification of Materials, Annu Rev Mater Res 40 (2010) 445-468.

[80] I. Bajpai, D.Y. Kim, Y.H. Han, B.K. Jang, S. Kim, Directional property evaluation of spark plasma sintered GNPs-reinforced hydroxyapatite composites, Mater Lett 158(0) (2015) 62-65.

[81] F. Chen, Y.J. Zhu, K.W. Wang, K.L. Zhao, Surfactant-free solvothermal synthesis of hydroxyapatite nanowire/nanotube ordered arrays with biomimetic structures, Crystengcomm 13(6) (2011) 1858-1863.

[82] W.S. Hummers, R.E. Offeman, Preparation of Graphitic Oxide, Journal of the American Chemical Society 80(6) (1958) 1339-1339.

[83] Z.J. Fan, J.Q. Wang, Z.F. Wang, H.Q. Ran, Y. Li, L.Y. Niu, P.W. Gong, B. Liu, S.R. Yang, One-pot synthesis of graphene/hydroxyapatite nanorod composite for tissue engineering, Carbon 66(0) (2014) 407-416.

[84] H. Hu, X. Wang, J. Wang, L. Wan, F. Liu, H. Zheng, R. Chen, C. Xu, Preparation and properties of graphene nanosheets–polystyrene nanocomposites via in situ emulsion polymerization, Chemical Physics Letters 484(4-6) (2010) 247-253.

[85] S. Erakovic, A. Jankovic, D. Veljovic, E. Palcevskis, M. Mitric, T. Stevanovic, D. Janackovic, V. Miskovic-Stankovic, Corrosion stability and bioactivity in simulated

body fluid of silver/hydroxyapatite and silver/hydroxyapatite/lignin coatings on titanium obtained by electrophoretic deposition, J Phys Chem B 117(6) (2013) 1633-43.

[86] S. Erakovic, D. Veljovic, P.N. Diouf, T. Stevanovic, M. Mitric, D. Janackovic, I.Z. Matic, Z.D. Juranic, V. Miskovic-Stankovic, The effect of lignin on the structure and characteristics of composite coatings electrodeposited on titanium, Progress in Organic Coatings 75(4) (2012) 275-283.

[87] A. Jankovic, S. Erakovic, M. Mitric, I.Z. Matic, Z.D. Juranic, G.C.P. Tsui, C.Y. Tang, V. Miskovic-Stankovic, K.Y. Rhee, S.J. Park, Bioactive hydroxyapatite/graphene composite coating and its corrosion stability in simulated body fluid, Journal of Alloys and Compounds 624 (2015) 148-157.

[88] A. Jankovic, S. Erakovic, M. Vukasinovic-Sekulic, V. Miskovic-Stankovic, S.J. Park, K.Y. Rhee, Graphene-based antibacterial composite coatings electrodeposited on titanium for biomedical applications, Progress in Organic Coatings 83 (2015) 1-10.

[89] E. Champion, Sintering of calcium phosphate bioceramics, Acta Biomater 9(4) (2013) 5855-75.

[90] S. Klebert, C. Balazsi, K. Balazsi, E. Bodis, P. Fazekas, A.M. Keszler, J. Szepvolgyi, Z. Karoly, Spark plasma sintering of graphene reinforced hydroxyapatite composites, Ceram Int 41(3) (2015) 3647-3652.

[91] M. Li, Q. Liu, Z.J. Jia, X.C. Xu, Y. Cheng, Y.F. Zheng, T.F. Xi, S.C. Wei, Graphene oxide/hydroxyapatite composite coatings fabricated by electrophoretic nanotechnology for biological applications, Carbon 67(0) (2014) 185-197.

[92] M. Li, Q. Liu, Z.J. Jia, X.C. Xu, Y.Y. Shi, Y. Cheng, Y.F. Zheng, T.F. Xi, S.C. Wei, Electrophoretic deposition and electrochemical behavior of novel graphene oxide-hyaluronic acid-hydroxyapatite nanocomposite coatings, Appl Surf Sci 284(0) (2013) 804-810.

[93] M. Li, Y.B. Wang, Q. Liu, Q.H. Li, Y. Cheng, Y.F. Zheng, T.F. Xi, S.C. Wei, In situ synthesis and biocompatibility of nano hydroxyapatite on pristine and chitosan functionalized graphene oxide, J Mater Chem B 1(4) (2013) 475-484.

[94] H.Y. Liu, P.X. Xi, G.Q. Xie, Y.J. Shi, F.P. Hou, L. Huang, F.J. Chen, Z.Z. Zeng, C.W. Shao, J. Wang, Simultaneous Reduction and Surface Functionalization of Graphene Oxide for Hydroxyapatite Mineralization, Journal of Physical Chemistry C 116(5) (2012) 3334-3341.

[95] Y. Liu, Z.H. Dang, Y.Y. Wang, J. Huang, H. Li, Hydroxyapatite/graphene-nanosheet composite coatings deposited by vacuum cold spraying for biomedical applications: Inherited nanostructures and enhanced properties, Carbon 67(0) (2014) 250-259.

[96] Y. Liu, J. Huang, H. Li, Synthesis of hydroxyapatite-reduced graphite oxide nanocomposites for biomedical applications: oriented nucleation and epitaxial growth of hydroxyapatite, J Mater Chem B 1(13) (2013) 1826-1834.

[97] G.M. Neelgund, A. Oki, Z. Luo, In-situ deposition of hydroxyapatite on graphene nanosheets, Mater Res Bull 48(2) (2013) 175-179.

[98] J.D. Nunez, A.M. Benito, R. Gonzalez, J. Aragon, R. Arenal, W.K. Maser, Integration and bioactivity of hydroxyapatite grown on carbon nanotubes and graphene oxide, Carbon 79(1) (2014) 590-604.

[99] G.M. Neelgund, K. Olurode, A. Oki, A simple and rapid method to graft hydroxyapatite on carbon nanotubes, Materials science & engineering. C, Materials for biological applications 31(7) (2011) 1477-1481.

[100] A. Oyefusi, O. Olanipekun, G.M. Neelgund, D. Peterson, J.M. Stone, E. Williams, L. Carson, G. Regisford, A. Oki, Hydroxyapatite grafted carbon nanotubes and graphene nanosheets: promising bone implant materials, Spectrochimica acta. Part A, Molecular and biomolecular spectroscopy 132(0) (2014) 410-6.

[101] J.H. Wang, Z.F. Ouyang, Z.W. Ren, J.F. Li, P.P. Zhang, G. Wei, Z.Q. Su, Self-assembled peptide nanofibers on graphene oxide as a novel nanohybrid for biomimetic mineralization of hydroxyapatite, Carbon 89(0) (2015) 20-30.

[102] J.H. Wang, H.X. Wang, Y.Z. Wang, J.F. Li, Z.Q. Su, G. Wei, Alternate layer-by-layer assembly of graphene oxide nanosheets and fibrinogen nanofibers on a silicon substrate for a biomimetic three-dimensional hydroxyapatite scaffold, J Mater Chem B 2(42) (2014) 7360-7368.

[103] C. Li, L. Zhao, J. Han, R. Wang, C. Xiong, X. Xie, Synthesis of citrate-stabilized hydrocolloids of hydroxyapatite through a novel two-stage method: a possible aggregates-breakdown mechanism of colloid formation, J Colloid Interface Sci 360(2) (2011) 341-9.

[104] X. Xie, K. Hu, D. Fang, L. Shang, S.D. Tran, M. Cerruti, Graphene and hydroxyapatite self-assemble into homogeneous, free standing nanocomposite hydrogels for bone tissue engineering, Nanoscale 7(17) (2015) 7992-8002.

[105] Y.J. Yan, X.J. Zhang, H.H. Mao, Y. Huang, Q.Q. Ding, X.F. Pang, Hydroxyapatite/gelatin functionalized graphene oxide composite coatings deposited on TiO2 nanotube by electrochemical deposition for biomedical applications, Appl Surf Sci 329(0) (2015) 76-82.

[106] L. Zhang, W.W. Liu, C.G. Yue, T.H. Zhang, P. Li, Z.W. Xing, Y. Chen, A tough graphene nanosheet/hydroxyapatite composite with improved in vitro biocompatibility, Carbon 61(0) (2013) 105-115.

[107] J. Zhao, Z.C. Zhang, Z.W. Yu, Z.N. He, S.S. Yang, H.Y. Jiang, Nucleation and characterization of hydroxyapatite on thioglycolic acid-capped reduced graphene oxide/silver nanoparticles in simplified simulated body fluid, Appl Surf Sci 289(0) (2014) 89-96.

[108] Z. Li, S. Bi, B.C. Thompson, R. Li, K.A. Khor, Multifunctional bioceramic-based composites reinforced with silica-coated carbon nanotube core-shell structures, Ceram Int 43(18) (2017) 16084-16093.

[109] F. Tuinstra, J.L. Koenig, Raman spectrum of graphite, The Journal of Chemical Physics 53(3) (1970) 1126-1130.

[110] J. Liu, U. Khan, J. Coleman, B. Fernandez, P. Rodriguez, S. Naher, D. Brabazon, Graphene oxide and graphene nanosheet reinforced aluminium matrix composites: Powder synthesis and prepared composite characteristics, Mater Design 94 (2016) 87-94.

[111] N. Li, Y.L. Cheng, Q. Song, Z.Y. Jiang, M.L. Tang, G.S. Cheng, Graphene meets biology, Chinese Science Bulletin 59(13) (2014) 1341-1354.

[112] M. Mehrali, E. Moghaddam, S.F. Shirazi, S. Baradaran, M. Mehrali, S.T. Latibari, H.S. Metselaar, N.A. Kadri, K. Zandi, N.A. Osman, Synthesis, mechanical properties,

and in vitro biocompatibility with osteoblasts of calcium silicate-reduced graphene oxide composites, ACS Appl Mater Interfaces 6(6) (2014) 3947-62.

[113] C.B. Ponton, R.D. Rawlings, Vickers indentation fracture toughness test Part 1 Review of literature and formulation of standardised indentation toughness equations, Materials Science and Technology 5(9) (1989) 865-872.

[114] G.R. Anstis, P. Chantikul, B.R. Lawn, D.B. Marshall, A Critical Evaluation of Indentation Techniques for Measuring Fracture Toughness: I, Direct Crack Measurements, J Am Ceram Soc 64(9) (1981) 533-538.

[115] H. Tsuda, J. Arends, Orientational micro-Raman spectroscopy on hydroxyapatite single crystals and human enamel crystallites, J Dent Res 73(11) (1994) 1703-1710.

[116] A. Antonakos, E. Liarokapis, T. Leventouri, Micro-Raman and FTIR studies of synthetic and natural apatites, Biomaterials 28(19) (2007) 3043-54.

[117] G. Cheng, Y. Zhang, H. Yin, Y. Ruan, Y. Sun, K. Lin, Effects of strontium substitution on the structural distortion of hydroxyapatite by rietveld refinement and Raman Spectroscopy, Ceram Int 45(8) (2019) 11073-11078.

[118] S. Koutsopoulos, Synthesis and characterization of hydroxyapatite crystals: a review study on the analytical methods, Journal of biomedical materials research 62(4) (2002) 600-12.

[119] L.M. Malard, M.A. Pimenta, G. Dresselhaus, M.S. Dresselhaus, Raman spectroscopy in graphene, Phys Rep 473(5-6) (2009) 51-87.

[120] A.C. Ferrari, D.M. Basko, Raman spectroscopy as a versatile tool for studying the properties of graphene, Nat Nanotechnol 8(4) (2013) 235-46.

[121] X. Wang, J. Zhang, X. Zhang, Y. Zhu, Characterization, uniformity and photo-catalytic properties of graphene/TiO2 nanocomposites via Raman mapping, Opt Express 25(18) (2017) 21496-21508.

[122] X. Yang, T. Zou, C. Shi, E. Liu, C. He, N. Zhao, Effect of carbon nanotube (CNT) content on the properties of in-situ synthesis CNT reinforced Al composites, Materials Science and Engineering: A 660 (2016) 11-18.

[123] L. Stobinski, B. Lesiak, A. Malolepszy, M. Mazurkiewicz, B. Mierzwa, J. Zemek, P. Jiricek, I. Bieloshapka, Graphene oxide and reduced graphene oxide studied by the XRD, TEM and electron spectroscopy methods, Journal of Electron Spectroscopy and Related Phenomena 195 (2014) 145-154.

[124] A. Gallardo-López, I. Márquez-Abril, A. Morales-Rodríguez, A. Muñoz, R. Poyato, Dense graphene nanoplatelet/yttria tetragonal zirconia composites: Processing, hardness and electrical conductivity, Ceram Int 43(15) (2017) 11743-11752.

[125] J.-H. Shin, J. Choi, M. Kim, S.-H. Hong, Comparative study on carbon nanotube- and reduced graphene oxide-reinforced alumina ceramic composites, Ceram Int 44(7) (2018) 8350-8357.

[126] C. Xiong, T. Li, A. Dang, T. Zhao, H. Li, H. Lv, Two-step approach of fabrication of three-dimensional MnO2-graphene-carbon nanotube hybrid as a binder-free supercapacitor electrode, Journal of Power Sources 306 (2016) 602-610.

[127] J.B. Wu, M.L. Lin, X. Cong, H.N. Liu, P.H. Tan, Raman spectroscopy of graphene-based materials and its applications in related devices, Chem Soc Rev 47(5) (2018) 1822-1873.

[128] A. McCreary, Q. An, A.M. Forster, K. Liu, S. He, C.W. Macosko, A. Stein, A.R. Hight Walker, Raman imaging of surface and sub-surface graphene oxide in fiber reinforced polymer nanocomposites, Carbon 143 (2019) 793-801.

[129] O. Tapasztó, L. Tapasztó, H. Lemmel, V. Puchy, J. Dusza, C. Balázsi, K. Balázsi, High orientation degree of graphene nanoplatelets in silicon nitride composites prepared by spark plasma sintering, Ceram Int 42(1) (2016) 1002-1006.

[130] H. Seiner, C. Ramirez, M. Koller, P. Sedlák, M. Landa, P. Miranzo, M. Belmonte, M.I. Osendi, Elastic properties of silicon nitride ceramics reinforced with graphene nanofillers, Mater Design 87 (2015) 675-680.

[131] C. Ramirez, L. Garzón, P. Miranzo, M.I. Osendi, C. Ocal, Electrical conductivity maps in graphene nanoplatelet/silicon nitride composites using conducting scanning force microscopy, Carbon 49(12) (2011) 3873-3880.

[132] H. Du, S.D. Pang, Dispersion and stability of graphene nanoplatelet in water and its influence on cement composites, Construction and Building Materials 167 (2018) 403-413.

[133] F. Chen, D. Jin, K. Tyeb, B. Wang, Y.-H. Han, S. Kim, J.M. Schoenung, Q. Shen, L. Zhang, Field assisted sintering of graphene reinforced zirconia ceramics, Ceram Int 41(4) (2015) 6113-6116.

[134] S. Grigoriev, P. Peretyagin, A. Smirnov, W. Solís, L.A. Díaz, A. Fernández, R. Torrecillas, Effect of graphene addition on the mechanical and electrical properties of Al 2 O 3 -SiCw ceramics, J Eur Ceram Soc 37(6) (2017) 2473-2479.

[135] M.S. Asl, M.G. Kakroudi, Characterization of hot-pressed graphene reinforced ZrB2–SiC composite, Materials Science and Engineering: A 625 (2015) 385-392.

[136] H. Li, A. Misra, Y. Zhu, Z. Horita, C.C. Koch, T.G. Holesinger, Processing and characterization of nanostructured Cu-carbon nanotube composites, Materials Science and Engineering: A 523(1-2) (2009) 60-64.

[137] X. Wang, Q. Jiang, W. Xu, W. Cai, Y. Inoue, Y. Zhu, Effect of carbon nanotube length on thermal, electrical and mechanical properties of CNT/bismaleimide composites, Carbon 53 (2013) 145-152.

[138] H. Wan, F. Delale, L. Shen, Effect of CNT length and CNT-matrix interphase in carbon nanotube (CNT) reinforced composites, Mechanics Research Communications 32(5) (2005) 481-489.

[139] F.H. Gojny, M.H. Wichmann, B. Fiedler, K. Schulte, Influence of different carbon nanotubes on the mechanical properties of epoxy matrix composites–a comparative study, Compos Sci Technol 65(15-16) (2005) 2300-2313.

[140] A.J. Albaaji, E.G. Castle, M.J. Reece, J.P. Hall, S.L. Evans, Effect of ball-milling time on mechanical and magnetic properties of carbon nanotube reinforced FeCo alloy composites, Mater Design 122 (2017) 296-306.

[141] V. Bundy, M. Chauhan, C. Fitch, P. Modi, K. Morsi, Effect of Carbon Nanotube (CNT) Length on the Mechanical Milling of Ni-CNT Powders and Ni-CNT/Al Reactive Synthesis, Metallurgical and Materials Transactions A 49(12) (2018) 6351-6358.

[142] R. Xu, Z. Tan, D. Xiong, G. Fan, Q. Guo, J. Zhang, Y. Su, Z. Li, D. Zhang, Balanced strength and ductility in CNT/Al composites achieved by flake powder metallurgy via shift-speed ball milling, Composites Part A: Applied Science and Manufacturing 96 (2017) 57-66.

[143] J.W. Suk, R.D. Piner, J. An, R.S. Ruoff, Mechanical properties of monolayer graphene oxide, ACS nano 4(11) (2010) 6557-6564.

[144] N. Yousefi, M.M. Gudarzi, Q. Zheng, X. Lin, X. Shen, J. Jia, F. Sharif, J.-K. Kim, Highly aligned, ultralarge-size reduced graphene oxide/polyurethane nanocomposites: mechanical properties and moisture permeability, Composites Part A: Applied Science and Manufacturing 49 (2013) 42-50.

[145] B. Ye, C. An, Y. Zhang, C. Song, X. Geng, J. Wang, One-Step Ball Milling Preparation of Nanoscale CL-20/Graphene Oxide for Significantly Reduced Particle Size and Sensitivity, Nanoscale Res Lett 13(1) (2018) 42.

[146] K. Gong, Z. Pan, A.H. Korayem, L. Qiu, D. Li, F. Collins, C.M. Wang, W.H. Duan, Reinforcing effects of graphene oxide on portland cement paste, Journal of Materials in Civil Engineering 27(2) (2014) A4014010.

[147] S.-H. Jang, S. Kawashima, H. Yin, Influence of carbon nanotube clustering on mechanical and electrical properties of cement pastes, Mater. 9(4) (2016) 220.

[148] S. Parveen, S. Rana, R. Fangueiro, M.C. Paiva, Microstructure and mechanical properties of carbon nanotube reinforced cementitious composites developed using a novel dispersion technique, Cement and Concrete Research 73 (2015) 215-227.

[149] M.K. Shin, B. Lee, S.H. Kim, J.A. Lee, G.M. Spinks, S. Gambhir, G.G. Wallace, M.E. Kozlov, R.H. Baughman, S.J. Kim, Synergistic toughening of composite fibres by self-alignment of reduced graphene oxide and carbon nanotubes, Nat Commun 3 (2012) 650.

[150] S. Chatterjee, F. Nafezarefi, N.H. Tai, L. Schlagenhauf, F.A. Nuesch, B.T.T. Chu, Size and synergy effects of nanofiller hybrids including graphene nanoplatelets and carbon nanotubes in mechanical properties of epoxy composites, Carbon 50(15) (2012) 5380-5386.

[151] W. Li, A. Dichiara, J. Bai, Carbon nanotube–graphene nanoplatelet hybrids as high-performance multifunctional reinforcements in epoxy composites, Compos Sci Technol 74 (2013) 221-227.

[152] W.B. Zhang, Z.X. Zhang, J.H. Yang, T. Huang, N. Zhang, X.T. Zheng, Y. Wang, Z.W. Zhou, Largely enhanced thermal conductivity of poly(vinylidene fluoride)/carbon nanotube composites achieved by adding graphene oxide, Carbon 90 (2015) 242-254.

[153] M. Khan, A.B. Yousaf, M. Chen, C. Wei, X. Wu, N. Huang, Z. Qi, L. Li, Molybdenum sulfide/graphene-carbon nanotube nanocomposite material for electrocatalytic applications in hydrogen evolution reactions, Nano Research 9(3) (2016) 837-848.

[154] A. A, D. Menon, S. T. B, M. Koyakutty, C.C. Mohan, S.V. Nair, M.B. Nair, Bioinspired Composite Matrix Containing Hydroxyapatite–Silica Core–Shell Nanorods for Bone Tissue Engineering, ACS Applied Materials & Interfaces 9(32) (2017) 26707-26718.

[155] Y.F. Chen, J.Q. Bi, C.L. Yin, G.L. You, Microstructure and fracture toughness of graphene nanosheets/alumina composites, Ceram Int 40 (2014) 13883-13889.

[156] M. Fellah, M. Abdul Samad, M. Labaiz, O. Assala, A. Iost, Sliding friction and wear performance of the nano-bioceramic α-Al2O3 prepared by high energy milling, Tribology International 91 (2015) 151-159.

[157] B.D. Beake, T.W. Liskiewicz, Comparison of nano-f`retting and nano-scratch tests on biomedical materials, Tribology International 63 (2013) 123-131.

[158] W.J. Basirun, B. Nasiri-Tabrizi, S. Baradaran, Overview of Hydroxyapatite–Graphene Nanoplatelets Composite as Bone Graft Substitute: Mechanical Behavior and In-vitro Biofunctionality, Critical Reviews in Solid State and Materials Sciences 43(3) (2017) 177-212.

[159] Z. Lu, Y. Liu, B. Liu, M. Liu, Friction and wear behavior of hydroxyapatite based composite ceramics reinforced with fibers, Mater Design 39 (2012) 444-449.

[160] S.H. Teoh, R. Thampuran, W.K.H. Seah, Coefficient of friction under dry and lubricated conditions of a fracture and wear resistant P/M titanium-graphite composite for biomedical applications, Wear 214(2) (1998) 237-244.

[161] K. Balani, S.P. Harimkar, A. Keshri, Y. Chen, N.B. Dahotre, A. Agarwal, Multiscale wear of plasma-sprayed carbon-nanotube-reinforced aluminum oxide nanocomposite coating, Acta Mater 56(20) (2008) 5984-5994.

[162] D. Lahiri, V. Singh, A.K. Keshri, S. Seal, A. Agarwal, Carbon nanotube toughened hydroxyapatite by spark plasma sintering: Microstructural evolution and multiscale tribological properties, Carbon 48(11) (2010) 3103-3120.

[163] P.-C. Tsai, Y.-R. Jeng, J.-T. Lee, I. Stachiv, P. Sittner, Effects of carbon nanotube reinforcement and grain size refinement mechanical properties and wear behaviors of carbon nanotube/copper composites, Diamond and Related Materials 74 (2017) 197-204.

[164] A. Bhadauria, L.K. Singh, T. Laha, Nanoindentation and nanoscratch properties of graphene nanoplatelets reinforced spark plasma sintered aluminium-based nanocomposite, Advances in Materials and Processing Technologies (2019) 1-8.

[165] A. El-Ghazaly, G. Anis, H.G. Salem, Effect of graphene addition on the mechanical and tribological behavior of nanostructured AA2124 self-lubricating metal matrix composite, Composites Part A: Applied Science and Manufacturing 95 (2017) 325-336.

[166] F. Gutiérrez-Mora, A. Morales-Rodríguez, A. Gallardo-López, R. Poyato, Tribological behavior of graphene nanoplatelet reinforced 3YTZP composites, J Eur Ceram Soc 39(4) (2019) 1381-1388.

[167] Z. Huang, Z. Zheng, S. Zhao, S. Dong, P. Luo, L. Chen, Copper matrix composites reinforced by aligned carbon nanotubes: Mechanical and tribological properties, Mater Design 133 (2017) 570-578.

[168] W. Ji, Y. Yuan, B. Zou, S. Dai, H. Zhang, Friction and wear behaviour of cemented carbide tool materials sliding against Al 2 O 3 and Si 3 N 4 ceramics under dry condition, Ceram Int 44(14) (2018) 17486-17491.

[169] J. Llorente, B. Román-Manso, P. Miranzo, M. Belmonte, Tribological performance under dry sliding conditions of graphene/silicon carbide composites, J Eur Ceram Soc 36(3) (2016) 429-435.

[170] P. Flores, Modeling and simulation of wear in revolute clearance joints in multibody systems, Mechanism and Machine Theory 44(6) (2009) 1211-1222.

[171] Y.-T. Cheng, C.-M. Cheng, Scaling, dimensional analysis, and indentation measurements, Materials Science and Engineering: R: Reports 44(4-5) (2004) 91-149.

[172] Y. Chen, S.R. Bakshi, A. Agarwal, Correlation between nanoindentation and nanoscratch properties of carbon nanotube reinforced aluminum composite coatings, Surface and Coatings Technology 204(16-17) (2010) 2709-2715.

[173] L.-N. Zhu, B.-S. Xu, H.-D. Wang, C.-B. Wang, Measurement of Residual Stresses Using Nanoindentation Method, Critical Reviews in Solid State and Materials Sciences 40(2) (2014) 77-89.

[174] Z. Hu, W. Lu, M.D. Thouless, J.R. Barber, Effect of plastic deformation on the evolution of wear and local stress fields in fretting, International Journal of Solids and Structures 82 (2016) 1-8.

[175] Elastic deformation and the laws of friction, Proceedings of the Royal Society of London. Series A. Mathematical and Physical Sciences 243(1233) (1957) 190-205.

[176] G.M. Choi, J. Jin, D. Shin, Y.H. Kim, J.H. Ko, H.G. Im, J. Jang, D. Jang, B.S. Bae, Flexible Hard Coating: Glass-Like Wear Resistant, Yet Plastic-Like Compliant, Transparent Protective Coating for Foldable Displays, Adv Mater 29(19) (2017).

[177] H.A. Sherif, F.A. Almufadi, Identification of contact parameters from elastic-plastic impact of hard sphere and elastic half space, Wear 368-369 (2016) 358-367.

[178] J.F. Archard, Contact and Rubbing of Flat Surfaces, J Appl Phys 24(8) (1953) 981-988.

[179] A. Yazdani, T. Isfahani, Hardness, wear resistance and bonding strength of nano structured functionally graded Ni-Al2O3 composite coatings fabricated by ball milling method, Advanced Powder Technology 29(5) (2018) 1306-1316.

[180] I. Konyashin, B. Ries, D. Hlawatschek, Y. Zhuk, A. Mazilkin, B. Straumal, F. Dorn, D. Park, Wear-resistance and hardness: Are they directly related for nanostructured hard materials?, International Journal of Refractory Metals and Hard Materials 49 (2015) 203-211.

[181] L. Yang, M. Wen, X. Dai, G. Cheng, K. Zhang, Ultrafine Ceramic Grains Embedded in Metallic Glass Matrix: Achieving Superior Wear Resistance via Increase in Both Hardness and Toughness, ACS Applied Materials & Interfaces 10(18) (2018) 16124-16132.

[182] Y. Li, Z. Peng, E. Larios, G. Wang, J. Lin, Z. Yan, F. Ruiz-Zepeda, M. Jose-Yacaman, J.M. Tour, Rebar graphene from functionalized boron nitride nanotubes, ACS Nano 9(1) (2015) 532-8.

[183] Z. Yan, Z. Peng, G. Casillas, J. Lin, C. Xiang, H. Zhou, Y. Yang, G. Ruan, A.R. Raji, E.L. Samuel, R.H. Hauge, M.J. Yacaman, J.M. Tour, Rebar graphene, ACS Nano 8(5) (2014) 5061-8.

[184] J.A. Rincon-Lopez, J.A. Hermann-Munoz, A.L. Giraldo-Betancur, A. De Vizcaya-Ruiz, J.M. Alvarado-Orozco, J. Munoz-Saldana, Synthesis, Characterization and In Vitro Study of Synthetic and Bovine-Derived Hydroxyapatite Ceramics: A Comparison, Materials (Basel) 11(3) (2018).

[185] A. Dorri Moghadam, E. Omrani, P.L. Menezes, P.K. Rohatgi, Mechanical and tribological properties of self-lubricating metal matrix nanocomposites reinforced by carbon nanotubes (CNTs) and graphene – A review, Composites Part B: Engineering 77 (2015) 402-420.

[186] H.B. Zhang, J.W. Wang, Q. Yan, W.G. Zheng, C. Chen, Z.Z. Yu, Vacuum-assisted synthesis of graphene from thermal exfoliation and reduction of graphite oxide, Journal of Materials Chemistry 21(14) (2011) 5392-5397.

[187] S. Ehtemam-Haghighi, K.G. Prashanth, H. Attar, A.K. Chaubey, G.H. Cao, L.C. Zhang, Evaluation of mechanical and wear properties of Ti xNb 7Fe alloys designed for biomedical applications, Mater Design 111 (2016) 592-599.

[188] S. Pei, H.M. Cheng, The reduction of graphene oxide, Carbon 50(9) (2012) 3210-3228.

[189] B.D. Beake, A.J. Harris, T.W. Liskiewicz, Review of recent progress in nanoscratch testing, Tribology - Materials, Surfaces & Interfaces 7(2) (2013) 87-96.

[190] T.-H. Fang, W.-J. Chang, C.-M. Lin, Nanoindentation and nanoscratch characteristics of Si and GaAs, Microelectronic Engineering 77(3-4) (2005) 389-398.

[191] R. Gecu, A. Karaaslan, Relationship Between Nanoindentation and Wear Properties of Stainless Steel-Reinforced Aluminium Matrix Composite, Tribology Letters 65(4) (2017).

[192] Q. Zhou, Y. Du, Y. Ren, W. Kuang, W. Han, H. Wang, P. Huang, F. Wang, J. Wang, Investigation into nanoscratching mechanical performance of metallic glass multilayers with improved nano-tribological properties, Journal of Alloys and Compounds 776 (2019) 447-459.

[193] S.R. Bakshi, D. Lahiri, R.R. Patel, A. Agarwal, Nanoscratch behavior of carbon nanotube reinforced aluminum coatings, Thin Solid Films 518(6) (2010) 1703-1711.

[194] M. Gee, L. Nimishakavi, Model single point abrasion experiments on WC/Co hardmetals, International Journal of Refractory Metals and Hard Materials 29(1) (2011) 1-9.

[195] B. Shi, J.L. Sullivan, B.D. Beake, An investigation into which factors control the nanotribological behaviour of thin sputtered carbon films, Journal of Physics D: Applied Physics 41(4) (2008).

[196] S.R. Bakshi, A.K. Keshri, A. Agarwal, A comparison of mechanical and wear properties of plasma sprayed carbon nanotube reinforced aluminum composites at nano and macro scale, Materials Science and Engineering: A 528(9) (2011) 3375-3384.

[197] L. Huang, Z. Zhang, Y. Zhao, W. Yao, A.K. Mukherjee, J.M. Schoenung, Scratch-induced deformation in fine- and ultrafine-grained bulk alumina, Scripta Mater 63(5) (2010) 528-531.

[198] Q. Yuan, N. Ramisetti, R.D.K. Misra, Nanoscale near-surface deformation in polymer nanocomposites, Acta Mater 56(9) (2008) 2089-2100.

[199] L. Huang, C. Bonifacio, D. Song, K.v. Benthem, A.K. Mukherjee, J.M. Schoenung, Investigation into the microstructure evolution caused by nanoscratch-induced room temperature deformation in M-plane sapphire, Acta Mater 59(13) (2011) 5181-5193.

[200] C. Li, F. Zhang, Y. Wu, X. Zhang, Influence of strain rate effect on material removal and deformation mechanism based on ductile nanoscratch tests of Lu2O3 single crystal, Ceram Int 44(17) (2018) 21486-21498.

[201] C. Li, F. Zhang, Y. Piao, Strain-rate dependence of surface/subsurface deformation mechanisms during nanoscratching tests of GGG single crystal, Ceram Int (2019).

[202] C. Li, F. Zhang, B. Meng, X. Rao, Y. Zhou, Research of material removal and deformation mechanism for single crystal GGG (Gd 3 Ga 5 O 12) based on varied-depth nanoscratch testing, Mater Design 125 (2017) 180-188.

[203] J.A. Greenwood, J.H. Tripp, The elastic contact of rough spheres, Journal of Applied Mechanics 34(1) (1967) 153-159.

[204] M. Yu, Strength and Breaking Mechanism of Multiwalled Carbon Nanotubes Under Tensile Load, Science 287(5453) (2000) 637-640.

[205] M. Bohner, Silicon-substituted calcium phosphates–a critical view, Biomaterials 30(32) (2009) 6403-6406.

[206] N. Horiuchi, K. Madokoro, K. Nozaki, M. Nakamura, K. Katayama, A. Nagai, K. Yamashita, Electrical conductivity of polycrystalline hydroxyapatite and its application to electret formation, Solid State Ionics 315 (2018) 19-25.

[207] O. Kaygili, S.V. Dorozhkin, T. Ates, A.A. Al-Ghamdi, F. Yakuphanoglu, Dielectric properties of Fe doped hydroxyapatite prepared by sol–gel method, Ceram Int 40(7) (2014) 9395-9402.

[208] F.E. Al-Hazmi, Synthesis and electrical properties of Bi doped hydroxyapatite ceramics, Journal of Alloys and Compounds 665 (2016) 119-123.

[209] C. López-Pernía, C. Muñoz-Ferreiro, C. González-Orellana, A. Morales-Rodríguez, Á. Gallardo-López, R. Poyato, Optimizing the homogenization technique for graphene nanoplatelet/yttria tetragonal zirconia composites: Influence on the microstructure and the electrical conductivity, Journal of Alloys and Compounds 767 (2018) 994-1002.

[210] Y. Yu, F. Xia, Q. Huang, J. Fang, L. An, Electrical conductivity of silicon carbonitride-reduced graphene oxide composites, J Am Ceram Soc 100(11) (2017) 5113-5119.

[211] N.W. Solís, P. Peretyagin, R. Torrecillas, A. Fernández, J.L. Menéndez, C. Mallada, L.A. Díaz, J.S. Moya, Electrically conductor black zirconia ceramic by SPS using graphene oxide, Journal of Electroceramics 38(1) (2017) 119-124.

[212] M. Xu, T. Liang, M. Shi, H. Chen, Graphene-like two-dimensional materials, Chem Rev 113(5) (2013) 3766-98.